*eXPRESS Polymer Letters Vol.9, No.4 (2015) 329*
*Available online at www.expresspolymlett.com*
*DOI: 10.3144/expresspolymlett.2015.30*

# Editorial corner – a personal view
## Where micro- and nano-worlds meet: multiscale polymer composites

*A. Pegoretti*[*]

Department of Industrial Engineering, University of Trento, via Sommarive 9, 38123 Trento, Italy

In the last twenty years a large amount of scientific data has been published on the preparation and characterization of polymer nanocomposites. Despite the very intense research efforts, the mechanical properties reported so far for nanocomposites are quite disappointing, particularly when compared to that of structural composites reinforced with high-performance continuous fibers (DOI: 10.1126/science.1151434). Among the main causes invoked to explain the obtained results one could mention i) poor dispersion and alignment of nanofillers, ii) difficulties in achieving an elevated volume fraction of nanofillers and iii) scarce bond and load transfer ability at the nanofiller/matrix interface. Intensive research is currently ongoing to tackle and possibly solve the above mentioned problems. Recently, new strategies emerged for the preparation of structural materials in which both micro- and nano-reinforcements coexist in multiscale composites (DOI: 10.1177/0731684412456612). Nanoscale reinforcements have been included within fiber reinforced composites in several ways, such as i) grafting or electrophoretic deposition (mostly of carbon nanomaterials) onto the fiber surface (DOI: 10.1016/j.compscitech.2014.06.019), ii) localization in sizing/coatings for fiber treatment (DOI: 10.1016/j.compositesa.2012.08.027) iii) homogeneous dispersion in the whole polymer matrix (DOI: 10.1177/0731684414542668). The presence of nano-reinforcements in traditional microcomposites has been proven to play beneficial effects on several properties, including delamination resistance, fiber/matrix shear strength (DOI: 10.1016/j.compscitech.2012.12.016), electrical and thermal conductivities. The possibility to improve the electrical conductivity of typically insulating materials such as glass/epoxy laminates, is opening new possibilities for the monitoring of deformation and damage in composite structures under service. For example, it has been proven that an integrated system of carbon nanotubes and piezoelectric sensors can be used to detect both microcracks and localized damage/delamination in composite structures (DOI: 10.1016/j.carbon.2012.04.008). Therefore, nanomodified matrices can be used for a continuous monitoring of deformational levels and damage of structural composites under various loading conditions such as fatigue, impact and creep (DOI: 10.1016/j.compositesa.2012.03.019). Can we dream of polymer composites in which micro- and nano-structures synergistically operate to provide both structural and functional features, including self-repairing and adaptive responses?

Prof. Dr. Alessandro Pegoretti
Member of International Advisory Board

[*]Corresponding author, e-mail: alessandro.pegoretti@unitn.it

*eXPRESS Polymer Letters Vol.9, No.4 (2015) 330–343*
*Available online at www.expresspolymlett.com*
*DOI: 10.3144/expresspolymlett.2015.31*

# Effect of phosphorous-containing modified poly(vinyl alcohol) on the mechanical and flame retardant properties of polypropylene

*S. Saucă*[1], *M. Giamberini*[2], *P. Cerruti*[3*], *M. Malinconico*[3], *J. A. Reina*[1]

[1]Departament de Química Analítica i Química Orgànica, Facultat de Química, Universitat Rovira i Virgili, Campus Sescelades, Carrer Marcel·lí Domingo s/n, E-43007 Tarragona, Spain
[2]Departament d'Enginyeria Química, Escola Tècnica Superior d'Enginyeria Química, Universitat Rovira i Virgili, Campus Sescelades, Av. Països Catalans 26, E-43007 Tarragona, Spain
[3]Institute of Polymers, Composites and Biomaterials (IPCB-CNR), Via Campi Flegrei 34, 80078 Pozzuoli (Na), Italy

*Received 28 May 2014; accepted in revised form 9 October 2014*

**Abstract.** Blends of polypropylene (PP) and different phosphorous-modified poly(vinyl alcohol) (PVA) derivatives synthesized on purpose, were prepared by both solvent and melt mixing, and fully characterized. Thermogravimetric analysis showed that the addition of the phosphorous-modified PVAs significantly increased thermal stability and charring of PP, probably due to their dehydration and the subsequent formation of a protective layer onto PP. SEM analysis demonstrated poor phase compatibility between PP and the polymeric additives, however acceptable dispersion of the polymeric additives was obtained. It was also observed that grafting of the modified PVA on PP occurred due to radical reactions arising during melt processing. Mechanical characterization showed that the elastic behavior of the blends was not altered with respect to neat PP, while ductility was reduced; on the other hand, impact resistance was considerably improved by blending. Slightly higher LOI values were obtained for the blends even with phosphorous content as small as 1 wt%; reduced dripping was also observed during the burning tests for the blend samples. Moreover, cone calorimeter test results showed that heat release rate, total heat release, and fire growth rate decreased compared with PP, in particular for the blends containing residual –OH groups on the PVA backbone. Therefore, these blends can find application where the combination of toughness and fire retardancy is required, such as in the automotive industry.

***Keywords:*** *polymer blends and alloys, poly(vinyl alcohol), polypropylene, flame retardant polymers, material testing*

## 1. Introduction

Polypropylene (PP) is one of the most widely used polymer because of its low cost, ease of processing as well as high water and chemical resistance. PP is used in several applications, for example housing, electronic pieces, wire and cables, automotive industry. However, it is inherently combustible [1–4], giving rise to problems such as evolution of smoke and toxic gases formed during combustion that are of particular concern among government regulatory bodies, consumers and manufacturers. A solution to reduce PP flammability is to incorporate flame retardants (FR) in the polymer structure [5–7]. As well known in the literature, FR can be introduced in the polymer matrix through a chemical modification of polymer (reactive FR) or by blending (additive FR) [8–11]. Phosphorous-containing flame retardants are widely used since they are more environmentally friendly compared to halogen-based flame retardants. The phosphorous based FR may operate in the vapor phase, suppressing the combustion of the flammable mixture through a radical mechanism which

*Corresponding author, e-mail: cerruti@ictp.cnr.it

interferes with the exothermic reactions. In the condensed phase, these FR can promote the formation of a charred layer on the polymer surface, which acts as a barrier against diffusion of volatile products as well as shielding the polymer surface from heat and air [3, 5, 6, 9].

Polymeric flame retardant additives are particularly interesting: the advantage of using them rather than conventional non-polymeric species is that they show better resistance to extraction, migration and volatilization due to their high molecular weight [12, 13]. In a previous paper, a set of polymers which showed promising action as flame retardant additives, obtained by chemically modifying poly(vinyl alcohol) (PVA) with 4-chloroformyl-1-oxo-2,6,7-trioxa-1-phosphabicyclo[2.2.2]octane (BIC), was synthesized and characterized [14]. The choice of PVA as a starting preformed polymer was due to its high availability, low cost, and relatively high reactivity. Moreover, PVA is potentially able to form char due to the presence of free hydroxyl groups. On heating, they can undergo dehydration reactions giving rise to unsaturated materials, especially in presence of phosphorous-containing moieties which can act as a dehydration catalyst source [15].The chemical structures of the prepared polymers are depicted in Figure 1. The choice of these structures was motivated by their expected different polarities, which could in turn confer different compatibility properties on blending with commodity polymers. PVA main chain and BIC moieties are quite polar. On the other hand, grafting of less polar aliphatic and aromatic ester groups onto PVA backbone lead to polymers showing a wider range of polarity.

In this work we chose PP as a thermoplastic material to be flame-retarded on blending with the above mentioned PVA derivatives. To this aim, we prepared blends by mixing the polymeric additives with PP in a suitable solvent and studied their flame retardancy behavior by thermogravimetry (TG) and limiting oxygen index (LOI) techniques. After assessing the efficiency of the PVA derivatives as flame retardant melt mixed blends were also prepared. Molecular weight, compatibility and mechanical properties of the melt mixed blends were determined through gel permeation chromatography (GPC), differential scanning calorimetry (DSC), X-Ray diffraction (XRD), dynamic mechanical thermal analysis (DMTA), scanning electron microscopy (SEM), impact and tensile tests. Finally, their flame retardancy properties were also assessed.

## 2. Experimental section

### 2.1. Materials

Moplen type polypropylene EP1X30F (MPP, containing 2 wt% ethylene, $M_w$ = 250 000 Da, melt flow at 230°C = 7.00–10.0 g/10 min) was provided by Montell (Italy). High molecular weight isotactic

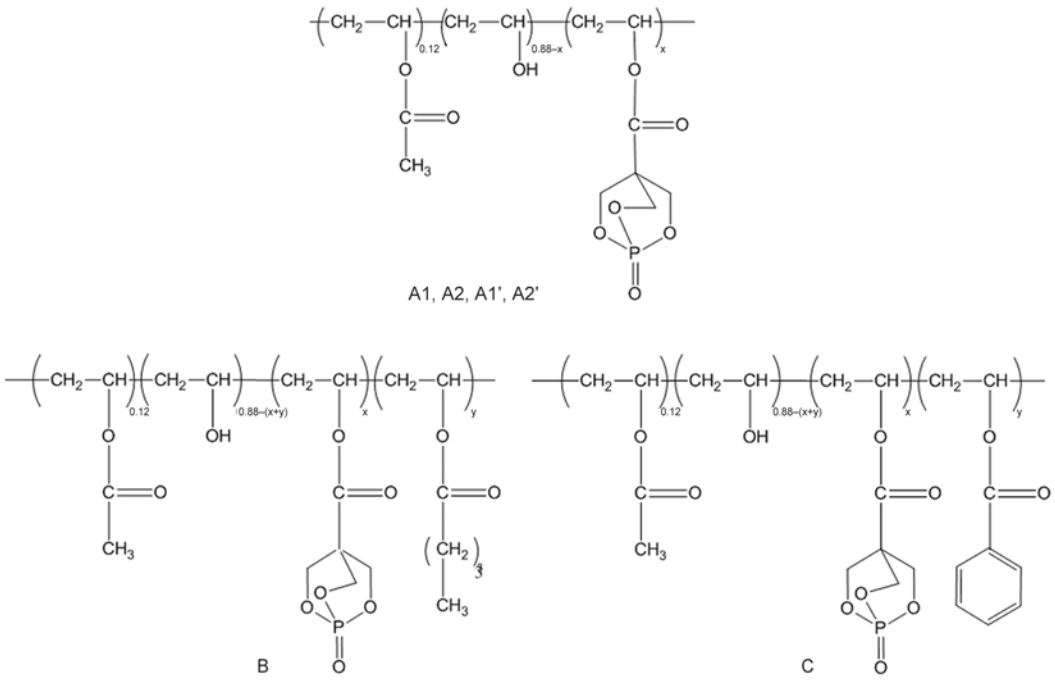


**Figure 1.** Chemical structure of the synthesized polymers

**Table 1.** Degrees of modification and phosphorous content of the additives

| Additive | P obtained from ICP-AES [wt%] | Degree of modification | | |
|---|---|---|---|---|
| | | $x^a$ | $x^b$ | $y^b$ |
| A1 | 11.5 | 0.52 | | |
| A2 | 8.0 | 0.23 | | |
| A1′ | 11.0 | 0.47 | | |
| A2′ | 9.3 | 0.32 | | |
| B | 8.6 | | 0.44 | 0.27 |
| C | 8.7 | | 0.51 | 0.10 |

[a]Obtained from % P determined through ICP-AES
[b]Obtained from $^{13}C$ NMR

polypropylene (HIPP, $M_w$ = 580 000 Da; $T_{m\ onset}$ = 160–165°C) and all solvents were purchased from Sigma-Aldrich (Italy), and used as received. Polymeric flame retardant additives A1 and A2, used for the preparation of the solvent-assisted blends, were synthesized as previously described [14]. The additives A1′, A2′, B and C, used for the melt mixed blends, were prepared through the same procedure, but using a higher amount of reagents (5 g of PVA). The degrees of modification and phosphorous content of the additives, determined through inductively coupled plasma-atomic emission spectroscopy (ICP-AES) and $^{13}C$ NMR, are listed in Table 1.

## 2.2. Blends preparation

### 2.2.1. Blends prepared by dissolution

4.5 g of HIPP and 1,1,2,2-tetrachloroethane (100 mL) were introduced in a round bottomed flask provided with magnetic stirrer. The mixture was heated under stirring up to 100°C to completely solubilise PP, then it was cooled down at 80°C, and the appropriate amount of selected additive was added. The mixture was further driven to reflux and stirred for two hours. Subsequently, the solvent was removed by rotary evaporation and the resulting material was dried under vacuum at 70°C for 1 h, then at room temperature for 24 h. In all cases, proper amounts of HIPP and polymeric additive were selected to prepare 5 g of blend. About 1 g of blend was pressed in a preheated press at 165°C and 2.5 atm for 1 hour in order to get bars (70×6×3 $mm^3$). These processing conditions were chosen in order to avoid thermal degradation of the additives. Table 2 lists the blends prepared in this way. These samples were characterized by means of TG and LOI measurements.

**Table 2.** Blends prepared by solvent dissolution

| Blend | Additive | Additive content [wt%] | Phosphorous content [wt%] |
|---|---|---|---|
| Bl1 | A1 | 8.6 | 1.0 |
| Bl2 | A1 | 4.3 | 0.5 |
| Bl3 | A2 | 6.2 | 0.5 |

### 2.2.2. Blends prepared by melt mixing

Melt mixing was carried out in a Brabender Plastograph EC (Germany) twin screw mixer at 175°C with a screw rate of 40 rpm. Proper amounts of polypropylene (MPP) and polymeric additive were selected to prepare 50 g of blend. The flame retardant additives were added after the MPP melted, and the resulting blend was further mixed for 5 minutes. Then the material was removed, left to cool and cut in pellets. The pellets were hot-pressed using a Collin P200E bench top press, under a pressure of 100 bar at 165°C for 3 minutes, to obtain thin films (average thickness 150 μm), or at 175°C for 5 minutes, to obtain plates of 3 mm thickness. Thin films samples were used to perform Fourier transform infrared (FTIR) spectroscopy, TG, DSC, XRD and tensile tests, while the plates were cut in bars and used for DMTA, Charpy impact tests, cone calorimeter tests and LOI measurements. The blends prepared in this way are listed in Table 3.

## 2.3. Characterization techniques

Transmission FTIR analysis was performed using a Nicolet Nexus FTIR spectrophotometer (USA). Spectra were collected using 32 scans at 4 $cm^{-1}$ resolution, in the 400–4000 $cm^{-1}$ range.

The number-average ($M_n$), weight-average ($M_w$) molecular weights and intrinsic viscosities were estimated by GPC using a Waters Alliance GPC V2000 system (USA), equipped with refractive index and viscosimetric detectors, using two consecutive Polymer Laboratories (UK) mixed columns with 1,2-dichlorobenzene (DCB) at 145°C as eluent (0.8 $mL \cdot min^{-1}$). The equipment was calibrated with polystyrene standards.

LOI measurements were performed in triplicate in vertical tests on a Stanton Redcroft FTA (UK) flammability unit provided with an oxygen analyzer, previously calibrated with polystyrene standard

**Table 3.** Blends prepared by melt mixing

| Blend | Additive | Additive content [wt%] | Phosphorous content [wt%] |
|---|---|---|---|
| Bl4 | A1′ | 9.0 | 1 |
| Bl5 | A2′ | 10.8 | 1 |
| Bl6 | B | 11.6 | 1 |
| Bl7 | C | 11.6 | 1 |

bars. The dimensions of the polymer bars prepared by hot pressing were 70×6×3 mm$^3$.

Cone calorimeter (CC) tests were performed in duplicate by a Fire Testing Technology (UK) cone calorimeter. The samples with the dimension of 60×60×3 mm$^3$ were exposed to a radiant cone at a heat flux of 35 kW·m$^{-2}$.

TG analysis of blends prepared by dissolution was carried out on a Mettler TGA/SDTA851e/LF/1100 (Switzerland) device at a heating rate of 10°C·min$^{-1}$ up to 800°C under nitrogen atmosphere (flow rate = 100 mL·min$^{-1}$). For the blends prepared by melt mixing, TG analysis was performed on a Perkin Elmer Pyris Diamond TG-DTA thermogravimetic analyzer (USA) under the same conditions, but in this case prior to the heating ramp the samples were subjected to a 30 minutes isotherm at 80°C to remove the moisture that could be absorbed after the melt processing.

DSC analyses were performed on a Mettler Toledo DSC Star 822e (Switzerland) calorimeter at a heating/cooling rate of 10 C·min$^{-1}$ in a nitrogen atmosphere. Melting temperatures and enthalpies were calculated from second heating scans. The crystallinity degree of MPP and its blends was calculated by using $\Delta H°_{melting}$ = 209 J g$^{-1}$, reported as the melting enthalpy of 100% crystalline PP [16].

XRD experiments were performed using a Philips PW 1710 (Netherlands) diffractometer with a rotating anode generator and a wide-angle power goniometer. The used radiation was unfiltered Cu Kα, with 40 kV voltage and 20 mA intensity. The scan rate was 1°·min$^{-1}$ over a diffraction angle 2θ ranging between 2 and 40°. The evaluation of the degree of crystallinity for each sample was obtained from the ratio between the area under the crystalline peaks and the total area under the diffraction curve. The separation of the crystalline peaks from the amorphous part was achieved by curve fitting using Gaussian functions by means of Origin 8.0 software.

A Perkin Elmer Pyris Diamond DMTA (USA) in the dual cantilever flexural mode was used to study the dynamic mechanical thermal behavior of the blends. Rectangular specimens 50 mm long, 10 mm wide, 3 mm thick were analyzed. The samples were conditioned in an environmental chamber at 25°C and 50% relative humidity (RH) for 7 days prior to testing. The tests were run at a heating rate of 3°C·min$^{-1}$ from –80 to 140°C under nitrogen. Oscillation frequency and amplitude were 1 Hz and 5 μm, respectively. $T_g$ was taken as the peak value of tan δ curves.

Charpy impact tests were performed on a CEAST 6545 (Italy) apparatus according to ASTM standard test method D256-06. A standard notch (3.5 mm long) was applied to the rectangular shaped rod sample with dimensions of 60×60×3 mm$^3$. The notch was in the opposite direction to the striking hammer.

A Philips XL20 (Netherlands) Scanning electron microscope (SEM) was used to examine the morphology of the cross-section of specimens subjected to impact tests. Samples were metallised before the observation with a gold–platinum mixture by means of a BalTec MED020 (UK) coater.

Tensile tests were performed on an Instron 5564 (USA) dynamometer equipped with a 100 N load cell on test specimens prepared according to ASTM D882-02 standard test method. The test samples were 'dog-bone' shaped 22 mm long, 4 mm wide. The thickness (0.1–0.2 mm) was measured at different points for each specimen and its average value was introduced in the Instron Merlin calculation software. The tests were performed using 5–8 specimens for each sample. The measurements were carried out at an elongation rate of 20 mm·min$^{-1}$ at room temperature after the samples were conditioned for 24 hours at 50% RH.

## 3. Results and discussion

### 3.1. Characterization of the blends obtained by dissolution

As a preliminary study, we prepared blends of PP with flame retardant additives by solvent dissolution, using a polypropylene grade with high molecular weight and melting point (HIPP). The HIPP blends were prepared by dissolution in hot 1,1,2,2-tetrachloroethane (Table 2). Additive contents lower than 10 wt% were used, since higher amounts would have affected negatively the mechanical properties of PP. Therefore blends containing 1 or 0.5 wt% of phosphorous were prepared, to evaluate the effect of the additive amount on the flame retardancy of polypropylene.

The obtained blends were studied by TG and LOI techniques. The thermogravimetric curves under nitrogen are shown in Figure 2, and the relative data are listed in Table 4. From the figure, a slight weight loss was observed for the blends at about 250°C, associated to polymeric additives decomposition (mainly dehydration of the vinyl alcohol moieties). Moreover, in the blends the main weight loss process was significantly delayed (>100°C), and a residual

**Table 4.** Thermogravimetric and LOI results of neat HIPP and its blends

| Sample | Additive | Phosphorous content [wt%] | $T_{onset}$[a] [°C] | $T_{max}$[b] [°C] | Char yield at 600°C [%)] | LOI [%] |
|---|---|---|---|---|---|---|
| HIPP | | | 297 | 415 | | 17.3±0.3 |
| Bl1 | A1 | 1.0 | 408 | 463 | 6.0 | 18.7±0.4 |
| Bl2 | A1 | 0.5 | 416 | 463 | 2.5 | 17.7±0.2 |
| Bl3 | A2 | 0.5 | 421 | 463 | 2.9 | 18.2±0.4 |

[a]Onset temperature of the main weight loss process
[b]Temperature of the maximum rate of weight loss

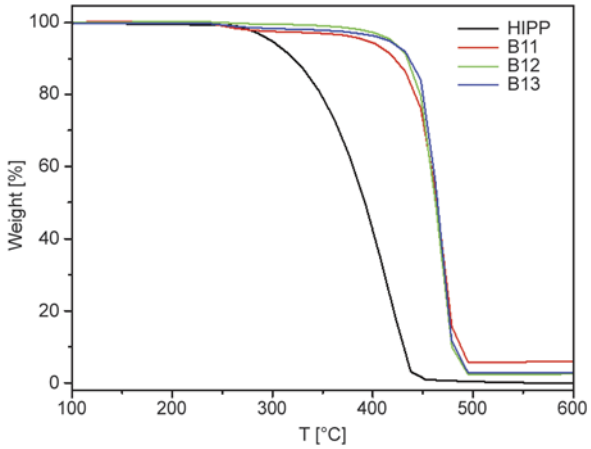


**Figure 2.** TG curves of neat HIPP and its blends in nitrogen atmosphere

char was formed at high temperature, while pure HIPP completely volatilized below 500°C. These results suggest that the additives can confer flame retardancy to PP. In this respect, A2 was likely more effective than A1, since Bl3 showed higher $T_{onset}$ and char yield with respect to Bl2. This slightly higher effectiveness shown by A2 can be related with its larger hydroxyl content (see Table 1), if we reasonably assume that dehydration is the first step of the additives decomposition.

The results of LOI measurements are reported in Table 4. The LOI values of the blends were slightly higher than that of neat HIPP. Therefore, LOI data also confirmed that flame retardancy was conferred by A1 and A2 to HIPP. In particular, the highest LOI value was obtained for the blend containing the highest phosphorous amount (B11), while at low phosphorous content the LOI value was higher when the blend contained more hydroxyl groups (B13). This result was in agreement with TG data.

### 3.2. Chemical characterization of melt mixed blends

Once the effectiveness of the additives as flame retardants was assessed, the modified PVAs were blended to PP through melt mixing, which is a more technologically feasible processing technique compared to solvent blending. For melt mixing, we selected a Moplen type polypropylene containing 2 wt% ethylene (MPP) as matrix. MPP had higher flexibility than HIPP, and Moplen type PPs have been used for different applications in automotive industry [17–20] MPP was blended with A1′, A2′, B and C at 175°C and 40 rpm for 5 min. For each blend, the amount of the polymeric additive was selected in order to get a phosphorous content of 1 wt%. In Table 3 the blends formulations are listed.

In order to probe the possibility that MPP or the polymeric additives partially degraded during the blending process, the obtained blends were characterized by FTIR and GPC. In general, FTIR spectra of the blends showed peaks due to MPP and the corresponding additive. The main MPP bands appeared at 3000–2850 $cm^{-1}$ (C–H stretching) and 1500–1350 $cm^{-1}$ (C–C stretching). All the blends showed signals due to the additives at 3600–3400 $cm^{-1}$ (O–H), 1730 $cm^{-1}$ (C=O) and 856 $cm^{-1}$ (skeleton vibration of caged bicyclic phosphate). It should be noted that no additional bands appeared in the blends with respect to virgin MPP and additives. This suggests that degradation upon blending, if any, occurred to a low extent. As an example, Figure 3 shows the spectrum of virgin MPP, the polymeric additive B and the corresponding blend (B16).

GPC analysis was performed in DCB at 145°C. The obtained data are collected in Table 5. For the sake of comparison, GPC analysis was also performed on unprocessed MPP and on a MPP sample processed analogously to the blends.

The polydispersity ($M_w/M_n$) of the unprocessed MPP is rather high, typical of a PP synthesized in the presence of Ziegler-Natta catalysts [21]. As can be seen, molecular weights and polydispersity of processed MPP were lower than those of unprocessed polymer pellets. Thus, melt-mixing processing of neat MPP brought about slight degradation of the polymer. The decrease of polydispersity is consistent with 'con-

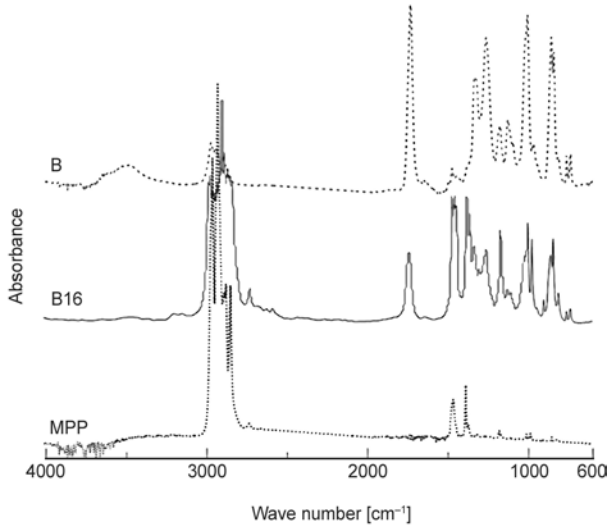


**Figure 3.** FTIR spectrum of virgin MPP, the additive B, and the corresponding blend B16

trolled PP degradation' principles, where the highest molecular weight chains are statistically more likely to undergo radical-mediated scission [22].

Although the polymeric additives were rather insoluble in DCB, when they were incorporated into the blends a significant fraction turned to be dissolved in the solution subjected to GPC characterization. Nevertheless, as can be observed from Figure 4a and Table 5, the GPC curves of the blends were similar to that of neat processed MPP, leading to comparable $M_w$ and polydispersity, and neither peaks related to the presence of the additive, nor bimodal patterns of the molecular-mass curves were observed. The blend B17 is an exception to this general behaviour, since its GPC chromatogram showed a minor portion of higher molecular weight chains.

These findings suggest that the polymeric additives could interact with the polypropylene phase, forming physical or chemical associates having a slightly larger hydrodynamic volume than that of plain MPP, which were not separated during the elution run. This could also explain the increase in $M_w$ observed for B17, in which the bulky pendant substituent can modify the size of the dissolved polymer adduct, thus yielding increased values of molecular weight [23].

A further confirmation of this hypothesis can be obtained by the Mark-Houwink-Sakurada (MHS) plots, Figure 4b, in which the intrinsic viscosity is plotted as a function of $M_w$. MHS plots are widely used for the analysis of polymer structure, as they reflect structural changes in the polymer, such as branching and chain rigidity [24]. The slope described by the Mark-Houwink exponent can vary between 0 for solid spheres and 2 for rod-shaped structures.

From the figure, it is observed that while all samples showed comparable curve slope values of about 0.71 (typical of linear flexible chains in good solvents), the processed MPP sample displayed higher values of viscosity throughout the range of

**Table 5.** GPC data of neat MPP and its blends

| Sample | Additive | $M_w$[a] [Da] | $M_w/M_n$[b] | $M_{peak}$[c] [Da] |
|---|---|---|---|---|
| Unprocessed MPP | – | 254 000 | 6.8 | 159 000 |
| Processed MPP | – | 218 000 | 4.5 | 136 000 |
| B14 | A1′ | 218 000 | 4.8 | 139 000 |
| B15 | A2′ | 229 000 | 5.2 | 144 000 |
| B16 | B | 235 000 | 4.8 | 145 000 |
| B17 | C | 278 000 | 4.6 | 159 000 |

[a]weight-average molecular weight
[b]polymer polydispersity
[c]peak of the GPC curve

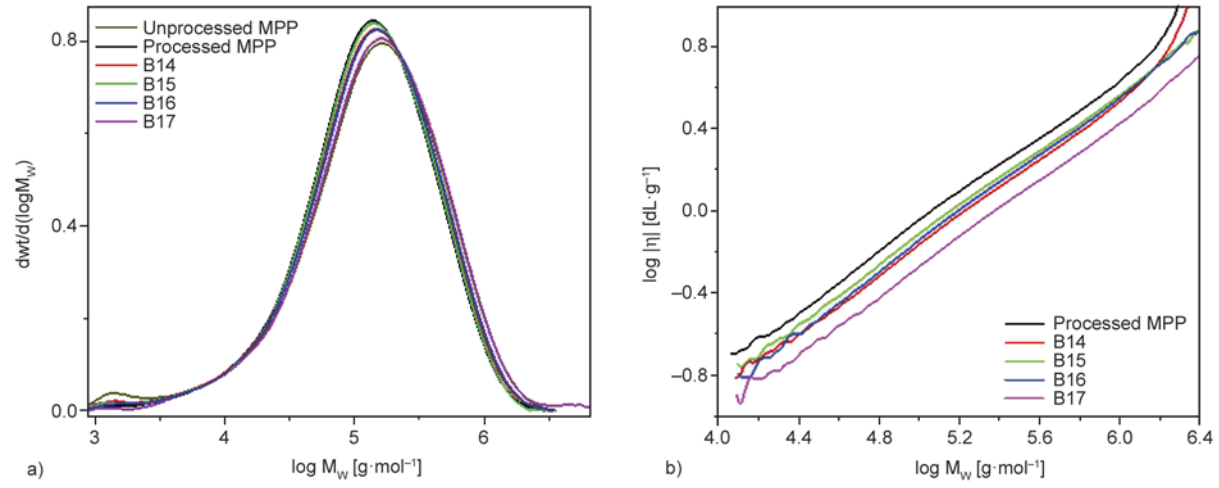


**Figure 4.** GPC chromatograms (a) and Mark-Houwink-Sakurada plots (b) of neat MPP and its blends

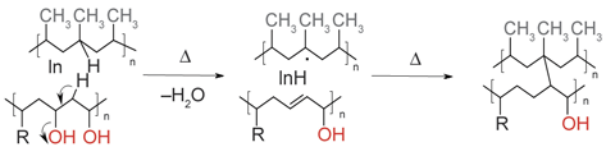


**Figure 5.** Scheme of the possible reactions involved in PVA grafting onto PP

$M_w$ values analyzed. This suggests that polypropylene molecules in the blends present chain branching [25], due to the interaction of MPP with the modified PVAs. This can be due to some radical reactions that may occur between additives and matrix, as depicted in Figure 5. Usually, radical formation occurs in the presence of an initiator, identified as [In] in the figure [26, 27], which in this case may be represented by the metal particles of the equipments used for processing. Also, we should take into account that a small part of the PVAs additives may undergo dehydration reactions, leading to double bond formation, which can react with the polypropylene free radicals that could be formed during processing at high temperature.

### 3.3. Crystallinity of the melt mixed blends

In order to study the effect of the additives on the polypropylene crystallinity, DSC and XRD experiments were performed. The DSC thermograms of the processed MPP showed a melting endotherm spanning between 143 and 161°C. The DSC data of the blends revealed that the melting temperature of polypropylene was not apparently affected by the addition of the flame retardant additives (see Table 6), indicating the absence of interactions such as co-crystallization within the polypropylene phase [28], as well as poor compatibility of the flame retardants with polypropylene. Since the glass transition signal from DSC traces was rather weak and broad, the $T_g$s of the blends were determined through DMTA (see Section 3.4).

Melting enthalpy values were used to calculate the crystallinity of MPP and blends. As can be seen from Table 6, the degree of crystallinity of MPP remained unaltered after blending with the flame retardant additives, with the exception of the blend B16, for which a slight increase in crystallinity was observed.

From the X-ray diffractograms (Figure 6) can be observed that the monoclinic α form of PP was present in all samples, and no peaks associated with the hexagonal β form (usually detected at 2θ = 16.1°) were visible [29]. This is in agreement with the observation that isotactic polypropylene prepared with the traditional heterogeneous Ziegler-Natta catalysts generally exist in the stable α form [30].

The degree of crystallinity for each sample was obtained also by XRD as detailed in the experimental part. In this approach, the amorphous contribution to the scattering was taken into account through a broad diffraction band. From Table 6, which shows the degrees of crystallinity obtained by XRD and DSC, it can be observed that the results obtained by the two techniques are comparable. Moreover, the blends did not present significant changes in comparison with virgin MPP, with the exception of B16, which contain the polymer B as an additive. The latter has a different chemical structure compared to

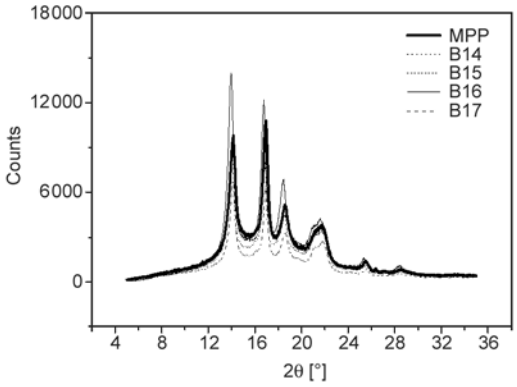


**Figure 6.** X-ray diffractograms of virgin MPP and its blends

**Table 6.** Melting temperatures and enthalpies, $T_g$ and crystallinity degrees of MPP and its blends

| Sample | $T_{peak}$ [°C] | $\Delta H_1$[a] [J·g$^{-1}$] | $\Delta H_2$[b] [J·g$^{-1}$] | $T_g$[c] [°C] | Crystallinity from DSC[d] [%] | Crystallinity from XRD [%] |
|---|---|---|---|---|---|---|
| MPP | 154 | 83 | 83 | –2.3 | 40 | 37 |
| Bl4 | 153 | 73 | 80 | –2.8 | 38 | 43 |
| Bl5 | 154 | 70 | 78 | –2.7 | 37 | 37 |
| Bl6 | 154 | 81 | 89 | 0.1 | 43 | 46 |
| Bl7 | 155 | 73 | 80 | –5.6 | 39 | 41 |

[a]Melting enthalpy per gram of blend
[b]Melting enthalpy per gram of MPP
[c]Glass transition temperature obtained from DMTA
[d]Crystallinity degree obtained from $\Delta H_2$

the other phosphorous containing additives. In fact, the presence of aliphatic butyl chains is able to increase the compatibility of the additive with the matrix, as also showed by SEM analysis (see Section 3.4). This entails that the additive particles can increase PP crystallinity acting as heterogeneous nucleating agents.

### 3.4. Dynamic mechanical thermal, morphological and mechanical properties

In order to get reliable $T_g$ values for the MPP blends, DMTA measurements were carried out. The dynamic viscoelastic curves for the neat MPP and the blends with the modified PVAs are shown in Figure 7. All the storage modulus versus temperature curves experienced a gradual decline with temperature increasing from –80 to 130°C [31]. MPP exhibited two distinct relaxations peaks. The α-relaxation, at about 81°C, relates to slip mechanism of polymer chains in the crystallites [32]. The β-relaxation (–2.3°C) is assigned to the motion of the main chain in the amorphous regions, thus can be regarded as the glass transition temperature [33].

The tan δ curves of the blends showed slight $T_g$ value changes with respect to the parent polypropylene (Table 6). In particular, a small increase was ascribed to B16, while B17 displayed a slightly anticipated glass transition (peak at –5.6°C). The latter result suggests that in the B17 blend the segmental mobility in the amorphous phase was increased, due to the presence of polymer chains bearing bulky aromatic pendants, as already evidenced by the GPC analysis. On the other hand, the increase in $T_g$ observed for B16 can be related to the increase in crystallinity of this sample, as detected through DSC and XRD analysis (see Section 3.3). It is expected that crystallization can impose constraints on chain mobility, thus yielding increased values of glass transition temperature [34].

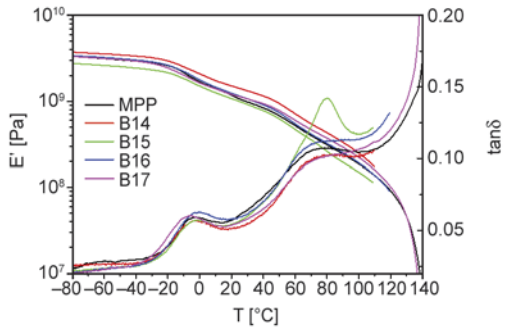


**Figure 7.** Elastic modulus ($E'$) and loss factor (tan δ) versus temperature for neat MPP and its blends obtained by melt mixing

It is also worth noticing that in the case of B15, i.e. the blend containing the additive with the lowest degree of modification (see Table 1), a sharp peak in the mechanical loss spectrum was observed at about 80°C, accounting for the $T_g$ of the unmodified PVA chain segments.

The morphology of neat MPP and its blends was evaluated by SEM observation of the fracture surfaces of samples subject to impact tests. The results are presented in Figure 8.

As can be observed, pure MPP presents a smooth and homogenous surface, evidencing a brittle fracture of the sample. Figure8 b and 8d are similar to virgin MPP, however small, well dispersed additives particles covered by a layer of polypropylene matrix could be observed. In Figure 8c and 8e large additive particles are poorly dispersed within the MPP matrix, thus indicating a strong incompatibility between the polymers. In particular, several voids ascribed to removal of the additive due to the mechanical stress are present on the surface of B15. Therefore, it should be concluded that although all the blends are incompatible, the dispersion of polymeric additives is acceptable in B14 and B16, while severe incompatibility is observed for B15 and B17. It should be noted that, regarding the flame retardancy of a material in general, the low phase compatibility is not a drawback, yet it can negatively affect the mechanical properties of the final blend. However, from SEM analysis it is also evident that samples B15 and B17 show a more ductile fracture, as confirmed by the appearance of multiple fracture planes.

The mechanical properties of the blends prepared by melt mixing were characterized in order to evaluate the effect of the flame retardant additives, with a special view on the poor compatibility observed by SEM analysis. To this aim, tensile and impact tests were carried out on films and rod-shaped samples, respectively. Table 7 displays tensile modulus, yield stress, ultimate stress and elongation at break for all samples. It was observed that pure MPP was able to bear deformations up to 625%, showing typical behaviour of ductile polymers: stress whitening followed by necking and drawing. On the other hand, a brittle behaviour was observed for the blends, and the tensile specimens failed just after the linear elastic region of the stress–strain curves. Since GPC

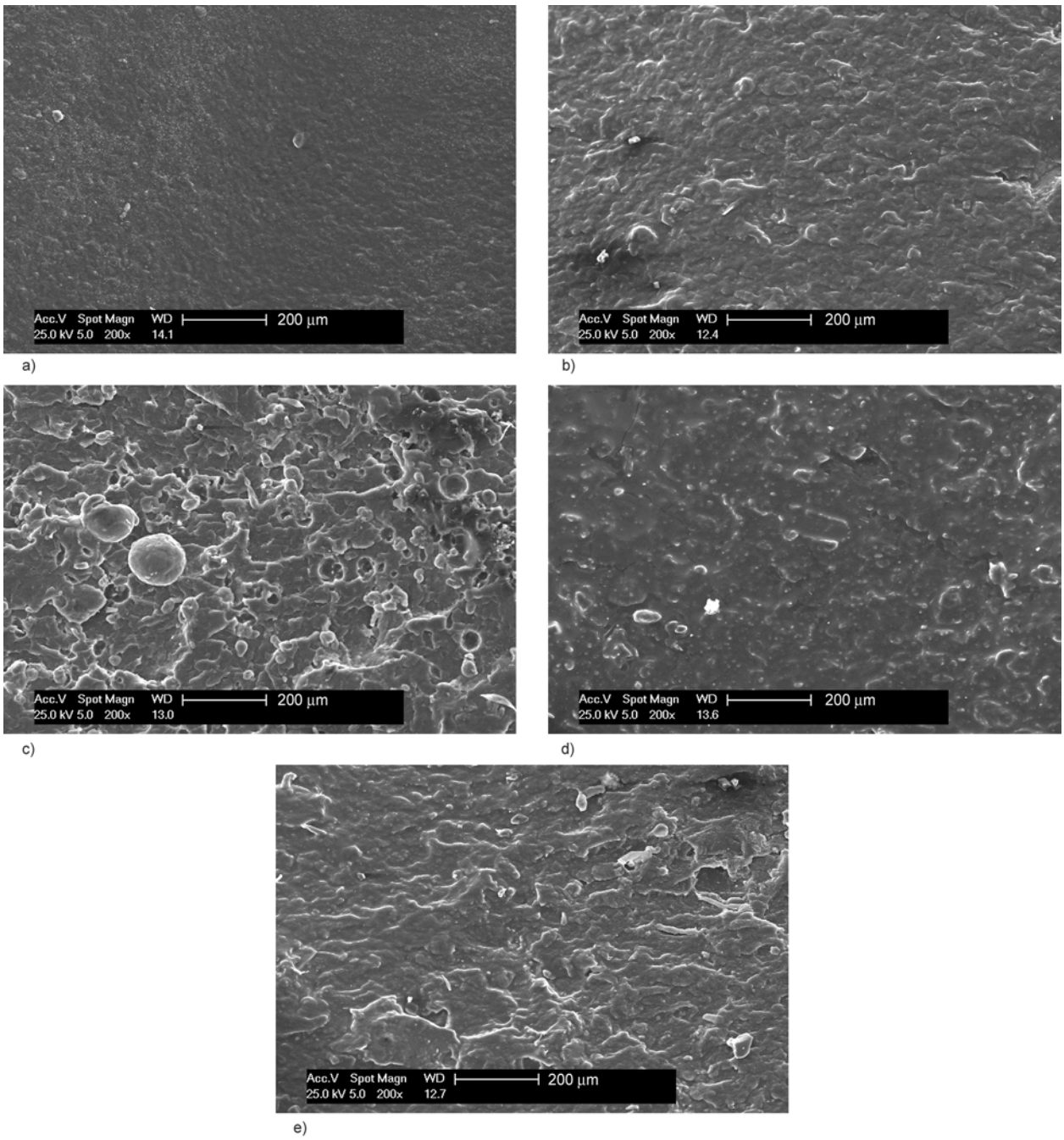


**Figure 8.** SEM micrographs of the fracture surface of plain MPP (a) and its blends: B14 (b), B15 (c), B16 (d), and B17 (e)

**Table 7.** Mechanical tests results for MPP and its blends

| Sample | Elastic modulus [MPa] | Yield stress [MPa] | Ultimate stress [MPa] | Elongation at break [%] | Resilience [kJ·m$^{-2}$] |
|---|---|---|---|---|---|
| MPP | 970±0.2 | 25±1.9 | 32±5.8 | 625±166.7 | 1.8±0.2 |
| Bl4 | 1063±0.3 | 26±1.0 | 21±1.1 | 12±2.5 | 2.1±0.1 |
| Bl5 | 1135±0.2 | 21±1.3 | 19±1.2 | 5±0.8 | 2.7±0.2 |
| Bl6 | 1027±0.2 | 22±0.9 | 19±0.5 | 16±3.9 | 2.3±0.2 |
| Bl7 | 1032±0.2 | 17±2.9 | 16±2.4 | 4±1.2 | 2.4±0.3 |

results showed that polypropylene molecular weight was not affected by the presence of the additives, this behaviour can be due to the poor interfacial interaction between matrix and flame retardant additives. As shown by SEM observations, the flame retardant additives were not well blended, but only dispersed in the matrix. In such a case, strength and elongation at break for filled systems depend on the

state of the polymer-particle interface, since when the adhesion between filler and matrix is poor, a reduced stress transfer occurs at the interface, facilitating void opening and crack propagation [35, 36]. Regarding elastic modulus and yield stress, the values obtained for the blends did not vary significantly with respect to that of the starting MPP. In particular, all the blends showed a slight increase in modulus, suggesting that the additive particles can act as weakly reinforcing fillers, whereas yield stress decreased to some extent. On the other hand, the ultimate stress and the elongation at break noticeably decreased compared to the starting MPP. It can be mentioned that the blends B14 and B16 showed slightly better elongation at break with respect to the other blends, which is probably due to better compatibility between the corresponding additive and the matrix, as observed by SEM micrograph analysis. Therefore, tensile tests showed that the elastic behaviour was not altered by the addition of the flame retardants, whereas the plastic behaviour was changed significantly. It must be noted that in several applications where PP must be flame retarded, elastic and impact properties of the material are crucial, while the plastic behaviour is not [37, 38]. Actually PP-based blends are widely used in many cases where good resistance to physical impulsive shocks is needed. For example, in automotive industry PP-based blends are constituents of many items, such as bumpers, in which the impact resistance is very important. Thus, it is convenient to evaluate impact properties of the materials where high toughness is required. The toughness of the starting MPP and its blends is displayed in Table 7 in terms of impact resilience. All blends showed higher toughness compared to MPP and B15 and B17 showed the highest resilience values. This can be related to SEM observations, which showed a more ductile fracture even though poor compatibility was observed for these blends. As already mentioned for the tensile tests, these results can be explained by considering that the size of the stiff particles dispersed into the matrix is in the range of tenths of microns, which make the additive particles acting as fillers. This can confer greater toughness to the matrix even with poor filler-to-matrix interaction. In fact, the impact energy can be partially dissipated in a mechanism, where the crack advancement is hindered by the presence of the stiffer additive particles. Crack deflection and twisting occur as a growing crack encounters the matrix-particle interfaces, which act primarily ahead of the crack tip to impede crack advance [39].

In summary, impact tests showed that the prepared blends can find application where toughness properties are required, while they increase slightly MPP flame retardancy, as it will be seen later.

### 3.5. Thermal and flammability properties of the melt mixed blends

Thermal stability and flame retardancy behaviour of the prepared melt mixed blends was characterized by TG analysis, LOI and cone calorimeter measurements.

Figure 9 shows the thermogravimetric curves of melt processed MPP and its blends in nitrogen atmosphere. From the curves it can be observed that neat MPP showed one weight loss step between 400 and 500°C, while all blends displayed an additional degradation step in the 200–300°C temperature range. This additional weight loss process has been attributed to the decomposition of the additives initiated by thermal dehydration reactions, as confirmed by massive water evolution detected through mass spectrometry [11].

This step appeared at a slightly lower temperature in B15 with respect to the other blends, probably due to its higher content of –OH groups. Table 8 shows the onset temperature of weight loss, the temperature of the maximum rate of weight loss for both steps, and the char yield at 600°C.

As can be seen in Figure 9 and Table 8, the second weight loss step of the blends, which is related to MPP degradation, was slightly delayed with respect to virgin MPP. Therefore, as it was observed for the blends obtained by dissolution, it is likely that the dehydration of additives led to a charred layer which

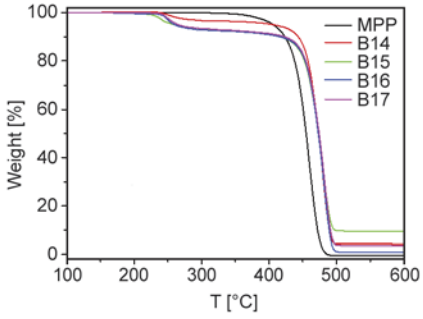


**Figure 9.** TG curves of MPP and its blends

**Table 8.** Thermogravimetric and LOI results of neat MPP and its blends

| Sample | Additive | Step 1 | | Step 2 | | Char yield at 600°C [%] | LOI [%] |
|---|---|---|---|---|---|---|---|
| | | $T_{onset}$ [°C] | $T_{max}$ [°C] | $T_{onset}$ [°C] | $T_{max}$ [°C] | | |
| MPP | | | | 403 | 460 | – | 17.2±0.3 |
| Bl4 | A1′ | 237 | 246 | 432 | 480 | 4.2 | 19.4±0.2 |
| Bl5 | A2′ | 225 | 240 | 429 | 481 | 9.3 | 19.2±0.4 |
| Bl6 | B | 236 | 249 | 431 | 481 | 0.9 | 19.0±0.4 |
| Bl7 | C | 233 | 249 | 432 | 483 | 3.5 | 18.8±0.5 |

can protect polypropylene from degradation. From this point of view, no differences can be observed between the different additives used.

At the end of the second degradation step, neat MPP completely volatilized at 500°C, whereas the blends yielded a residue at 600°C. The highest amount of residue was associated to B15, as higher content of –OH groups favoured charring. B16 showed a lower char yield, probably due to the aliphatic nature of the side groups introduced. Therefore, as already discussed for the blends prepared by dissolution, the polymeric additives can confer flame retardancy also to the melt mixed blends.

As can be seen in Table 8, even with a small content of phosphorous (1 wt%), LOI values increased to some extent in comparison with the plain polypropylene. Reduced dripping was also observed during the burning tests for the additivated samples. Thus, LOI values confirmed that the additives A1′, A2′, B and C are able to increase MPP flame retardancy in the melt mixed blends.

Cone calorimeter (CC) test is an effective method to study the flammability of materials. To further investigate the effect of the phosphorous modified PVAs on the flame behavior of PP, CC tests were performed using a heat flux of 35 kW·m$^{-2}$. The heat release rate (HRR) and the mass loss curves of MPP and the blends are shown in Figure 10, while the relevant data obtained from CC measurements are listed in Table 9.

It was observed that the peak of heat release rate (PHRR) for neat PP was 1109.1 kW·m$^{-2}$, and its total heat release (THR) was 100.7 MJ·m$^{-2}$. All the blends showed reduced values of both HRR and THR compared to MPP. In particular, B15 displayed a PHHR value about 25% lower than MPP, while a 24% decrease of the THR was measured for B14. These results suggest that the presence of phosphorous atoms associated with higher amounts of –OH groups increased the flame retardant properties of the blends. Based on the HRR curves, the fire growth rate (FGR) was calculated as the PHHR to $PHRR_t$ ratio [40, 41], to assess the fire hazard of the samples. In general, lower FGR values indicate that the time to flashover is delayed, then more time is allowed for people to escape fire. Slightly lower values of FGR were associated to the presence of the modified PVAs, and B15 showed a value of 5.29 kW·m$^{-2}$ s$^{-1}$, which represented a decrease of about 25% with respect to MPP. These results further demonstrated that blending polypropylene of PP with the phosphorous-modified PVA derivatives reduced the FGR of the blends provided that a significant number of free –OH groups is present. On the other hand,

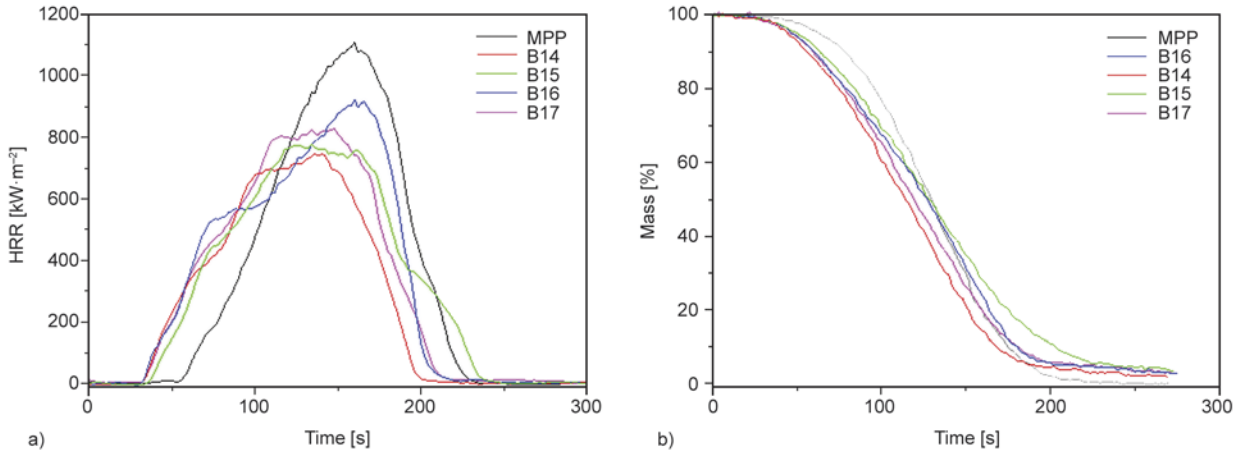


**Figure 10**. Heat release rate (a) and mass loss (b) curves of neat MPP and its blends obtained from cone calorimeter tests

**Table 9.** Cone calorimeter data of neat PP and its blends

| Sample | TTI[a] [s] | PHRR[b] [kW·m$^{-2}$] | PHRR$_t$[c] [s] | THR[d] [MJ·m$^{-2}$] | FGR[e] [kW·m$^{-2}$·s$^{-1}$] | Average SPR[f] [m$^2$·s$^{-1}$] | Char residue [wt%] |
|---|---|---|---|---|---|---|---|
| MPP | 48±3 | 1109.1±74.2 | 160±2 | 100.7±1.8 | 6.93±0.4 | 0.019±0.001 | not data |
| B14 | 24±1 | 862.8±31.2 | 130±28 | 78.4±7.1 | 6.64±1.1 | 0.021±0.003 | 2.3±0.3 |
| B15 | 29±3 | 841.0±105.4 | 159±25 | 94.9±3.4 | 5.29±1.6 | 0.022±0.001 | 3.7±0.2 |
| B16 | 24±1 | 927.9±19.5 | 163±3 | 97.6±1.3 | 5.69±0.1 | 0.022±0.002 | 3.2±0.2 |
| B17 | 25±1 | 904.3±50.1 | 139±23 | 92.4±6.5 | 6.51±1.2 | 0.021±0.002 | 3.1±0.4 |

[a]time to ignition
[b]peak of the heat release rate curve
[c]time to peak of the heat release rate curve
[d]total heat release
[e]fire growth rate
[f]average smoke production rate

slightly increased values of the averaged smoke production rate (SPR) indicated that the additives can promote smoke release to some extent. As a final remark, it was observed that the residue after combustion increased for all the blends in comparison with MPP, demonstrating that the additives can enhance the stability of the residue also in presence of oxygen.

## 4. Conclusions

The results obtained on the flammability behavior of polypropylene through the use of purposely synthesized phosphorous-containing polyvinyl alcohol polymers are reported. The characterization of blends of polypropylene and different phosphorous-modified PVA derivatives bearing aliphatic (valeroyl group) or aromatic (benzoyl group) substituents showed that phase compatibility depended on the kind of substituting groups on the PVA backbone. It was also observed that grafting of the modified PVA on MPP may occur due to radical reactions arising during melt processing. TG, cone calorimeter and LOI measurements demonstrated that thermal stability and flame retardancy of the blends was improved, confirming that the phosphate moieties can act as carbonization promoters, in particular when a suitable amount of free hydroxyl groups is present. Tensile tests demonstrated that the elastic properties of the starting MPP were slightly influenced, while plastic behaviour was negatively affected. Impact test showed that the toughness of the blends was higher than that of pure MPP, likely due to a crack deflection and twisting mechanism.

## References

[1] Bodzay B., Fejős M., Bocz K., Toldy A., Ronkay F., Marosi G.: Upgrading of recycled polypropylene by preparing flame retarded layered composite. Express Polymer Letters, **6**, 895–902 (2012).
DOI: 10.3144/expresspolymlett.2012.95

[2] Lv P., Wang Z., Hu K., Fan W.: Flammability and thermal degradation of flame retarded polypropylene composites containing melamine phosphate and pentaerythritol derivatives. Polymer Degradation and Stability, **90**, 523–534 (2005).
DOI: 10.1016/j.polymdegradstab.2005.04.003

[3] Li Q., Jiang P., Su Z., Wei P., Wang G., Tang X.: Synergistic effect of phosphorus, nitrogen, and silicon on flame-retardant properties and char yield in polypropylene. Journal of Applied Polymer Science, **96**, 854–860 (2005).
DOI: 10.1002/app.21522

[4] Fina A., Cuttica F., Camino G.: Ignition of polypropylene/montmorillonite nanocomposites. Polymer Degradation and Stability, **97**, 2619–2626 (2012).
DOI: 10.1016/j.polymdegradstab.2012.07.017

[5] Lu S-Y., Hamerton I.: Recent developments in the chemistry of halogen-free flame retardant polymers. Progress in Polymer Science, **27**, 1661–1712 (2002).
DOI: 10.1016/S0079-6700(02)00018-7

[6] Ebdon J. R., Jones M. S., Salamone J. C.: Polymeric materials encyclopedia. CRC Press, Boca Raton (1996).

[7] Bocz K., Bárány T., Toldy A., Bodzay B., Csontos I., Madi K., Marosi G.: Self-extinguishing polypropylene with a mass fraction of 9% intumescent additive – A new physical way for enhancing the fire retardant efficiency. Polymer Degradation and Stability, **98**, 79–86 (2013).
DOI: 10.1016/j.polymdegradstab.2012.10.029

[8] Chen X. L., Jiao C. M., Wang Y.: Synergistic effects of iron powder on intumescent flame retardant polypropylene system. Express Polymer Letters, **3**, 359–365 (2009).
DOI: 10.3144/expresspolymlett.2009.45

[9] Anna P., Marosi G., Bertalan G., Márton A., Szép A.: Structure–property relationship in flame retardant polymers. Journal of Macromolecular Science Part B: Physics, **41**, 1321–1330 (2002).
DOI: 10.1081/MB-120013102

[10] Fina A., Bocchini S., Camino G.: Catalytic fire retardant nanocomposites. Polymer Degradation and Stability, **93**, 1647–1655 (2008).
DOI: 10.1016/j.polymdegradstab.2008.05.027

[11] Huang N. H., Chen Z. J., Wang J. Q., Wei P.: Synergistic effects of sepiolite on intumescent flame retardant polypropylene. Express Polymer Letters, **4**, 743–752 (2010).
DOI: 10.3144/expresspolymlett.2010.90

[12] Chiang W-Y., Hu H. C-H.: Phosphate-containing flame-retardant polymers with good compatibility to polypropylene. II. Effect of the flame-retardant polymers on polypropylene. Journal of Applied Polymer Science, **82**, 2399–2403 (2001).
DOI: 10.1002/app.2090

[13] Wilkie C. A, Morgan A. B.: Fire retardancy of polymeric materials. CRC Press, Boca Raton (2010).

[14] Saucă S., Giamberini M., Reina J. A.: Flame retardant phosphorous-containing polymers obtained by chemically modifying poly(vinyl alcohol). Polymer Degradation and Stability, **98**, 453–463 (2013).
DOI: 10.1016/j.polymdegradstab.2012.07.045

[15] Banks M., Ebdon J. R., Johnson M.: Influence of covalently bound phosphorus-containing groups on the flammability of poly(vinyl alcohol), poly(ethylene-*co*-vinyl alcohol) and low-density polyethylene. Polymer, **34**, 4547–4556 (1993).
DOI: 10.1016/0032-3861(93)90163-5

[16] Avella M., Martuscelli E., Raimo M., Partch R., Gangolli S. G., Pascucci B.: Polypropylene reinforced with silicon carbide whiskers. Journal of Materials Science, **32**, 2411–2416 (1997).
DOI: 10.1023/A:1018561308695

[17] Trongtorsak K., Supaphol P., Tantayanon S.: Effect of calcium stearate and pimelic acid addition on mechanical properties of heterophasic isotactic polypropylene/ethylene–propylene rubber blend. Polymer Testing, **23**, 533–539 (2004).
DOI: 10.1016/j.polymertesting.2003.11.006

[18] Malucelli G., Priola A., Ferrero F., Quaglia A., Frigione M., Carfagna C.: Polyurethane resin-based adhesives: Curing reaction and properties of cured systems. International Journal of Adhesion and Adhesives, **25**, 87–91 (2005).
DOI: 10.1016/j.ijadhadh.2004.04.003

[19] Tomasetti E., Legras R., Henri-Mazeaud B., Nysten B.: Plastic deformation in polypropylene/(ethylene–propylene) copolymer blend during paint debonding. Polymer, **41**, 6597–6602 (2000).
DOI: 10.1016/S0032-3861(99)00885-X

[20] Weidenfeller B., Höfer M., Schilling F.: Thermal and electrical properties of magnetite filled polymers. Composites Part A: Applied Science and Manufacturing, **33**, 1041–1053 (2002).
DOI: 10.1016/S1359-835X(02)00085-4

[21] Rodionov A. G., Domareva N. M., Baulin A. A., Ponomareva Y. L., Ivanchev S. S.: Polydispersity of ethylene-propylene copolymers synthesized on supported Ziegler catalysts. Polymer Science U.S.S.R., **23**, 1724–1732 (1981).
DOI: 10.1016/0032-3950(81)90410-X

[22] Tzoganakis C., Vlachopoulos J., Hamielec A. E., Shinozaki D. M.: Effect of molecular weight distribution on the rheological and mechanical properties of polypropylene. Polymer Engineering and Science, **29**, 390–396 (1989).
DOI: 10.1002/pen.760290607

[23] Parent J. S., Bodsworth A., Sengupta S. S., Kontopoulou M., Chaudhary B. I., Poche D., Cousteaux S.: Structure–rheology relationships of long-chain branched polypropylene: Comparative analysis of acrylic and allylic coagent chemistry. Polymer, **50**, 85–94 (2009).
DOI: 10.1016/j.polymer.2008.11.014

[24] Mendrek B., Trzebicka B.: Synthesis and characterization of well-defined poly(*tert*-butyl acrylate) star polymers. European Polymer Journal, **45**, 1979–1993 (2009).
DOI: 10.1016/j.eurpolymj.2009.04.016

[25] Zhang C., Zhou Y., Liu Q., Li S., Perrier S., Zhao Y.: Facile synthesis of hyperbranched and star-shaped polymers by RAFT polymerization based on a polymerizable trithiocarbonate. Macromolecules, **44**, 2034–2049 (2011).
DOI: 10.1021/ma1024736

[26] Kaur I., Gautam N., Deepika Khanna N.: Modification of polypropylene through intercrosslinking graft copolymerization of poly(vinyl alcohol): Synthesis and characterization. Journal of Applied Polymer Science, **107**, 2238–2245 (2008).
DOI: 10.1002/app.27259

[27] Jang J., Lee D. K.: Oxygen barrier properties of biaxially oriented polypropylene/polyvinyl alcohol blend films. Polymer, **45**, 1599–1607 (2004).
DOI: 10.1016/j.polymer.2003.12.046

[28] Kontopoulou M., Wang W., Gopakumar T. G., Cheung C.: Effect of composition and comonomer type on the rheology, morphology and properties of ethylene-α-olefin copolymer/polypropylene blends. Polymer, **44**, 7495–7504 (2003).
DOI: 10.1016/j.polymer.2003.08.043

[29] Yamaguchi M., Miyata H., Nitta K-H.: Compatibility of binary blends of polypropylene with ethylene-α-olefin copolymer. Journal of Applied Polymer Science, **62**, 87–97 (2003).
DOI: 10.1002/(SICI)1097-4628(19961003)62:1<87::AID-APP12>3.0.CO;2-5

[30] De Rosa C., Auriemma F., Spera C.: Comparison between polymorphic behaviors of Ziegler-Natta and metallocene-made isotactic polypropylene: The role of the chain microstructure. Macromolecular Symposia, **218**, 113–124 (2004).
DOI: 10.1002/masy.200451412

[31] Yan H., Chen Y.: Blends of polypropylene and hyperbranched poly(phenylene sulphide) for production of dyeable PP fibres. Iranian Polymer Journal, **19**, 791–799 (2010).

[32] Vranjes N., Rek V.: Effect of EPDM on morphology, mechanical properties, crystallization behavior and viscoelastic properties of iPP+HDPE blends. Macromolecular Symposia, **258**, 90–100 (2007).
DOI: 10.1002/masy.200751210

[33] Jain S., Goossens H., van Duin M., Lemstra P.: Effect of *in situ* prepared silica nano-particles on non-isothermal crystallization of polypropylene. Polymer, **46**, 8805–8818 (2005).
DOI: 10.1016/j.polymer.2004.12.062

[34] Willbourn H.: The glass transition in polymers with the $(CH_2)_n$ group. Transactions of the Faraday Society, **54**, 717–729 (1958).
DOI: 10.1039/tf9585400717

[35] Ratanakamnuan U., Aht-Ong D.: Preparation and characterization of low-density polyethylene/banana starch films containing compatibilizer and photosensitizer. Journal of Applied Polymer Science, **100**, 2717–2724 (2006).
DOI: 10.1002/app.23047

[36] Persico P., Ambrogi V., Carfagna C., Cerruti P. Ferrocino I., Mauriello G.: Nanocomposite polymer films containing carvacrol for antimicrobial active packaging. Polymer Engineering and Science, **49**, 1447–1455 (2009).
DOI: 10.1002/pen.21191

[37] Hong C. H., Lee Y. B., Bae J. W., Jho J. Y., Nam B. U., Hwang T. W.: Preparation and mechanical properties of polypropylene/clay nanocomposites for automotive parts application. Journal of Applied Polymer Science, **98**, 427–435 (2005).
DOI: 10.1002/app.21800

[38] Luda M. P., Brunella V., Guaratto D.: Characterisation of used PP-based car bumpers and their recycling properties. ISRN Materials Science, **2013**, 531093/1–531093/12 (2013).
DOI: 10.1155/2013/531093

[39] Ritchie R. O.: The conflicts between strength and toughness. Nature Materials, **10**, 817–822 (2011).
DOI: 10.1038/nmat3115

[40] Shao Z-B., Deng C., Tan Y., Yu L., Chen M-J., Chen L., Wang Y-Z.: Ammonium polyphosphate chemically-modified with ethanolamine as an efficient intumescent flame retardant for polypropylene. Journal of Materials Chemistry A, **2**, 13955–13965 (2014).
DOI: 10.1039/c4ta02778g

[41] Breulet H., Steenhuizen T.: Fire testing of cables: Comparison of SBI with FIPEC/Europacable tests. Polymer Degradation and Stability, **88**, 150–158 (2005).
DOI: 10.1016/j.polymdegradstab.2004.01.031

*eXPRESS Polymer Letters Vol.9, No.4 (2015) 344–353*
*Available online at www.expresspolymlett.com*
*DOI: 10.3144/expresspolymlett.2015.32*

# Tailoring the mechanical and thermal properties of dicyclopentadiene polyHIPEs with the use of a comonomer

*E. H. Mert*[1*], *C. Slugovc*[2], *P. Krajnc*[3]

[1]Yalova University, Faculty of Engineering, Polymer Engineering Department, 77100 Yalova, Turkey
[2]Graz University of Technology, Institute for Chemistry and Technology of Materials, Stremayrgasse 9, A-8010 Graz, Austria
[3]University of Maribor, Faculty of Chemistry and Chemical Engineering, PolyOrgLab, Smetanova 17, Maribor, Slovenia

*Received 30 June 2014; accepted in revised form 12 October 2014*

**Abstract.** The effect of adding a comonomer to dicyclopentadiene in high internal phase emulsions (HIPEs) on the properties of ring-opening metathesis polymerisation (ROMP) derived polyHIPEs has been investigated. With this aim, dicylopentadiene was copolymerised with norbornene in surfactant stabilized high internal phase emulsions. Morphological, mechanical and thermal properties of the resulting materials were investigated with regard to the monomer ratio. The interconnected pore structure was observed for the resulting poly(dicylopentadiene-*co*-norbornene) polyHIPEs. Furthermore, the new polyHIPE copolymers were found to have an improved thermal stability compared to the poly(dicylopentadiene) homopolymer.

***Keywords:*** *mechanical properties, emulsion templating, polyHIPE, dicyclopentadiene, norbornene*

## 1. Introduction

Emulsion templating is an effective method to prepare open porous polymers with well-defined morphology and properties such as low density, high porosity and interconnected pore structure. In recent years, microcellular polymers obtained from high internal phase emulsions (HIPEs) have attracted considerable attention [1–4]. A HIPE is an emulsion with an internal phase volume ratio greater than 74% of the total emulsion volume [5–8], although some definitions refer to HIPEs at lower internal phase ratios [9]. Polymerisation of the HIPE continuous phase and the subsequent removal of the dispersed phase leads to the formation of a monolithic porous polymer, usually termed a polyHIPE. The majority of reports describe polyHIPE preparation from the radical polymerisation of hydrophobic monomers; the most widely studied monomer system being styrene and divinylbenzene (DVB) [10, 11]. However, in order to expand the applications of polyHIPEs, a variety of more hydrophilic monomers have been studied including; 4-vinylbenzene chloride (VBC) [12–14], 4-nitrophenyl acrylate (NPA) [15], 2-hydroxyethyl methacrylate (HEMA) [16], acryl amide (AAm) [17], glycidyl methacrylate (GMA) and ethylene glycol dimethacrylate (EGDMA) [18–20]. In recent years, the preparation of polyHIPEs via oil-in-water (o/w) templates has attracted attention despite the difficulties in achieving a stable emulsion [1]. For instance poly(acrylic acid) polyHIPEs have been prepared by Krajnc *et al.* [21] from an o/w HIPE consisting of acrylic acid. More recently, Pulko and Krajc [4] succeeded to prepare hierarchically porous functional polyHIPEs from acryl amide (AAm) by using water soluble surfactants. While the majority of polyHIPEs are

*Corresponding author, e-mail: hmert@yalova.edu.tr

produced from radical chain growth polymerisations there are examples of step growth polymerisation as demonstrated by Lovelady *et al*. [22], Caldwell *et al*. [23] and Sergent *et al*. [24] who have used the fast kinetics of thiol-ene reaction to rapidly build the polymer network via a step growth mechanism. This was also successfully utilized for macro structuring of polyHIPEs via layer-by-layer photopolymerisation [25, 26]. Moreover, the use of ring-opening metathesis reactions (ROMP) has also been successfully applied for the preparation of polyHIPEs [27–29]. Cyclic monomers, such as dicyclopentadiene (DCPD) were used and a one-pot procedure for the further functionalization of the polyHIPEs via the residual double bonds by thiol-ene reaction was developed [29, 30]. Recently, a polyHIPE membrane produced by ROMP of DCPD and norbornene has been utilised as a separator in Li-ion batteries [31] and in another study macroporous polyolefin membranes were prepared by using the same approach [32].

PolyHIPEs have been explored for a wide range of applications [31–39]. However, the poor mechanical strength originated from the highly porous and interconnected morphology is the major deficiency restricting the commercial applications. In the last decade, as well as a few studies have tried to address this issue, the poor mechanical properties of polyHIPEs are still required to be improved [40–42].

So far, in order to increase the mechanical strength of polyHIPEs several methods such as changing the polymerisable monomomer(s) and cross-linker comonomer, introducing a suitable reinforcement into the continuous phase or increasing the foam density have been used by scientists. However, increasing the foam density is not preferred since most of the applications of these materials required low density [39]. Within this context, Wu *et al*. [43] reported the preparation of nanoparticle reinforced polyHIPEs with reduced brittleness and chalkiness by using a stress-reducing cross-linker. More recently, Ikem *et al*. [44] synthesised polyHIPEs with increased compressive modulus and compressive strength from titania-particle-stabilized emulsion templates. Moreover, open porous architectures based on polyDCPD via ROMP with very favourable mechanical resilience and the highest *E*-moduli of polyHIPE materials of the respective porosity reported was demonstrated [29, 30, 41, 42].

Herein, the effect of the presence of a comonomer in the polymer matrix on the morphological features, mechanical strength and thermal stability of the polyHIPEs based on poly(dicylopentadiene) (polyDCPD) have been investigated. With this intent polyHIPEs have been prepared by incorporating various amounts of norbornene (NBE) into the polymer matrix. Moreover, ring-opening metathesis polymerisation (ROMP) has been used in order to accomplish an unsaturated polymer chain for further post-functionalization applications. The change of the above mentioned properties with the NBE amount is discussed.

## 2. Experimental section

### 2.1. Materials

Dicyclopentadiene (Aldrich, DCPD), norbornene (Merck, NBE), Pluronic PEL121 (poly(ethylene glycol)-block-poly(propylene glycol)-block-poly (ethylene glycol) copolymer) (Aldrich), Toluene (Carlo Erba) were used without further purification. M2 ($(H_2IMes)(PCy_3)Cl_2Ru$(3-phenyl-indenylid-1-ene) with $H_2IMes$=N,N-bis(mesityl)4,5-dihydroimidazol-2-yl, $PCy_3$=tricyclohexylphosphine) was obtained from UMICORE.

### 2.2. PolyHIPE Preparation

PolyHIPE samples were prepared from DCPD and NBE monomer mixtures. The example given here is for poly(DCPD-*co*-NBE) polymer of 90/10 (molar) ratio of DCPD/NBE, 80 vol% porosity, 5 vol% of surfactant and 0.015 mol% of initiator. These values were changed by altering the DCPD to NBE ratio between 100/0 and 10/90 (molar). DCPD (49.5 mmol, 6.64 mL), NBE (5.5 mmol, 0.61 mL) and Pluronic L121 (0.36 mL) were added to a 250 mL two-necked round bottom flask. The mixture was stirred at approx. 400 rpm with an overhead stirrer. The aqueous phase composed of deionised water (28.9 mL) was added drop-wise with constant stirring. Once the aqueous phase was added, the mixture was stirred for further 1 h followed by the addition of the initiator (M2) (0.015 mol% with regards to monomer mixture) (see Figure 1). Afterwards, the emulsion was transferred to a polyethylene mould and cured at 80°C for 5 h. The resulting polyHIPE was purified via Soxhlet extraction (ethanol, for 24 h) and dried in vacuum at room temperature.

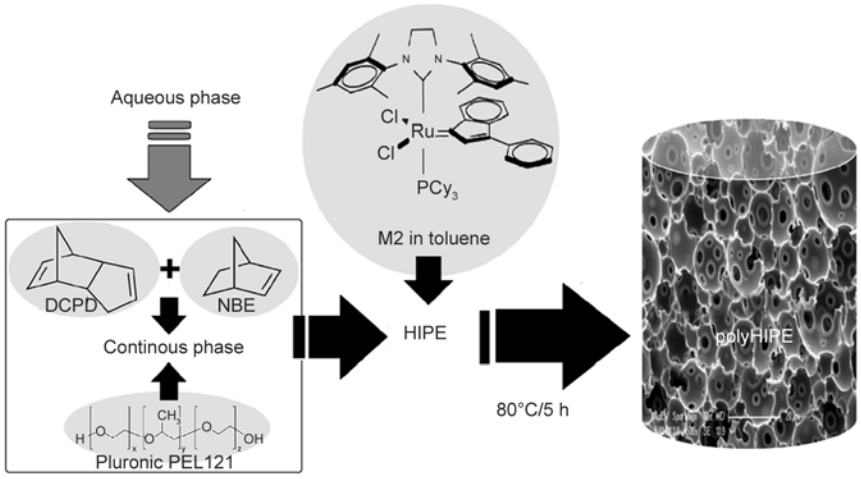


**Figure 1.** Preparation of poly(DCPD-*co*-NBE) polyHIPEs

## 2.3.Characterisation

The morphology of the resulting polyHIPEs was observed by scanning electron microscopy (SEM) using ESEM-FEG and EDAX Philips XL-30 microscope (Philips, Eindhoven, The Netherlands). As the resulting materials were too though and hard to break or cut, the SEM images were taken from the polymer pieces obtained by crushing the polyHIPEs in liquid nitrogen. In each measurement polyHIPE pieces were mounted on a copper stub and a thin layer of gold was sputtered on the samples prior to analysis. Average cell diameters and interconnecting pore diameters were measured from SEM images. Over 50 measurements were taken from each SEM image and the average value was corrected with a correction factor ($2/3^{1/2}$) to account for irregular cutting of the samples [45].

Specific surface areas and cumulative pore volumes were measured at Central Laboratory of the Middle East Technical University (Ankara, Turkey) with Quantachrome's Autosorb-6B Surface Area and Pore Size Analyzer (Quantachrome GmbH & Co. KG, Germany) by applying the Brunauer–Emmet–Teller (BET) molecular adsorption method. Prior to analysis, samples were degassed for 24 h at room temperature.

Mechanical strengths of the polyHIPEs were measured by performing uniaxial compression experiment with a Zwick/Roell Z020 Universal Testing Machine (Zwick GmbH & Co.KG, Germany) equipped with a 10 kN load cell. Compression tests were carried out according to the industrial standard ASTM D1621-2004. For each polyHIPE sample five specimen, which were 25 mm in diameter and 10 mm high, were tested at a compression rate of 1.3 mm/min. The compression modulus and compressive strength were obtained from the original output of the instrument.

Thermogravimetric analysis (TGA) of the polyHIPEs were performed on a Seiko TG/DTA 6300 thermal analysis system instrument (Seiko Instruments Inc., Tokyo, Japan) under nitrogen flow with a heating rate of 10°C/min. The differential scanning calorimeter (DSC) measurements were performed on a Seiko DSC 7020 calorimeter (Seiko Instruments Inc., Tokyo, Japan) to measure glass transition temperatures of the samples by using instrument at a heating rate of 10°C/min. During DSC measurements, two heating and one cooling curves were recorded for each sample in a temperature range from 10 to 300°C and the heat flow was measured.

## 3. Results and discussion

The advantages of using a cyclic monomer for polyHIPE preparation are already known from recent studies [27–30, 41, 42]. Particularly, polyHIPEs prepared by ROMP of DCPD are unique members of emulsion templated open-porous materials. The key feature of such materials is that they can be produced by crosslinking of the monomer through olefin metathesis without using an additional cross-linker. NBE was chosen as a comonomer because it does not bear a second cyclic double bond thus the overall material's crosslinking degree is reduced. However, changed polymer structure is expected to have an effect on the mechanical properties of the product while the emulsion templating procedure needs optimization due to changed formulation of the oil phase. On the other hand, it is also required to investigate the influence of comonomer incorpora-

tion in order to understand the variability of the properties with the change of monomer composition. Herein, we focused on the determination of the alternation of morphological, thermal and mechanical properties of polyDCPD polyHIPEs in the presence of a comonomer (NBE).

For investigation of morphological, mechanical and thermal properties freshly prepared samples were used. Morphology of the resulting polyHIPEs was investigated by SEM and the SEM micrographs of the materials are presented in Figure 2. In all cases, addition of NBE eventuated with polymers having spherical cells interconnected with minor pores. Average cell diameters and pore sizes were calculated from SEM images by taking over 50 measurements and the results are presented in Table 1. There was no significant change in the size of interconnecting pores comparing neat polyDCPD with norbornene containing copolymers. The change of cavity diameters on the other hand, was more remarkable then the change in interconnected pore sizes. It was found that the addition of NBE increases the cavity diameters between 40 and 52% depending on the NBE content of each copolymer sample (c.f. Table 1). This reflects the changed polarity of the oil phase and thus larger droplets are obtained during the emulsion preparation which yields the material with larger cavities. It has to be noted that the surfactant and the surfactant concentration was kept identical for all prepared samples (Pluronic L121; 5 vol% to oil phase). Additionally, specific surface area and cumulative pore volumes of the resulting materials were determined from nitrogen adsorption/desorption isotherms using the BET model and the results are presented in Table 1. Surface areas of the poly(DCPD/NBE) copolymers were decreased compared to the polyDCPD by approximately twofold, which is a consequence of the increase of cavity diameters.

Since oxidation is the major factor that causes the loss of mechanical strength it is important to investigate the mechanical features through unoxidized samples. Thus, mechanical tests were performed with freshly prepared, unoxidized polyHIPEs by applying compression tests under 10 kN compressive load. Figure 3 demonstrates the standard force [kPa]/compression ratio [%] curves obtained from the test samples, while the Table 2 summarizes the data obtained from the original software during the measurements. The similar curves having initial linear elasticity and plateau can be accepted as the evidence of classical foam behavior. At small strains, usually less than ca. 6%, the behavior is linear elastic, with a slope equal to the compressive modulus. At higher loads the cavities of the foams begin to collapse and give a stress plateau. The characteristic maximum at the end of the linear elasticity region was used to determine the compressive strength.

The addition of NBE leads to increase of compression modulus and compressive strength. It was found that addition of 50 mol% of NBE increases the compression modulus by ca. 55%. However, when the ratio of NBE exceeded 50 mol% the compression modulus decreased. It was found that, as compared to P6 the compression modulus of P7 decreased from 69.4 to 56.2 MPa. An increase in the NBE ratio from 60 to 90 mol% resulted in an irregular decrease of the compression modulus for the P8, P9 and P10. Additionally, in accordance with the compressive modulus, sample P6 was found to have the maximum compressive strength. Finally, the compression modulus and compressive strength of P10 was found to comparable with P1.

**Table 1.** Morphological characterisation of polyDCPD homopolymer and poly(DCPD/NBE) copolymers.

| Sample | DCPD [mol%] | NBE [mol%] | Surface area [$m^2 \cdot g^{-1}$] | Cavity diameter [µm] | Pore diameter [µm] | $V_p^c$ [$mL \cdot g^{-1}$] |
|---|---|---|---|---|---|---|
| P1 | 100 | 0 | 7.34±1.4 | 6.48±0.2 | 2.22±0.1 | 5.30±2.4 |
| P2 | 90 | 10 | 4.67±0.3 | 11.50±0.9 | 2.20±0.1 | 6.60±3.5 |
| P3 | 80 | 20 | 5.17±0.6 | 12.81±1.1 | 2.27±0.1 | 6.90±2.6 |
| P4 | 70 | 30 | 5.80±0.2 | 12.85±1.1 | 2.27±0.1 | 6.70±2.5 |
| P5 | 60 | 40 | 4.20±0.1 | 13.38±1.3 | 2.25±0.1 | 6.70±2.0 |
| P6 | 50 | 50 | 5.56±1.6 | 13.76±0.9 | 2.45±0.1 | 7.30±6.3 |
| P7 | 40 | 60 | 5.90±0.8 | 12.87±1.1 | 2.43±0.1 | 7.30±2.2 |
| P8 | 30 | 70 | 3.87±0.1 | 8.23±0.2 | 2.36±0.1 | 7.60±0.1 |
| P9 | 20 | 80 | 4.68±0.6 | 10.12±0.6 | 2.34±0.1 | 7.20±1.9 |
| P10 | 10 | 90 | 4.18±0.1 | 10.51±0.4 | 2.45±0.1 | 6.90±1.9 |

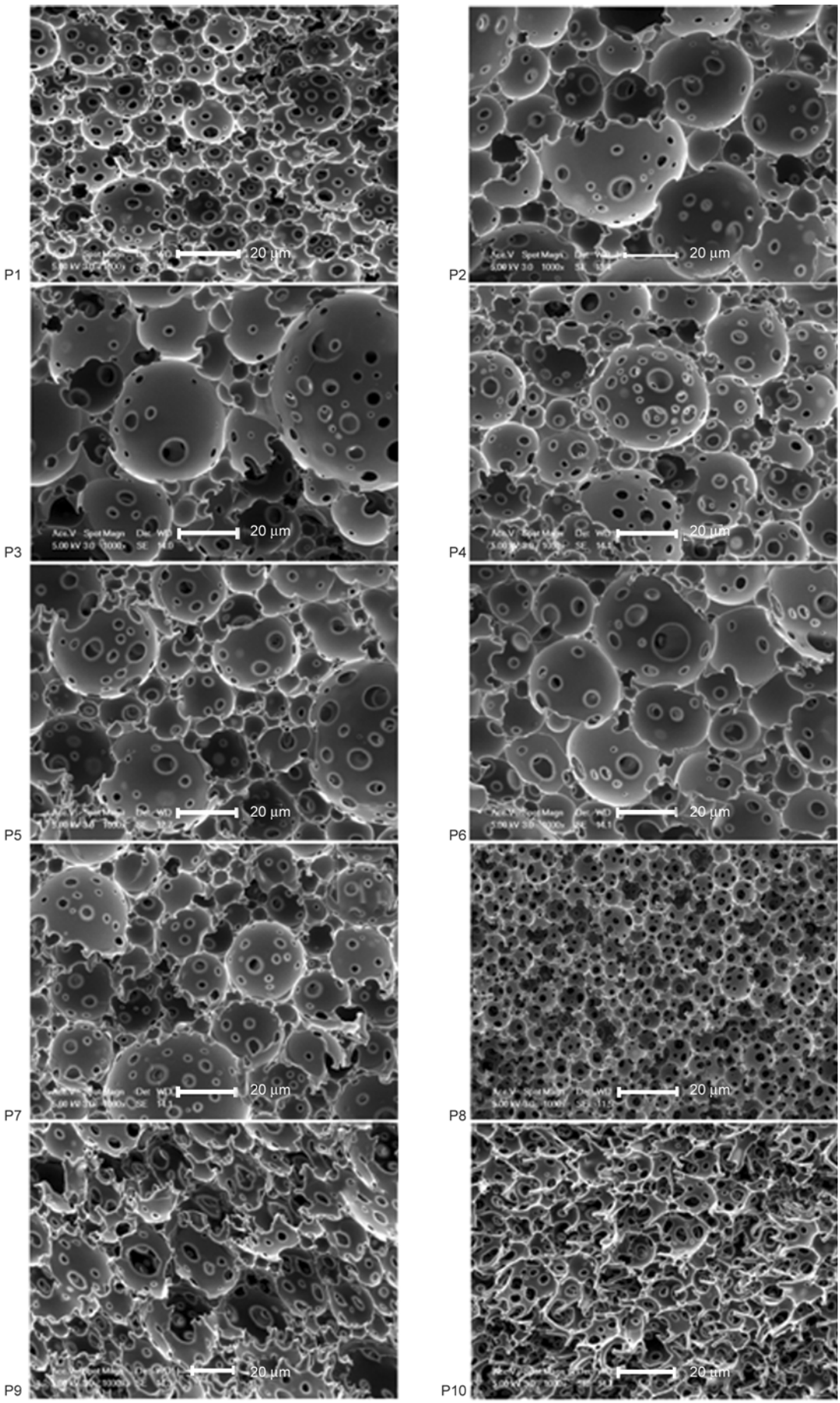


**Figure 2.** SEM images of the polyDCPD homopolymer (P1) and poly(DCPD/NBE) copolymers (P2–P10)

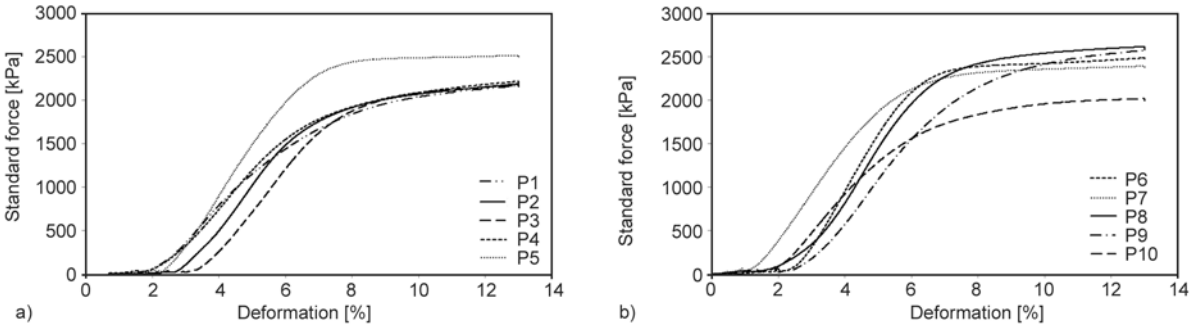


**Figure 3.** Mechanical characterization of polyDCPD homopolymer (P1) (a) and poly(DCPD/NBE) copolymers (P2–P10) (a, b)

**Table 2.** Mechanical and thermal characterization of polyDCPD homopolymer (P1) and poly(DCPD/NBE) copolymers (P2–P10)

| Sample | $E_c$ [a] [MPa] | $\sigma_M$ [b] [MPa] | $T_{d5}$ [°C] | $T_{d10}$ [°C] | $T_{d50}$ [°C] | $V_{max}$ at $T_{max}$ [%·min$^{-1}$] at [°C] | Char [wt%] | $T_g$ [°C] |
|---|---|---|---|---|---|---|---|---|
| P1 | 44.6 | 1.0 | 144.9 | 222.3 | 446.7 | 5.39 at 448.5 | 29.1 | – |
| P2 | 50.7 | 1.5 | 274.8 | 372.5 | 458.7 | 11.67 at 467.3 | 15.5 | 188.2 |
| P3 | 49.7 | 1.6 | 346.5 | 397.1 | 453.6 | 12.61 at 462.2 | 19.8 | 145.6 |
| P4 | 46.6 | 1.4 | 346.4 | 394.6 | 461.8 | 13.19 at 465.7 | 17.0 | 130.6 |
| P5 | 62.4 | 1.7 | 276.7 | 359.7 | 452.4 | 11.56 at 462.5 | 15.3 | 125.0 |
| P6 | 69.4 | 1.8 | 278.1 | 367.5 | 453.5 | 13.10 at 457.4 | 11.3 | 111.4 |
| P7 | 56.2 | 1.6 | 389.8 | 413.8 | 462.6 | 14.14 at 462.0 | 11.1 | 85.6 |
| P8 | 65.2 | 1.8 | 309.6 | 387.8 | 454.3 | 13.98 at 456.0 | 5.6 | 70.2 |
| P9 | 53.0 | 1.5 | 392.0 | 411.7 | 457.1 | 15.07 at 455.9 | 7.7 | 82.7 |
| P10 | 46.4 | 1.1 | 393.9 | 415.4 | 452.9 | 16.90 at 460.9 | 0.6 | 61.0 |

[a] $E_c$: compression modulus; [b] $\sigma_M$: compressive strength

Thermal stability of polyDCPD homopolymer and poly(DCPD/NBE) copolymers were investigated by thermal gravimetric analysis (TGA). The curves obtained from TGA are presented in Figure 4 and Figure 5. Table 2, on the other hand summarizes the decomposition temperatures at 5, 10, 50% weight loss ($T_{d5}$, $T_{d10}$, $T_{d50}$), maximum rate of decomposition ($V_{max}$), temperature of maximum rate of decomposition ($T_{max}$) and residual char at 550°C. As can be seen from Figure 4, polyDCPD homopolymer (P1) shows three stage decomposition and a continuous mass loss up to c.a. 500°C. The mass loss at 60°C can be explained by the water trapped within the cavities. On the other hand, polyDCPD homopolymer (P1) starts to lose mass slightly at 150°C and then continuous degradation begins. The largest mass loss occurred between 400 and 475°C. In the case of copolymers (P2 to P10), the slight mass loss starts above 150°C and significant mass loss occurred between 400 and 500°C. Consisting with the literature, this stage indicates the rapid degradation of norbornene chains in the copolymer matrix [46]. In Table 2, $T_{d5}$ and $T_{d10}$ indicate the onset degradation temperatures and $T_{d50}$ is the mid-

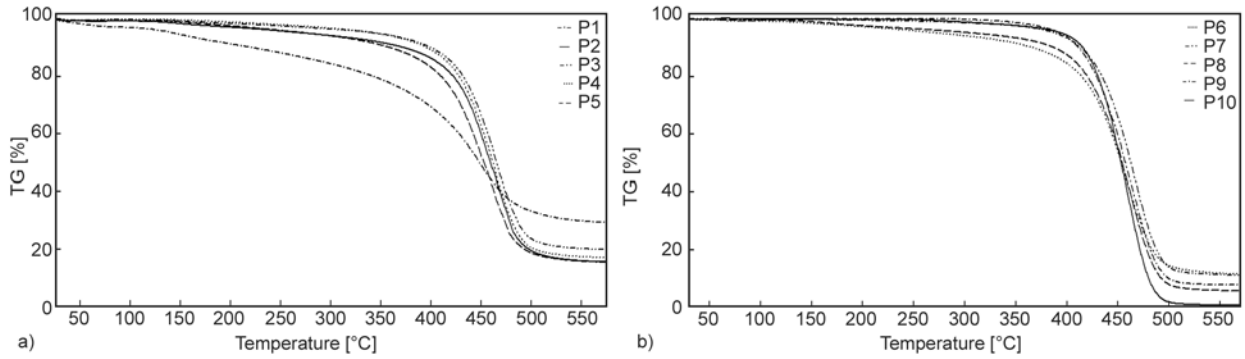


**Figure 4.** The comparative curves for thermal decomposition of polyHIPEs obtained from TGA: P1–P5 (a) and P6–P10 (b)

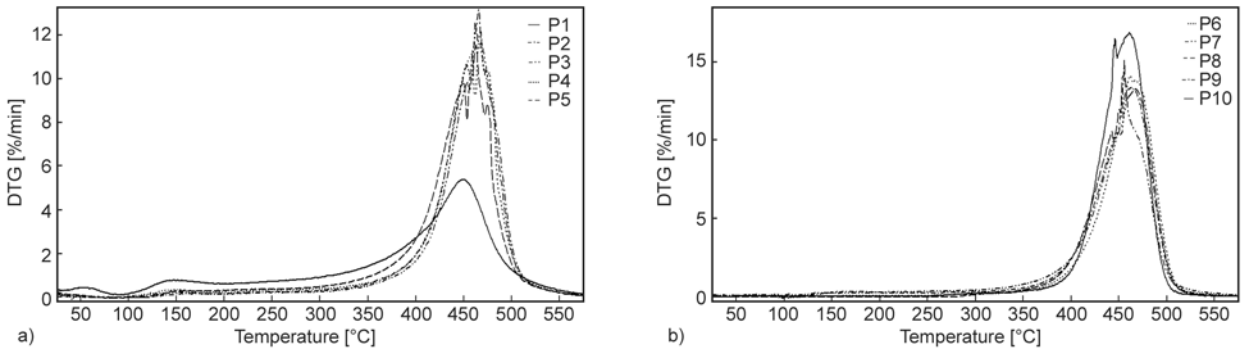


**Figure 5.** The comparative DTG thermograms of the resulting polyHIPEs: P1–P5 (a) and P6–P10 (b)

point degradation temperature. As shown in Table 2, the increases of the onset degradation temperatures ($T_{d5}$, $T_{d10}$) and as well as the midpoint degradation temperature ($T_{d50}$) indicated enhanced thermal stability of poly(DCPD/ NBE) copolymers (P2 to P10) compared with polyDCPD homopolymer (P1).

On the other hand, the copolymerisation of increasing NBE amounts caused an increase of the maximum degradation rate. Table 2 indicates that as well as the maximum degradation temperature increased slightly, the increase of the maximum degradation rate was more remarkable. As compared with the polyDCPD matrix the maximum degradation rate was increased up to 11.5% for the poly(DCPD/ NBE) copolymers. Accordingly, there is also a significant deterioration of 97.9% lower char yield than polyDCPD matrix. TGA analyses confirm that NBE amount has a remarkable influence on the degradation behaviour. In comparison with the polyDCPD matrix, polymer backbones decomposed more rapidly at considerably high temperatures for poly (DCPD/NBE) copolymers. This may be explained by the fact that NBE and DCPD units possess different structures and degradation of poly(DCPD/NBE) copolymers requires different energy to occur.

It is known from the literature the $T_g$ value of polyDCPD is usually ranged between 140 and 160°C, depending on the amount of crosslinked units [47]. However, incorporation of a comonomer into polyDCPD leads to change in glass transition temparature values depending on the nature of the comonomer. The effect of polymer backbone chemistry onto glass transitions of the polyDCPD homopolymer and the resulting copolymers was examined by DSC. The curves obtained from DSC are presented in Figure 6. However we didn't observe any thermal transition for pure polyDCPD matrix (P1) most probably due to the highly cross-linked structure. In all cases of copolymers DSC curves showed only one single glass transition. Consequently, it was confirmed that no phase separated blocks of the mononers were built. By copolymerisation with norbornene, copolymers with glass transition temperatures between 61 and 188°C were obtained. With increasing the content of NBE the $T_g$ values of the copolymers were gradually decreased. In particular, 127°C decrease in $T_g$ was observed for the copolymer prepared by incorporating 90 mol% of NBE (P10) as compared to copolymer sample having 10 mol% of NBE (P2). The decrease in the $T_g$ can be explained by the presence

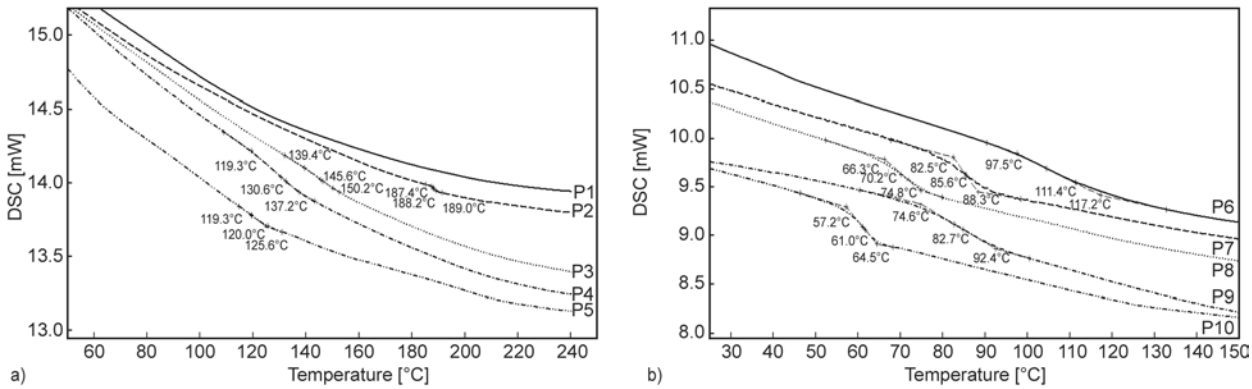


**Figure 6.** The comparative DSC curves of polyHIPEs: P1–P5 (a) and P6–P10 (b)

of NBE units in the resulting copolymers. It is known from the literature that $T_g$ of polyNBE range between 20 and 40°C [48]. Consequently, the increase in NBE quantity leads to increased flexibility in the polymer backbone and decreased glass transition temperature ($T_g$).

## 4. Conclusions

In this paper, we have demonstrated the effect of using a comonomer on the properties of dicyclopentadiene polyHIPEs. Since norbornene can be cross-linked via ROMP and possesses only one double bond, norbornene was used as comonomer. The effect of monomer composition on morphological, mechanical and thermal properties was explored by varying the norbornene composition in HIPEs. By incorporating norbornene into the polymer matrix polyHIPEs exhibited enhanced thermal properties without compromising the morphological features. Moreover, it was found that as compared with the pure polyDCPD matrix addition of 50 mol% of NBE into the polymer matrix increases the compression modulus and compressive strength ca. 55% and ca. 73%, respectively. On the other hand, incorporation of a comonomer into the polymer matrix and its amount has a remarkable effect on the thermal degradation behavior. The onset degradation temperatures were found to increase significantly with the increasing amount of comonomer. Moreover, as compared with the pure polyDCPD matrix, polymer backbones decomposed more rapidly at considerably higher temperatures.

## References


[1] Kimmins S. D., Cameron N. R.: Functional porous polymers by emulsion templating: Recent advances. Advanced Functional Materials, **21**, 221–225 (2011). DOI: 10.1002/adfm.201001330

[2] Silverstein M. S.: PolyHIPEs: Recent advances in emulsion-templated porous polymers. Progress in Polymer Science, **39**, 199–234 (2014). DOI: 10.1016/j.progpolymsci.2013.07.003

[3] Tebboth M., Menner A., Kogelbauer A., Bismarck A.: Polymerised high internal phase emulsions for fluid separation applications. Current Opinion in Chemical Engineering, **4**, 114–120 (2014). DOI: 10.1016/j.coche.2014.03.001

[4] Pulko I., Krajnc P.: High internal phase emulsion templating – A path to hierarchically porous functional polymers. Macromolecular Rapid Communications, **33**, 1731–1746 (2012). DOI: 10.1002/marc.201200393

[5] Bartl H., von Bonin W.: Über die polymerisation in umgekehrter emulsion. Die Makromolekulare Chemie, **57**, 74–95 (1962). DOI: 10.1002/macp.1962.020570105

[6] Bartl H., von Bonin W.: Über die polymerisation in umgekehrter emulsion. II. Die Makromolekulare Chemie, **66**, 151–156 (1963). DOI: 10.1002/macp.1963.020660115

[7] Lissant K. J., Peace B. W., Wu S. H., Mayhan K. G.: Structure of high-internal-phase-ratio emulsions. Journal of Colloid and Interface Science, **47**, 416–423 (1974). DOI: 10.1016/0021-9797(74)90273-2

[8] Lissant K. J., Mayhan K. G.: A study of medium and high internal phase ratio water/polymer emulsions. Journal of Colloid and Interface Science, **42**, 201–208 (1973). DOI: 10.1016/0021-9797(73)90025-8

[9] Lissant K. J.: Emulsions and emulsion technology. Marcel Dekker, New York (1984).

[10] Cameron N. R., Sherrington D. C., Ando I., Kurosu H.: Chemical modification of monolithic poly(styrene–divinylbenzene) polyHIPE® materials. Journal of Materials Chemistry, **6**, 719–726 (1996). DOI: 10.1039/JM9960600719

[11] Mercier A., Deleuze H., Mondain-Monval O.: Preparation and functionalization of (vinyl)polystyrene polyHIPE®.: Short routes to binding functional groups through a dimethylene spacer. Reactive and Functional Polymers, **46**, 67–79 (2000). DOI: 10.1016/S1381-5148(00)00040-7

[12] Barbetta A., Cameron N. R., Cooper S. J.: High internal phase emulsions (HIPEs) containing divinylbenzene and 4-vinylbenzyl chloride and the morphology of the resulting polyHIPE materials. Chemical Communications, **2000**, 221–222 (2000). DOI: 10.1039/A909060F

[13] Štefanec D., Krajnc P.: 4-vinylbenzyl chloride based porous spherical polymer supports derived from water-in-oil-in-water emulsions. Reactive and Functional Polymers, **65**, 37–45 (2005). DOI: 10.1016/j.reactfunctpolym.2005.01.007

[14] Kovačić S., Krajnc P.: Macroporous monolithic poly(4-vinylbenzyl chloride) columns for organic synthesis facilitation by *in situ* polymerization of high internal phase emulsions. Journal of Polymer Science Part A: Polymer Chemistry, **47**, 6726–6734 (2009). DOI: 10.1002/pola.23732

[15] Krajnc P., Štefanec D., Brown J. F., Cameron N. R.: Aryl acrylate based high-internal-phase emulsions as precursors for reactive monolithic polymer supports. Journal of Polymer Science Part A: Polymer Chemistry, **43**, 296–303 (2005). DOI: 10.1002/pola.20501

[16] Kovačič S., Štefanec D., Krajnc P.: Highly porous open-cellular monoliths from 2-hydroxyethyl methacrylate based high internal phase emulsions (HIPEs): Preparation and void size tuning. Macromolecules, **40**, 8056–8060 (2007).
DOI: 10.1021/ma071380c

[17] Zhang H., Cooper A. I.: Synthesis of monodisperse emulsion-templated polymer beads by oil-in-water-in-oil (O/W/O) sedimentation polymerization. Chemistry of Materials, **14**, 4017–4020 (2002).
DOI: 10.1021/cm0206643

[18] Pulko I., Smrekar V., Podgornik A., Krajnc P.: Emulsion templated open porous membranes for protein purification. Journal of Chromatography A, **1218**, 2396–2401 (2011).
DOI: 10.1016/j.chroma.2010.11.069

[19] Barbetta A., Dentini M., Leandri L., Ferraris G., Coletta A., Bernabei M.: Synthesis and characterization of porous glycidylmethacrylate–divinylbenzene monoliths using the high internal phase emulsion approach. Reactive and Functional Polymers, **69**, 724–736 (2009).
DOI: 10.1016/j.reactfunctpolym.2009.05.007

[20] Yao C., Qi L., Jia H., Xin P., Yang G., Chen Y.: A novel glycidyl methacrylate-based monolith with sub-micron skeletons and well-defined macropores. Journal of Materials Chemistry, **19**, 767–772 (2009).
DOI: 10.1039/B816712E

[21] Krajnc P., Štefanec D., Pulko I.: Acrylic acid 'reversed' polyHIPEs. Macromolecular Rapid Communications, **26**, 1289–1293 (2005).
DOI: 10.1002/marc.200500353

[22] Lovelady E., Kimmins S. D., Wu J., Cameron N. R.: Preparation of emulsion-templated porous polymers using thiol–ene and thiol–yne chemistry. Polymer Chemistry, **2**, 559–562 (2011).
DOI: 10.1039/C0PY00374C

[23] Caldwell S., Johnson D. W., Didsbury M. P., Murray B. A., Wu J. J., Przyborski S. A., Cameron N. R.: Degradable emulsion-templated scaffolds for tissue engineering from thiol–ene photopolymerisation. Soft Matter, **8**, 10344–10351 (2012).
DOI: 10.1039/C2SM26250A

[24] Sergent B., Birot M., Deleuze H.: Preparation of thiol–ene porous polymers by emulsion templating. Reactive and Functional Polymers, **72**, 962–966 (2012).
DOI: 10.1016/j.reactfunctpolym.2012.02.011

[25] Sušec M., Ligon S. C., Stampfl J., Liska R., Krajnc P.: Hierarchically porous materials from layer-by-layer photopolymerization of high internal phase emulsions. Macromolecular Rapid Communications, **34**, 938–943 (2013).
DOI: 10.1002/marc.201300016

[26] Johnson D. W., Sherborne C., Didsbury M. P., Pateman C., Cameron N. R., Claeyssens F.: Macrostructuring of emulsion-templated porous polymers by 3D laser patterning. Advanced Materials, **25**, 3178–3181 (2013).
DOI: 10.1002/adma.201300552

[27] Deleuze H., Faivre R., Herroguez V.: Preparation and functionalisation of emulsion-derived microcellular polymeric foams (polyHIPEs) by ring-opening metathesis polymerisation (ROMP). Chemical Communications, **2002**, 2822–2823 (2002).
DOI: 10.1039/B208832K

[28] Benmachou K., Deleuze H., Herroguez V.: Ring opening polymerisation of highly concentrated inverse emulsions to obtain microcellular foams. Reactive and Functional Polymers, **55**, 211–217 (2003).
DOI: 10.1016/S1381-5148(02)00248-1

[29] Kovačič S., Krajnc P., Slugovc C.: Inherently reactive polyHIPE material from dicyclopentadiene. Chemical Communications, **46**, 7504–7506 (2010).
DOI: 10.1039/C0CC02610G

[30] Kovačič S., Jeřábek K., Krajnc P., Slugovc C.: Ring opening metathesis polymerisation of emulsion templated dicyclopentadiene giving open porous materials with excellent mechanical properties. Polymer Chemistry, **3**, 325–328 (2012).
DOI: 10.1039/C2PY00518B

[31] Kovačič S., Kren H., Krajnc P., Koller S., Slugovc C.: The use of an emulsion templated microcellular poly (dicyclopentadiene-*co*-norbornene) membrane as a separator in lithium-ion batteries. Macromolecular Rapid Communications, **34**, 581–587 (2013).
DOI: 10.1002/marc.201200754

[32] Kovačič S., Preishuber-Pflügl F., Slugovc C.: Macroporous polyolefin membranes from dicyclopentadiene high internal phase emulsions: Preparation and morphology tuning. Macromolecular Materials and Engineering, **299**, 843–850 (2014).
DOI: 10.1002/mame.201300400

[33] Krajnc P., Leber N., Štefanec D., Kontrec S., Podgornik A.: Preparation and characterisation of poly (high internal phase emulsion) methacrylate monoliths and their application as separation media. Journal of Chromatography A, **1065**, 69–73 (2005).
DOI: 10.1016/j.chroma.2004.10.051

[34] Moine L., Deleuze H., Maillard B.: Preparation of high loading polyHIPE monoliths as scavengers for organic chemistry. Tetrahedron Letters, **44**, 7813–7816 (2003).
DOI: 10.1016/j.tetlet.2003.08.051

[35] Christenson E. M., Soofi W., Holm J. L., Cameron N. R., Mikos A. G.: Biodegradable fumarate-based polyHIPES as tissue engineering scaffolds. Biomacromolecules, **8**, 3806–3814 (2007).
DOI: 10.1021/bm7007235

[36] Krajnc P., Leber N., Brown J. F., Cameron N. R.: Hydroxy-derivatised emulsion templated porous polymers (polyHIPEs): Versatile supports for solid and solution phase organic synthesis. Reactive and Functional Polymers, **66**, 81–91 (2006).
DOI: 10.1016/j.reactfunctpolym.2005.07.023

[37] Mert E. H., Kaya M. A., Yıldırım H.: Preparation and characterization of polyester–glycidyl methacrylate polyHIPE monoliths to use in heavy metal removal. Designed Monomers and Polymers, **15**, 113–126 (2012).
DOI: 10.1163/156855511X615001

[38] Mert E. H., Yıldırım H., Üzümcü A. T., Kavas H.: Synthesis and characterization of magnetic polyHIPEs with humic acid surface modified magnetic iron oxide nanoparticles. Reactive and Functional Polymers, **73**, 175–181 (2013).
DOI: 10.1016/j.reactfunctpolym.2012.09.005

[39] Tunç Y., Gölgelioğlu Ç., Hasirci N., Ulubayram K., Tuncel A.: Acrylic-based high internal phase emulsion polymeric monolith for capillary electrochromatography. Journal of Chromatography A, **1217**, 1654–1659 (2010).
DOI: 10.1016/j.chroma.2010.01.020

[40] Menner A., Salgueiro M., Shaffer M. S. P., Bismarck A.: Nanocomposite foams obtained by polymerization of high internal phase emulsions. Journal of Polymer Science Part A: Polymer Chemistry, **46**, 5708–5714 (2008).
DOI: 10.1002/pola.22878

[41] Kovačič S., Matsko N. B., Jerabek K., Krajnc P., Slugovc C.: On the mechanical properties of HIPE templated macroporous poly(dicyclopentadiene) prepared with low surfactant amounts. Journal of Materials Chemistry A, **1**, 487–490 (2013).
DOI: 10.1039/C2TA00546H

[42] Kovačič S.: Ring opening metathesis polymerisation (ROMP) as a tool for polyHIPES with extraordinary mechanical properties. Acta Chimica Slovenica, **60**, 448–454 (2013).

[43] Wu R., Menner A., Bismarck A.: Tough interconnected polymerized medium and high internal phase emulsions reinforced by silica particles. Journal of Polymer Science Part A: Polymer Chemistry, **48**, 1979–1989 (2010).
DOI: 10.1002/pola.23965

[44] Ikem V. O., Menner A., Bismarck A.: High-porosity macroporous polymers synthesized from titania-particle-stabilized medium and high internal phase emulsions. Langmuir, **26**, 8836–8841 (2010).
DOI: 10.1021/la9046066

[45] Barbetta A., Cameron N. R.: Morphology and surface area of emulsion-derived (polyHIPE) solid foams prepared with oil-phase soluble porogenic solvents: Span 80 as surfactant. Macromolecules, **37**, 3188–3201 (2004).
DOI: 10.1021/ma0359436

[46] Carvalho Jr. V. P., Ferraz C. P., Lima-Neto B. S.: Tailored norbornene-based copolymer with systematic variation of norbornadiene as a crosslinker obtained *via* ROMP with alternative amine Ru catalysts. European Polymer Journal, **48**, 341–349 (2012).
DOI: 10.1016/j.eurpolymj.2011.11.011

[47] Morbelli L., Eder E., Preishuber-Pflügl P., Stelzer F.: Copolymerizations between cyclic olefins and norbornene lactone. Journal of Molecular Catalysis A: Chemical, **160**, 45–51 (2000).
DOI: 10.1016/S1381-1169(00)00231-4

[48] Carvalho Jr. V. P., Ferraz C. P., Lima-Neto B. S.: Electronic synergism in $[RuCl_2(PPh_3)_2(amine)]$ complexes differing the reactivity for ROMP of norbornene and norbornadiene. Journal of Molecular Catalysis A: Chemical, **333**, 46–53 (2010).
DOI: 10.1016/j.molcata.2010.09.015

*eXPRESS Polymer Letters Vol.9, No.4 (2015) 354–361*
*Available online at www.expresspolymlett.com*
*DOI: 10.3144/expresspolymlett.2015.33*

# Effect of injection molded micro-structured polystyrene surfaces on proliferation of MC3T3-E1 cells

*G. Lucchetta[1]*, M. Sorgato[1], E. Zanchetta[1], G. Brusatin[1], E. Guidi[2], R. Di Liddo[2], M. T. Conconi[2]*

[1]University of Padua, Department of Industrial Engineering, Via Venezia, 1 - 35131 Padova, Italy
[2]University of Padua, Department of Pharmaceutical and Pharmacological Sciences, Via Marzolo, 5 - 35131 Padova, Italy

*Received 4 August 2014; accepted in revised form 12 October 2014*

**Abstract.** In this work, osteoinductive micro-pillared polystyrene surfaces were mass-produced for bone replacement applications, by means of the micro injection molding process. Firstly, the molding process parameters were optimized with a two-level, three-factor central composite face-centered plan to increase the quality of polystyrene micro pillars replication and to maximize the pillars height uniformity over the molded part. Secondly, osteoblastic MC3T3-E1 cells adhesion and proliferation on the replicated substrates were assessed as a function of micro topography parameters, such as pillars diameter, aspect ratio and spacing. Cell morphology and proliferation were evaluated through MTS test after 1, 3 and 7 days from seeding. The experimental results showed that cells adhesion and proliferation is more positively promoted on micro-pillared surfaces compared to flat surfaces, but no correlations were observed between cell proliferation and pillar diameter and spacing.

***Keywords:*** *processing technologies, micro injection molding, micro topography replication, cells growth*

## 1. Introduction

Osseointegration is the process in which an implanted material integrates with living bone, firmly anchoring the implant in place. It assures the clinical success of dental implants and creates anchors for prosthesis, such as prosthetic limbs. Osseointegration depends to a large extent on previous osteoinduction. This last process occurs in the initial part of the implant incorporation and healing response. Bone growth on an implant surface depends on the action of differentiated bone cells. These cells may originate either in pre-existing preosteoblasts/osteoblasts that are activated by trauma or in cells recruited from primitive mesenchymal cells by osteoinduction [1]. Work by several research groups has shown that biomaterials need to meet very specific requirements in terms of (a) chemical composition, (b) macrostructure and (c) microstructure in order to be osteoinductive [2]. Regarding this last requirement, several studies have shown that numerous cell types react to micro topography [3–5]. Changes in cell adhesion [6, 7], alignment [7, 8] and proliferation [9] have been reported in the literature. In particular, Kolind *et al*. [10] conducted a combinatorial screening experimental campaign to identify the effect of several distinct micro-pillared silicon wafers on fibroblast proliferation. They observed that larger (4–6 μm) inter-pillar gap sizes reduced fibroblast growth. Smaller (1–2 μm) inter-pillar spacing, on the contrary, caused the fibroblasts to proliferate comparable to cells on a non-structured surface.

Polymers have increasingly been used to look at how the elasticity of underlying substrates can be tailored to direct human mesenchymal stem cells (hMSC) differentiation into either neuronal, muscle or bone lineages [11]. Disordered arrays of nanoscale

*Corresponding author, e-mail: giovanni.lucchetta@unipd.it

pits on polymethyl methacrylate substrates have been found to induce hMSC differentiation into bone mineral in the absence of osteogenic biochemical cues [12]. hMSC culture on injection molded polycarbonate nano pits have been found to influence filopodia interaction, resulting in reduced spreading and focal adhesion [13].

Angelov *et al*. [14] have demonstrated that micro injection molding can be used for the mass fabrication of nano-pillared polystyrene (PS) surfaces for hMSC differentiation. However, the effect of the scale sizes (diameter and aspect ratio) as well as the spacing of the pillars on cell adhesion and proliferation needs to be further investigated, especially in relation to micro injection molding replication capabilities. In fact, the aspect ratio achievable in replicating micro features is one of the most important characteristics of any micro fabrication process and determines the manufacturing constraints of a given process-material combination. Molding micro features with high aspect ratios is still a challenge [15] because the high surface-to-volume ratio typical of micro cavities makes the melt solidify much faster than in the conventional process, thus leading to an incomplete replication. Concerning the achievable aspect ratios, there is a limitation that is a function of geometry of the micro features, their position on the part, the polymer type and the process parameters [16, 17]. Moreover, to achieve the required accuracy the process needs to be optimized, as the quality of micro molded parts can be largely modified by different selections of process parameters. Griffiths *et al*. [18] indicated that the selection of high process settings can significantly improve the replication quality. In particular, the mold temperature was identified as the most significant parameters, due to its influence on the viscosity of the polymer melt [19]. An increase in mold temperature, especially above the glass transition temperature of the material, could lessen the thermal gradient between the mold and the molten polymer [20, 21].

In this work, the micro injection molding process was employed and optimized to produce micro-pillared PS surfaces for bone replacement applications. Directly patternable hybrid materials were used for micro-structured mold inserts fabrication. Pillars diameter, aspect ratio and spacing were varied in order to evaluate the topography effect on osteoblastic MC3T3-E1 cells adhesion and proliferation.

## 2. Experimental

### 2.1. Materials

The material used for injection molding was a commercial polystyrene resin PS Crystal 1540, manufactured by TOTAL, with a MFI (200°C – 5kg) of 12 g/10 min and a $T_g$ of 100°C. This resin was chosen due to its high flowability, good biocompatibility, high optical clarity, high transparency and high impact strength. Furthermore, polystyrene was not treated for cell cultures to better discriminate the effects of micro-pillared on cell adhesion and growth. The molded products were cylindrical supports with a diameter of 5.9 mm and a thickness of 2 mm, with different micro-structured surface topographies.

### 2.2. Lithography and resist development

The tooling inserts were manufactured from rectangular pieces of steel 39NiCrMo3, according to the following operations: lapping, machining and photolithography. The initial rectangular pieces of steel were lapped to obtain a polish surface for the subsequent deposition of the masking film. The steel was initially sandpapered (grit: 180, 600, 1200) and then refined with abrasive particles (6, 3, 1 mm) to eventually obtain a surface with $R_a$ <0.050 μm. The lapped inserts were then machined to obtain the desired shape to mount it on the fixed plate of the mold. The inserts were eventually coated with a silica-zirconia directly patternable resist, which was synthesized starting with 3-(trimethoxysilyl)propyl methacrylate (TMSPM) and Zr-butoxide ($Zr(OBut)_4$) as sol-gel precursors. The system was obtained as follows: TMSPM was firstly hydrolyzed in acidic conditions for one hour at room temperature (TMSPM:$H_2O$:HCl=1:3:0.01 molar ratio). $Zr(OBut)_4$ and Metacrylic acid (MAA) were separately left stirring for five minutes, before being added to the hydrolyzed TMSPM solution (TMSPM:$Zr(OBut)_4$ = 1:0.5 molar ratio). The final sol was stirred for one hour. Tetrahydrofuran solvent was added to the sol to reach the desired concentration of 110 g/L $SiO_2$+$ZrO_2$. IRGACURE 369 photoinitiator was finally added 1% molar (with respect to TMSPM) to the sol before UV exposure. The sol was finally filtrated through a 0.2 μm filter in order to remove large particles and get a better film quality.

After spin coating at different speeds, according to the final target thickness, each insert was exposed

**Table 1.** Average values for holes depth and interspace

| Insert | Depth [µm] | Interspace [µm] | Aspect ratio |
|---|---|---|---|
| 2–8 | 0.990±0.147 | 7.999±0.048 | 0.495 |
| 3–9 | 1.525±0.033 | 9.012±0.058 | 0.508 |
| 4–10a | 0.990±0.041 | 10.020±0.065 | 0.248 |
| 4–10b | 1.789±0.094 | 10.063±0.091 | 0.477 |

to a 4 J/cm$^2$ ultraviolet dose through a mask, which contains the desired pattern. Three different patterns of equally spaced holes were realized over the whole circular area:

– Pattern 2–8: 2 µm diameter holes interspaced by 8 µm,
– Pattern 3–9: 3 µm diameter holes interspaced by 9 µm,
– Pattern 4–10: 4 µm diameter holes interspaced by 10 µm. Two inserts having different resist thickness (to vary the holes aspect ratio) were produced with this pattern.

Following UV exposure, the resist was developed for 15 s in a solution of ethanol:acetone 100:1 and dried by blowing air. This was followed by resist film hard-baking at 100°C for 1 hour.

Every insert was then characterized by means of an Atomic Force Microscope (DME, DS 95-200) having a nominal scanning range of 200×200 µm$^2$. All inserts were measured in three areas along the diameter of the molded part (close to gate, in the center and at the opposite side from the gate) for a total of 15 measurements per insert. Average values for the holes depth and interspace are reported in Table 1.

## 2.3. Polymer replication

Each micro-structured steel insert was housed in a custom-built steel mold. A state-of-the-art micro injection molding machine (Wittmann-Battenfeld, MicroPower 15) was used for the molding experiments. The machine is characterized by a maximum clamping force of 150 kN and a maximum injection speed of 750 mm/s. The plasticizing screw has a diameter of 14 mm and the injection plunger has a diameter of 5 mm.

A two-level, three-factor central composite face-centered plan was used to optimize the process using the insert 4–10b. The optimal process parameters determined for this insert have then been used to mold all of the other patterns. The factors investigated were injection speed ($V_{inj}$), mold temperature ($T_m$) and holding pressure ($P_{hold}$), as their influence on replication quality has been repeatedly reported in the literature [18, 22]. The choices of the upper and lower values for the factors derived from a literature review, recommendations of the material supplier and technological limits of the available experimental setup (Table 2). In particular, the lower and higher values for $V_{inj}$ were selected considering a robust molding window, which was defined in preliminary tests.

**Table 2.** Process parameter settings

| Level | $V_{inj}$ [mm/s] | $T_m$ [°C] | $P_{hold}$ [bar] |
|---|---|---|---|
| –1 | 250 | 50 | 100 |
| +1 | 500 | 90 | 200 |

The nozzle, front, middle, and rear temperature settings were: 240, 230, 220, and 200ºC respectively.

For each run, the parts produced in the first 20 cycles were discarded in order to stabilize the process, and then the following part was collected for metrological characterization. Each run of the designed experiments was replicated twice in a completely randomized order for a total of 30 produced samples, with the aim of minimizing the interference of external variability sources. The material was taken from a single batch.

The response variable for this analysis was chosen to be the replicated height of the pillars, measured by means of a state-of-the-art 3D optical profiler (Sensofar PLu neox) operating in confocal mode with 20× and 100× objectives. All replications of each treatment have been measured in three areas along the diameter of the molded part (Figure 1). The

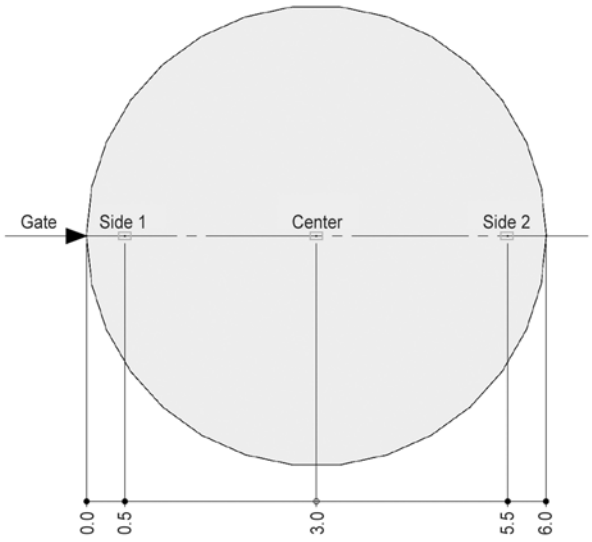


**Figure 1.** Measured areas for the characterization of the height of micro pillars. All quotes in mm.

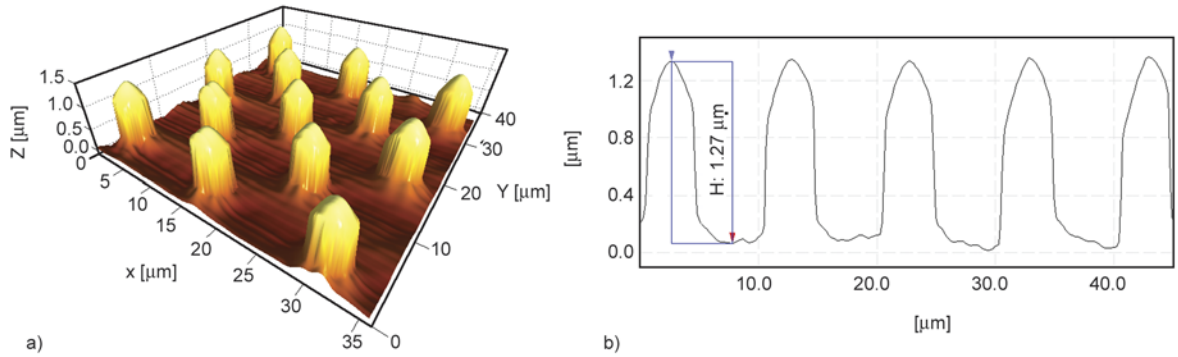


**Figure 2.** (a) Topography of a 4–10b insert replication in the Side 2 area; (b) height profile of the 5 measured micro pillars of a 4–10b insert in the Side 2 area

scans have an area of 127.32×95.45 mm$^2$. The positions of the measured areas are the same used for the inserts measurements.

Figure 2 shows the topography of the surface of a molded part in the scanned area. In each scanned area the profiles of 5 micro pillars were taken into consideration, for a total of 15 micro pillars analyzed for each replication. The height of the pillars was measured with 1-cursor pair using the image processing software SPIP 6.2.6 (Image Metrology).

### 2.4. Cell cultures

The osteoblastic cell line MC3T3-E1 was purchased from DSMZ (Leibniz-Institut DSMZ-Deutsche Sammlung von Mikroorganismen und Zellkulturen GmbH) and cultured with α-minimal essential medium (α-MEM, Life Technologies, Baltimore, MD, cod. 22561-021) containing 10% fetal bovine serum (FBS, Sigma, ST. Louis, MO, cod. F9665), and 1% penicilline/streptomycine (Sigma, cod. P0781). Cells were grown at 37°C in a humid atmosphere with 5% $CO_2$. Medium was refreshed three times a week. Cells ($1.5 \cdot 10^4$ cells/cm$^2$) were seeded on pillar-structured polystyrene arrays previously put onto wells of 96-well plates. Cultures grown on non-modified polystyrene arrays were used as control. After various time points from seeding, cell morphology and proliferation were evaluated.

At 24 h from seeding, cultures were fixed in 3.7% formaldehyde for 20 min at room temperature and then dehydrated with a graded ethanol series. After gold sputtering, samples were observed by a Scanning Electron Microscope (JEOL JSM-6490, Peabody, MA).

### 2.5. MTS assay

To test cell viability, the 3-(4,5-dimethylthiazol-2-yl)-5-(3-carboxymethoxyphenyl)-2-(4 sulfophenyl)-2H-tetrazolium) (MTS) test (CellTiter 96® AQueous One Solution Cell Proliferation Assay; Promega, Austria, cod. G3580) was used, according to the manufacturer's instruction. Briefly, at 1, 3, and 7 days from seeding, 200 uL of cell media, containing 10% MTS, were added into each well and cells were incubated at 37°C for 4 h. Optical density of purple formazan produced in living cells was measured at 490 nm, using a Microplate autoreader EL 311 (BIOTEK instruments Inc., Winooski, Vermont, USA). Results were expressed as number of cells. The linearity of absorbance of formazan over a range of $2.5 \cdot 10^3$–$20 \cdot 10^3$ cells was established by determining the linear coefficient (0.980).

Triplicate experiments were performed. The results were expressed as the arithmetic mean ± standard deviation. Their statistical comparison was performed by analysis of variance, followed by Student's *t*-test.

## 3. Results and discussion

### 3.1. Micro pillars replication

The primary goal of the performed experimental plan was to identify the factors that influence the replicated height of micro pillars. The ANOVA results for the designed plan indicate that all the factors and their interactions are significant, especially the mold temperature and the holding pressure (Table 3). The lack of fit test confirmed that the regression fitted the second-order model.

**Table 3.** Estimated regression coefficients for pillars height

| Term | Coef | SE Coef | T | P |
|---|---|---|---|---|
| Constant | 0.319720 | 0.009886 | 32.341 | 0.000 |
| $V_{inj}$ | 0.026222 | 0.005816 | 4.508 | 0.000 |
| $P_{hold}$ | 0.094042 | 0.005816 | 16.168 | 0.000 |
| $T_m$ | 0.238988 | 0.005816 | 41.089 | 0.000 |
| $V_{inj}$·$V_{inj}$ | 0.007625 | 0.011470 | 0.665 | 0.514 |
| $P_{hold}$·$P_{hold}$ | 0.023425 | 0.011470 | 2.042 | 0.055 |
| $T_m$·$T_m$ | 0.176858 | 0.011470 | 15.419 | 0.000 |
| $V_{inj}$·$P_{hold}$ | 0.002723 | 0.006503 | 0.419 | 0.680 |
| $V_{inj}$·$T_m$ | 0.010577 | 0.006503 | 1.627 | 0.119 |
| $P_{hold}$·Tm | 0.078952 | 0.006503 | 12.141 | 0.000 |

**Table 4.** Replication of the micro holes for the insert 4–10b

| Term | Holes depth [µm] | Pillars height [µm] | Difference |
|---|---|---|---|
| Side 1 | 1.789±0.094 | 0.707±0.065 | 60% |
| Center | 1.789±0.094 | 1.438±0.037 | 20% |
| Side 2 | 1.789±0.094 | 1.634±0.030 | 9% |

The maximum replication is achievable for the high values of the factors. As the high value of the mold temperature was already set at the technological limit of the available experimental setup, only the other process parameters were increased up to the maximum values of $P_{hold}$ = 400 bar and $V_{inj}$ = 700 mm/s. With this optimal combination of process parameters the replication results reported in Table 4 were obtained.

The inadequate replication of the micro holes located close to gate is due to the hesitation of the polymer in that zone. This hypothesis was confirmed by the results of further experiments carried out varying only $V_{inj}$ on three levels: 200, 500 and 700 mm/s. The effect of injection speed on the standard deviation of micro pillars height, plotted in Figure 3, clearly shows that for higher values of $V_{inj}$, the reduced hesitation time contributes to make the pillars height distribution more uniform over the molded part.

The quality of the replication was also assessed by observing both the mold inserts (Figure 4) and the

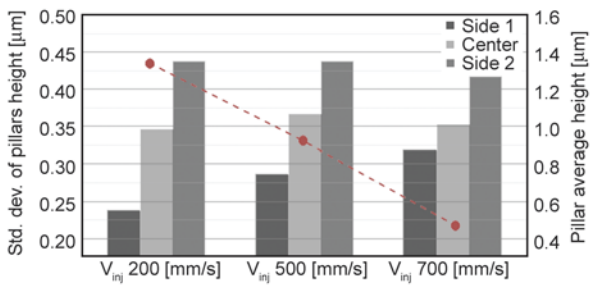


**Figure 3.** Influence of the injection speed on the standard deviation of micro pillars height along the diameter of the molded part ($P_{hold}$ = 200 bar, $T_m$ = 90°C)

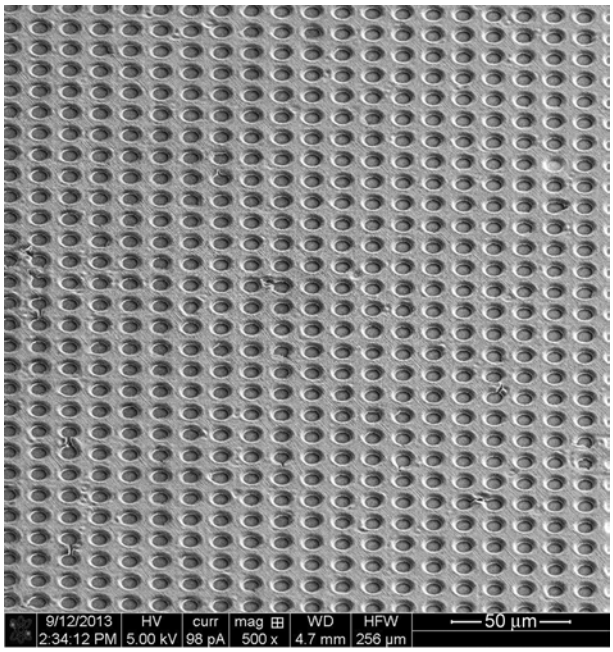


**Figure 4.** SEM micrographs of the micro holes in the pattern 4–10b insert

molded supports (Figure 5) by a Scanning Electron Microscope (FEI QUANTA 450).

Eventually, the optimal process parameters, determined by the experiments conducted using the insert 4–10b, were employed to produce supports with the inserts 2–8, 3–9 and 4–10a. The insert 4–10a instead of the 4–10b was used in order to maximize the aspect ratio variation and therefore to analyze the cell growth dependence on pillars aspect ratio. The overall replication results are reported in Table 5.

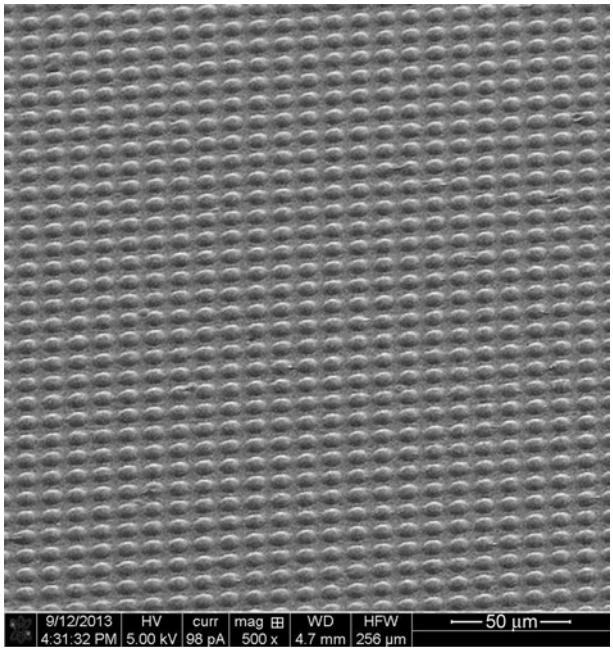


**Figure 5.** SEM micrographs of the micro pillars for the insert 4–10b

**Table 5.** Replication of the micro holes

| Pattern | 2–8 | 3–9 | 4–10a |
|---|---|---|---|
| Holes depth, HD [μm] | 0.990 | 1.525 | 0.990 |
| Pillars height, PH [μm] | 0.792 | 1.252 | 0.852 |
| Replication degree, PH/HD | 80% | 82% | 86% |
| Pillars aspect ratio | 0.396 | 0.417 | 0.213 |
| Interspace [μm] | 7.999 | 9.012 | 10.020 |

### 3.2. Cells growth

Our preliminary data reveal that the cells adhered and proliferated onto the micro-structured surface. Although cells adhered on all topographies at 1d, differences in cell morphology were noted (Figure 6). Indeed, the most of cells on modified inserts appeared flattened with several protrusions and less elongated that those observed on the smooth surfaces. Thus, as already observed by Justesen *et al*. [23] and by Hamilton *et al*. [24], surface topography influences cell morphology and this, in turn, can modulate cell differentiation. However, the geometry of our micropillars had no effect on cell orientation and alignment, because cells cultured on modified surfaces were randomly oriented. To evaluate the effect of substrate topography on cell proliferation, cell number was determined at 1, 3 and 7 d postseeding (Figure 7). On all cultural conditions no increases in cell number were detected between 1 and 3 d. Since the inserts were composed of polystyrene not treated for cell cultures, this result was expected. Furthermore, at 1 and 3 d no differences in cell number were detected among cultures grown on pillar-structured surfaces and the control ones. On the contrary, at 7 d the cell numbers on all modified surfaces were significantly higher than that determined on control

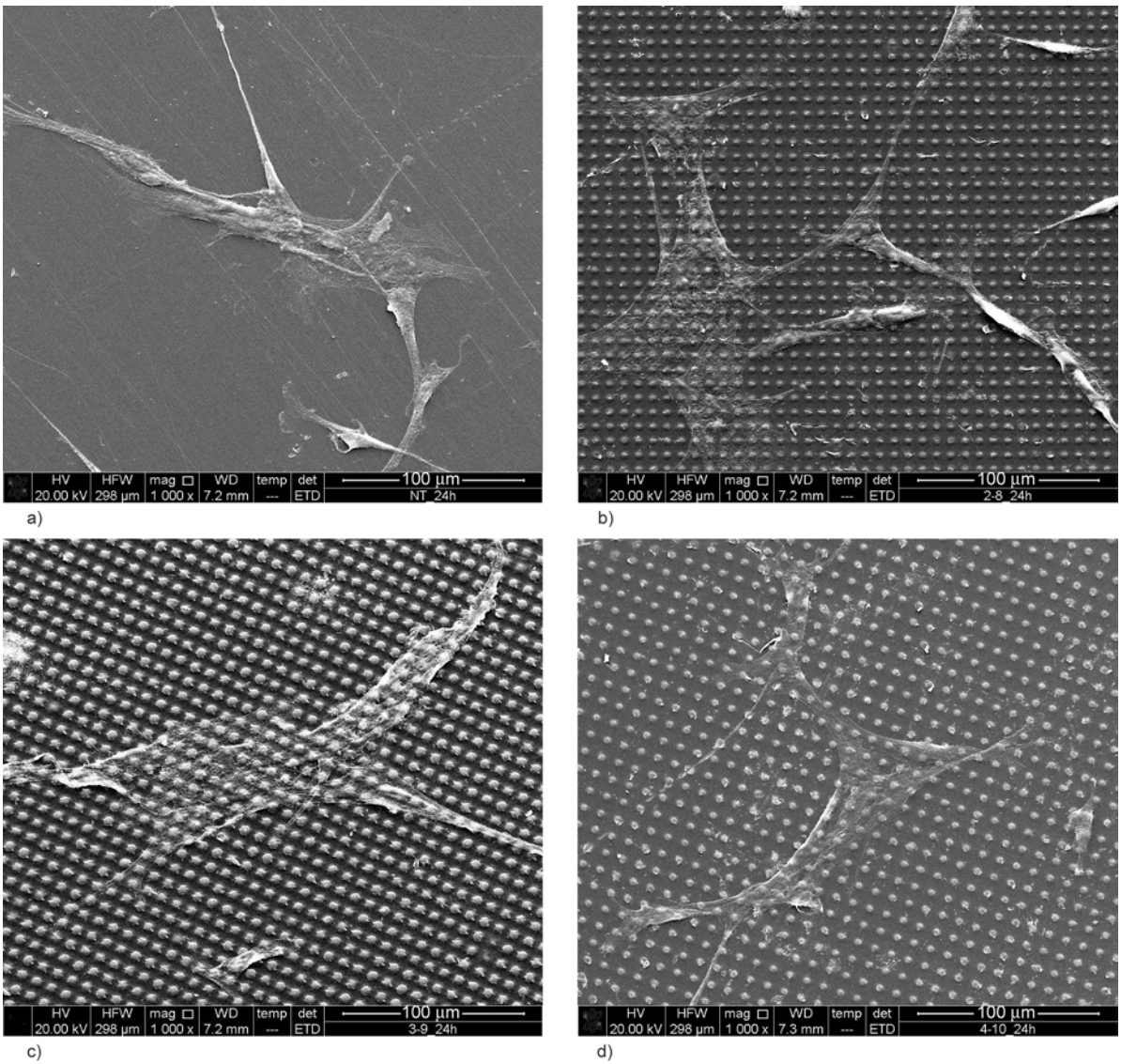


**Figure 6.** SEM micrographs of cultures grown on smooth (a), 2–8 (b), 3–9 (c), and 4–10 (d) inserts at 1 d from seeding

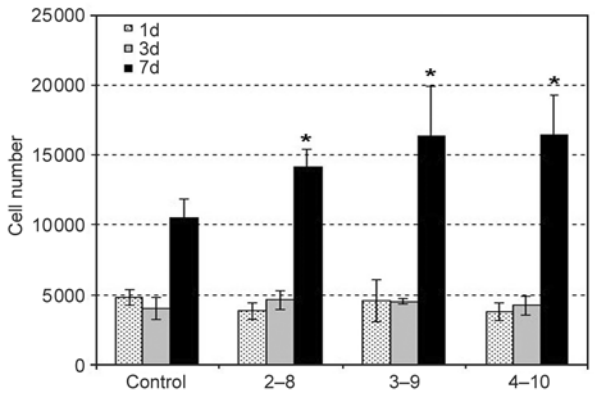


**Figure 7.** MTS assay at 1, 3, and 7 d after seeding. Results, expressed as cell number, are means ± SD of three independent experiments. * = $p$<0.05 vs control cultures, Student's $t$-test

cultures. However, no statistical differences in cell growth were noted among the pillar-structured surfaces.

## 4. Conclusions

The micro injection molding process of micro-pillared polystyrene surfaces, performed on directly patternable silica-zirconia hybrid micro-structured mold inserts, was optimized to increase the degree of micro structures replication. The experimental results obtained from micro-pillared surfaces show that cells adhesion and proliferation is more positively promoted on micro-pillared surfaces compared to flat surfaces. Although mouse osteoblastic MC3T3-E1 cells well adhered on micro-pillared PS surface, indicating a positive cell-substrate interaction, no correlations were between cell proliferation and pillar diameter and spacing. To obtain more concrete results, future work would focus on varying the scale sizes, realizing nano pillars, as well as the array pattern. Meaningful results will help to form the groundwork for studying the effects of controlling cells differentiation towards osteogenic lineage using nano-structured topography.

## Acknowledgements

The authors are grateful for the support of the Italian Ministry of Health (Grant: RF-2009-1528187).

## References

[1] Kraus K. H., Kirker-Head C.: Mesenchymal stem cells and bone regeneration. Veterinary Surgery, **35**, 232–242 (2006). DOI: 10.1111/j.1532-950X.2006.00142.x

[2] Habibovic P., de Groot K.: Osteoinductive biomaterials – Properties and relevance in bone repair. Journal of Tissue Engineering and Regenerative Medicine, **1**, 25–32 (2007). DOI: 10.1002/term.5

[3] Hasirci V., Kenar H.: Novel surface patterning approaches for tissue engineering and their effect on cell behavior. Nanomedicine, **1**, 73–90 (2006). DOI: 10.2217/17435889.1.1.73

[4] Flemming R. G., Murphy C. J., Abrams G. A., Goodman S. L., Nealey P. F.: Effects of synthetic micro- and nano-structured surfaces on cell behavior. Biomaterials, **20**, 573–588 (1999). DOI: 10.1016/S0142-9612(98)00209-9

[5] Curtis A. S. G., Dalby M., Gadegaard N.: Cell signaling arising from nanotopography: Implications for nanomedical devices. Nanomedicine, **1**, 67–72 (2006). DOI: 10.2217/17435889.1.1.67

[6] Matsuzaka K., Walboomers X. F., Yoshinari M., Inoue T., Jansen J. A.: The attachment and growth behavior of osteoblast-like cells on microtextured surfaces. Biomaterials, **24**, 2711–2719 (2003). DOI: 10.1016/S0142-9612(03)00085-1

[7] Recknor J. B., Recknor J. C., Sakaguchi D. S., Mallapragada S. K.: Oriented astroglial cell growth on micropatterned polystyrene substrates. Biomaterials, **25**, 2753–2767 (2004). DOI: 10.1016/j.biomaterials.2003.11.045

[8] Clark P., Connolly P., Curtis A. S., Dow J. A., Wilkinson D. W.: Topographical control of cell behaviour: II. Multiple grooved substrata. Development, **108**, 635–644 (1990).

[9] Keselowsky B. G., Wang L., Schwartz Z., Garcia A. J., Boyan B. D.: Integrin $\alpha_5$ controls osteoblastic proliferation and differentiation responses to titanium substrates presenting different roughness characteristics in a roughness independent manner. Journal of Biomedical Materials Research Part A, **80**, 700–710 (2007). DOI: 10.1002/jbm.a.30898

[10] Kolind K., Dolatshahi-Pirouz A., Lovmand J., Pedersen F. S., Foss M., Besenbacher F.: A combinatorial screening of human fibroblast responses on micro-structured surfaces. Biomaterials, **31**, 9182–9191 (2010). DOI: 10.1016/j.biomaterials.2010.08.048

[11] Engler A. J., Sen S., Sweeney H. L., Discher D. E.: Matrix elasticity directs stem cell lineage specification. Cell, **126**, 677–689 (2006). DOI: 10.1016/j.cell.2006.06.044

[12] Dalby M. J., Gadegaard N., Tare R., Andar A., Riehle M. O., Herzyk P., Wilkinson C. D. W., Oreffo R. O. C.: The control of human mesenchymal cell differentiation using nanoscale symmetry and disorder. Nature Materials, **6**, 997–1003 (2007).
DOI: 10.1038/nmat2013

[13] Hart A., Gadegaard N., Wilkinson C. D. W., Oreffo R. O. C., Dalby M. J.: Osteoprogenitor response to low-adhesion nanotopographies originally fabricated by electron beam lithography. Journal of Materials Science: Materials in Medicine, **18**, 1211–1218 (2007).
DOI: 10.1007/s10856-007-0157-7

[14] Angelov A., Coulter J., Jaafar I., Gomatam R., Kim Y., Rajagopalan P.: Realization of polymer-based nanostructured surfaces for biomedical applications via nanoscale injection molding. in 'SPE Annual Technical Conference and Exhibition. Denver, USA' 2489–2493 (2008).

[15] Yao D., Kim B.: Scaling issues in miniaturization of injection molded parts. Journal of Manufacturing Science and Engineering, **126**, 733–739 (2004).
DOI: 10.1115/1.1813479

[16] Heckele M., Schomburg W. K.: Review on micro molding of thermoplastic polymers. Journal of Micromechanics and Microengineering, **14**, R1–R14 (2004).
DOI: 10.1088/0960-1317/14/3/R01

[17] Lucchetta G., Sorgato M., Carmignato S., Savio E.: Investigating the technological limits of micro-injection molding in replicating high aspect ratio micro-structured surfaces. CIRP Annals – Manufacturing Technology, **63**, 521–524 (2014).
DOI: 10.1016/j.cirp.2014.03.049

[18] Griffiths C. A., Dimov S. S., Scholz S., Tosello G.: Cavity air flow behavior during filling in microinjection molding. Journal of Manufacturing Science and Engineering, **133**, 011006/1–011006/10 (2011).
DOI: 10.1115/1.4003339

[19] Mönkkönen K., Pakkanen T. T., Hietala J., Pääkkönen E. J., Pääkkönen P., Jääskeläinen T., Kaikuranta T.: Replication of sub-micron features using amorphous thermoplastics. Polymer Engineering and Science, **42**, 1600–1608 (2002).
DOI: 10.1002/pen.11055

[20] Lin H-Y., Chang C-H., Young W-B.: Experimental and analytical study on filling of nano structures in micro injection molding. International Communications in Heat and Mass Transfer, **37**, 1477–1486 (2010).
DOI: 10.1016/j.icheatmasstransfer.2010.08.017

[21] Lucchetta G., Fiorotto M., Bariani P. F.: Influence of rapid mold temperature variation on surface topography replication and appearance of injection-molded parts. CIRP Annals – Manufacturing Technology, **61**, 539–542 (2012).
DOI: 10.1016/j.cirp.2012.03.091

[22] Tosello G., Gava A., Hansen H. N., Lucchetta G.: Influence of process parameters on the weld lines of a micro injection molded component. in 'Conference Proceedings of Annual Technical Conference – ANTEC, Cincinnati, USA' Vol 4, 2002–2006 (2007).

[23] Justesen J., Lorentzen M., Andersen L. K., Hansen O., Chevallier J., Modin C., Füchtbauer A., Foss M., Besenbacher F., Duch M., Pedersen F. S.: Spatial and temporal changes in the morphology of preosteoblastic cells seeded on microstructured tantalum surfaces. Journal of Biomedical Materials Research Part A, **89**, 885–894 (2009).
DOI: 10.1002/jbm.a.32032

[24] Hamilton D. W., Wong K. S., Brunette D. M.: Microfabricated discontinuous-edge surface topographies influence osteoblast adhesion, migration, cytoskeletal organization, and proliferation and enhance matrix and mineral deposition *in vitro*. Calcified Tissue International, **78**, 314–325 (2006).
DOI: 10.1007/s00223-005-0238-x

*eXPRESS Polymer Letters Vol.9, No.4 (2015) 362–371*
*Available online at www.expresspolymlett.com*
*DOI: 10.3144/expresspolymlett.2015.34*

# Investigation of fatigue and mechanical properties of the pipe grade poly(vinyl chloride) using recycled scraps

*J-M. Lee*[1], *J-S. Moon*[2], *H. Lee*[1], *B-H. Choi*[3*]

[1]Tech Center, LG Chem Co. Ltd., Republic of Korea
[2]VC R&D Laboratory, LG Electronics Co. Ltd., Republic of Korea
[3]School of Mechanical Engineering, Korea University, Republic of Korea

*Received 4 August 2014; accepted in revised form 19 October 2014*

**Abstract.** In this paper, the effect of using pre-consumer PVC scraps on static and long-term mechanical properties is studied. The degradation characteristics of mixing virgin PVC with crushed pre-consumer and PVC pipe scraps are analyzed using various tools including Gel Permeation Chromatography (GPC), Thermogravimetric Analysis (TGA), X-ray fluorescence (XRF) and Fourier Transform Infrared (FTIR) spectroscopy. The variation of static mechanical properties as a function of adding pre-consumer PVC pipe scraps is investigated using the degradation analyses of recycled PVC scraps. In addition, fatigue tests are executed to evaluate the long-term durability of blending virgin PVC and recycled PVC scraps, and the fracture surface is investigated in detail to reveal the variation of the fracture mechanisms.

***Keywords:*** *recycling, poly(vinyl chloride), fatigue, fractography, thermal degradation*

## 1. Introduction

Poly(vinyl chloride) (PVC) is commonly used in many commercial products such as pipes, window profiles, rigid sheets, cables, etc. because of its unique properties. Especially, PVC is commonly used to make pipes and fittings; up to 40% of polymer pipe and fitting market is occupied by PVC [1]. PVC pipes are widely used for various industrial and consumer piping systems such as pressurized piping systems, portable water transportation systems, and non-pressurized sewer and drainage piping systems.

One of the technical issues with the use of recycled PVC scraps for producing low cost non-pressurized sewer and drainage piping systems is that recycled PVC scraps impact the quality control of such piping systems because the control of recycled PVC scraps is not managed well. The separation of the scrap from the contaminants can be another issue [2]. While the regulation on the use of recycled PVC scraps is very limited, the details of the variation of long-term as well as static mechanical properties of PVC using recycled PVC scraps have scarcely been considered. Since PVC piping systems are recognized as low-cost applications, the variation of some key properties such as mechanical properties, lifetime, etc. has not been properly evaluated in the field. Moreover, since the piping system is a rather essential infrastructure and is intended to last for several decades, the long-term durability under fatigue and creep loading conditions, in addition to the variation of static mechanical properties, are very important. Especially, fatigue tests are usually considered as one of efficient accelerated test, so there have been some efforts of the application of fatigue characteristics on PVC pipe designs [3, 4].

*Corresponding author, e-mail: bhchoi@korea.ac.kr

Previous researches on the use of recycled PVC mainly focused on the blending of virgin and recycled PVC [5–10], the blending of recycled PVC with different polymers [11–14], and the effect of aging due to the repeated use of PVC [15]. However, most researches focused on the variation of static mechanical properties, and investigations on long-term durability are very scarce. Ma and La Mantia [8] studied the variation of thermal stability and mechanical properties when using post-consumer PVC beverage bottles and recycled pipe-grade PVC. Arnold and coworkers [9, 10] compared the mechanical properties of virgin and post-consumer recycled PVC. Ajji [13] investigated the variation of mechanical properties of virgin and recycled PVC and polyethylene (PE) based on additives and peroxides. Yarahmadi *et al*. [15] studied the variation of physical properties when repeatedly using extruded PVC, and observed the long-term degradation behavior using accelerated thermal ageing tests.

In this paper, the effect of using pre-consumer PVC scraps (which can be collected during the pipe manufacturing process then mixed with virgin pipe grade PVC) on static and long-term mechanical properties is studied. The degradation characteristics by mixing virgin PVC with crushed pre-consumer and PVC pipe scraps are analyzed using various tools including GPC, TGA, XRF, and FTIR spectroscopy. The variation of static mechanical properties as a function of adding pre-consumer PVC pipe scraps is investigated and related to the degradation analyses of recycled PVC scraps. In addition, fatigue tests are executed to evaluate the long-term durability of the blend with virgin PVC and recycled PVC scraps, and the fracture surface is investigated in detail to reveal the variation of fracture mechanisms.

## 2. Materials and experiments

### 2.1. Virgin PVC and recycled PVC scraps

Virgin PVC used in this study is commercially available pipe-grade PVC for sewage and drainage piping systems, and is a homopolymer with the degree of polymerization (DP) of 1000 and K-value of 66 from LG Chem (Yeosu, Korea). Recycled PVC scraps are collected from various pipe extrusion processes, and are crushed as flakes and used without any additional additives.

Five samples were prepared by blending virgin PVC with recycled PVC scraps of various weights; the composition of virgin PVC to recycled PVC scraps is shown with sample codes in Table 1. V and R in the sample codes represent the virgin PVC and the recycled PVC scraps, respectively, and the number following V and R represents the weight fraction of each polymer.

### 2.2. Specimens and experiments

Sample strips of 32 mm width and 3.10~3.24 mm thickness were extruded using a conical type extruder (KMD 2-25KK) from Krauss Maffei (Munich, Germany), and test specimens were fabricated by mill machining the strips. While extruding the strips, the adapter and die temperatures were 185 and 190°C, respectively, and the barrel temperature was 180°C/182°C. The screw and transmitting speeds of the extruder were 15 and 10 rpm, respectively.

The degree of polymerization of scraps blended with virgin PVC (V100R0) and recycled PVC (V0R100) was confirmed by a custom-made GPC system from Waters GPC systems (Milford, U.S.A.). The contents of inorganic components and the ash amount in the strips were examined using XRF and TGA (Q5000) from TA Instruments (New Castle, U.S.A.). In addition, the chemical structures of the strips were confirmed using an FTIR spectrometer (Equinox 55) from Bruker (Billerica, U.S.A.). Samples for both of GPC and TGA were collected from the central region of flexural test specimens. Samples for GPC were dissolved by tetrahydrofuran (THF). TGA was repeated with two samples to confirm the reproducibility of test results.

The mechanical properties of the strips were tested using tensile and flexural tests based on ASTM D638 and D790, respectively, and the loading speed was 10 mm/min. The specimen geometry of tensile and flexural tests are shown in Figure 1. Izod impact tests were also executed based on ASTM D258.

Fatigue tests were executed using tensile test specimens (ASTM D638 Type I) as shown in Figure 1a at room temperature using the Instron 8872 servo-

**Table 1.** The composition of virgin PVC and recycled PVC scraps with sample codes (V: virgin PVC, R: recycled PVC)

| Sample code | V100R0 | V75R25 | V50R50 | V20R80 | V0R100 |
|---|---|---|---|---|---|
| Virgin PVC [wt%] | 100 | 75 | 50 | 20 | 0 |
| Recycled PVC [wt%] | 0 | 25 | 50 | 80 | 100 |

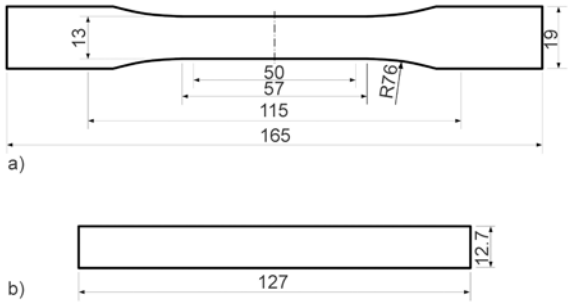


**Figure 1.** Specimen geometry, a) tensile and fatigue tests (ASTM D638 Type I), b) flexural tests (ASTM D790)

hydraulic testing system (Norwood, U.S.A.). Sinusoidal wave was used for the load controlled fatigue test; the stress ratio (R) and test frequency were 0.01 and 5 Hz, respectively. Five stress levels for fatigue tests were selected within 25%~65% of the tensile strength of each strip, and conventional *S–N* curves were plotted. It is commonly known that the variation of fatigue strength of PVC over 2 million cycles does not affect the fatigue limit [16], so, in this paper, fatigue tests were performed less than 3 million cycles.

Fractographic analyses were carried out to understand the fracture mechanisms of the failed specimens using an optical microscope AM-413ZT from AnMo Electronics Corporation and a scanning electron microscope (SEM) S-3500 from Hitachi.

## 3. Results and discussion

### 3.1. Characterization of materials degradation

Virgin PVC and recycled PVC show very similar molecular weight distributions using GPC as shown in Figure 2. In Figure 2, GPC results of three reference samples with various degree of polymerization (DP) are also plotted. The shoulder of virgin and recycled PVC in Figure 2 shows that the same processing aids are used for both PVCs. No significant difference in the GPC curves is observed between the two PVC types, though the molecular weight distribution of recycled PVC ($M_n$ = 73 322 and $M_w$ = 153 538) was slightly shifted to the left hand side comparing with that of virgin PVC ($M_n$ = 75 677 and $M_w$ = 159 780). It can show that recycled PVC is somewhat degraded.

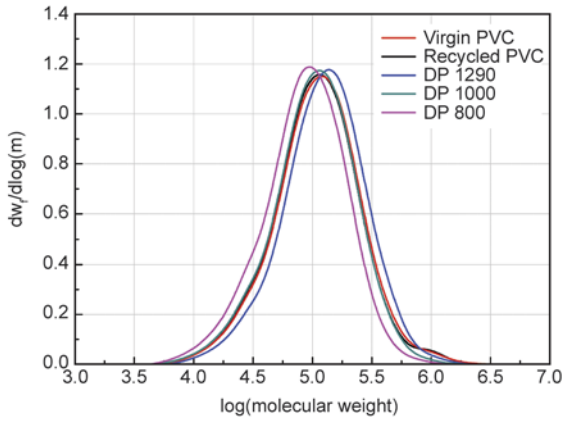


**Figure 2.** Molecular weight distribution of the virgin and recycled PVC with reference materials using GPC (DP: degree of polymerization)

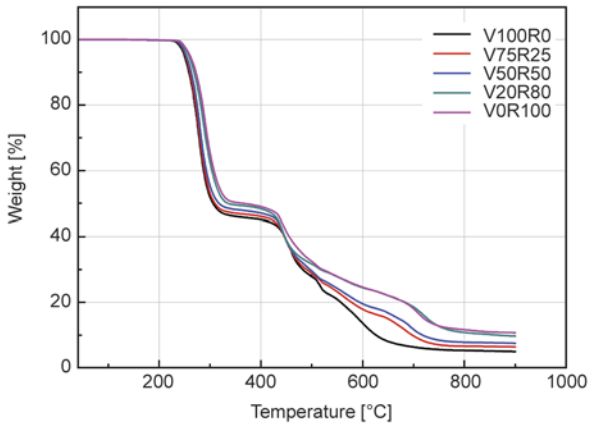


**Figure 3.** The characteristics of thermal decomposition and the volatile content are investigated by TGA

The characteristics of thermal decomposition and the volatile content are investigated by TGA, as shown in Figure 3. All samples have an initial weight loss at around 260°C, implying that most HCl components including dehydrochlorination are decomposed at this temperature [17]. As the contents of the recycled PVC increase, the second and the third decomposition temperatures slightly shifted to a higher temperature. In addition, the amount of non-volatile residues increases with the increasing content of recycled PVC, and the amount of residues of recycled PVC (10.76 wt%) is more than twice that of virgin PVC (4.97 wt%). Such a large amount of non-volatile residues in recycled PVC increases the inhomogeneity of the blend with recycled PVC. In Table 2, the composition of inorganic components

**Table 2.** Typical composition of virgin and recycled PVC [wt%]

| Composition | Pb | Ca | Sn | Zn | Ash |
|---|---|---|---|---|---|
| V100R0 | ND | 2.5 | ND | 0.1 | 4.97 |
| V75R25 | 0.3 | 3.2 | ND | 0.1 | 6.44 |
| V50R50 | 0.6 | 4.2 | ND | 0.1 | 7.55 |
| V20R80 | 1.0 | 5.5 | ND | 0.04 | 9.75 |
| V0R100 | 1.3 | 6.4 | ND | ND | 10.76 |

of virgin PVC and recycled PVC using XRF is shown. It is observed that, as the contents of recycled PVC increase, the amount of lead (Pb), which is the thermal stabilizer for recycling PVC, increases. In addition, the amount of ash and fillers such as $CaCO_3$ also increases by increasing the amount of recycled PVC.

The variation of chemical structures by adding recycled PVC is investigated using FTIR spectroscopy. It is observed that the peak around 900 $cm^{-1}$ increases as the recycled PVC increases, which may indicate the formation of cis-olefins or aromatic-olefins [18–20]. Two explanations for this are possible: (1) the ineffective or improper thermal stabilization of recycled PVC may lead the localized crosslinking of olefin structures after removing HCl and (2) the formation of polyene structures containing double-bonds before crosslinking by the reaction of sufficient thermal stabilizers. However, as shown in Figure 2, significant crosslinking is not clearly observed, so the latter might be a more reasonable explanation, especially if the proper amount of lead stabilizers is added to the recycled PVC.

### 3.2. Static mechanical properties

The tensile strength, elastic modulus, and strain at break of V100R0 were measured at 45 MPa, 2.29 GPa, and 120%, respectively, and the Izod impact strength was measured as 7.3 kJ/$m^2$. The variations of static mechanical properties of the strips are summarized in Table 3 and Figure 4.

**Table 3.** Experimental results of the mechanical properties

| Sample | Tensile | | | Flexural | | Izod impact |
|---|---|---|---|---|---|---|
| | Strength [MPa] | Modulus [MPa] | Elongation [%] | Strength [MPa] | Modulus [MPa] | Strength [kJ/$m^2$] |
| V100R0 | 44.7±1.26 | 2293±47 | 128±16 | 78.5±0.42 | 2307±50 | 7.3±0.21 |
| V75R25 | 43.6±0.95 | 2276±50 | 64±4 | 78.0±0.64 | 2458±52 | 6.4±0.66 |
| V50R50 | 40.8±0.66 | 2313±88 | 22±6 | 76.2±1.50 | 2477±24 | 5.5±0.46 |
| V20R80 | 41.8±0.61 | 2372±96 | 15±7 | 77.9±0.71 | 2654±50 | 5.0±0.59 |
| V0R100 | 42.5±0.69 | 2502±150 | 30±10 | 79.0±1.13 | 2736±55 | 5.1±0.25 |

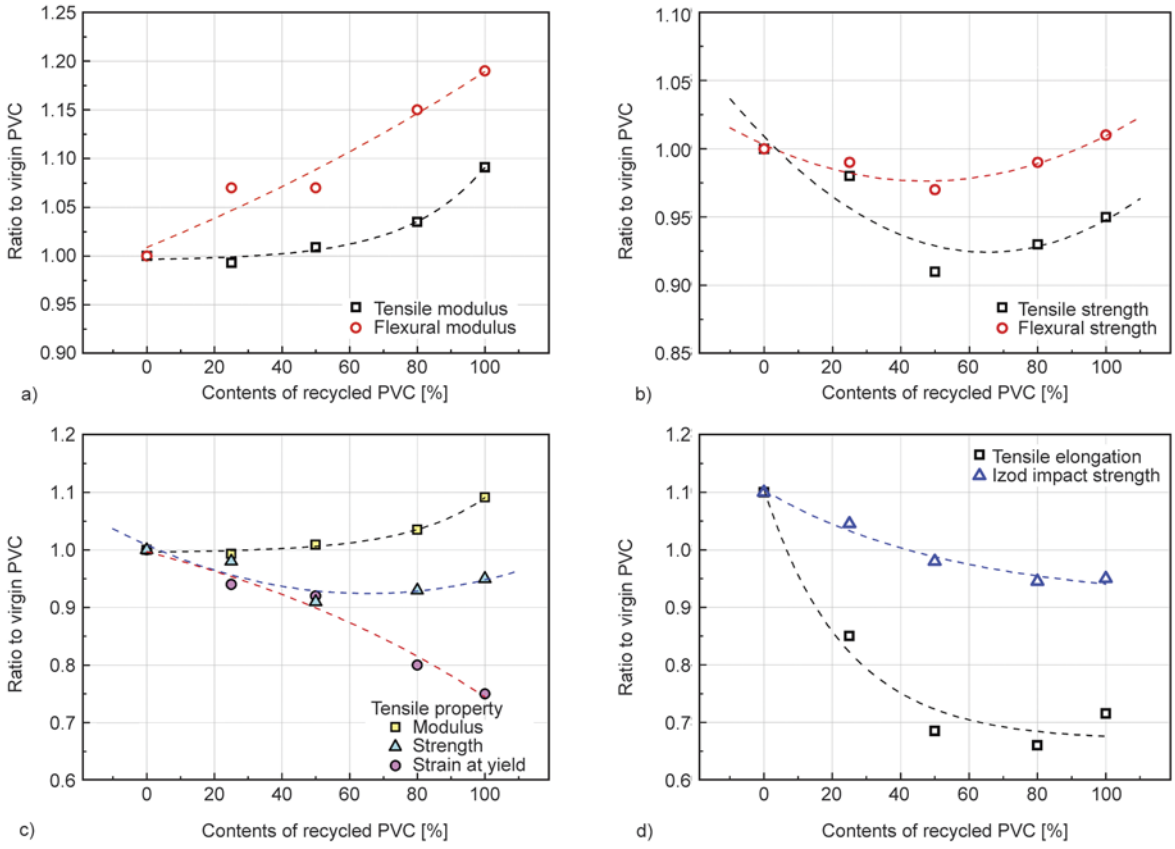


**Figure 4.** Variation of mechanical properties with different contents of recycled PVC; (a) modulus, (b) strength, (c) tensile properties, (d) tensile elongation and Izod impact strength

Tensile and flexural moduli increase as the content of recycled PVC scraps increases, as shown in Figure 4a, and both moduli of recycled PVC, i.e. V0R100, are recorded as higher than that of virgin PVC, i.e. V100R0, which may be caused by the embrittlement of recycled PVC due to degradation. Interestingly, both moduli increase rapidly after blending an amount of recycled PVC of 50% or greater. The relationship between contents of recycled PVC and tensile/flexural strengths is shown in Figure 4b. Unlike tensile and flexural moduli, tensile and flexural strengths decrease up to the V50R50 sample and thereafter increase by adding recycled PVC. The tensile and flexural strengths of recycled PVC are equal or slightly lower than those of virgin PVC. Such behavior might be explained by two opposite phenomena: (1) stiffening of the blend by adding recycled PVC and (2) inhomogeneity of the blend due to the formation of residues by adding uncontrolled recycled PVC (see Figure 3). The incompatibility of virgin PVC and recycled PVC could also be a possible root cause [5, 21]. The incompatibility and antagonistic effects can arise not only from blending polymers with different structures, but also form blending polymers with very similar structures. This can occur when blends are prepared from the sample polymer, i.e. virgin and recycled [21]. In the case of V50R50, as shown in Figure 4c, the stiffening effect is not significant, but the incompatibility of virgin and recycled PVC leads the low strength of the blend. It is also observed that recycled PVC has low strain at yield as well as low yield strength; this can be explained by the formation of residues, which are the source of the early failure. As shown in Figure 4d, both the tensile elongation and the Izod impact strength decrease rapidly as the contents of the recycled PVC increase. Under tensile loading conditions, virgin PVC shows ductile failure, but samples that contain more than 50% recycled PCV show quasi-brittle failure. The same transition of failure mechanism is observed for Izod impact strength. Therefore, it can be understood that the blends containing more than 50% recycled PVC may very likely exhibit brittle mechanical behavior.

As shown in Figure 5, fractographic analysis of the fracture surface of samples under tensile loading conditions is executed to understand the change of fracture mechanisms. The fracture surface of virgin PVC shows ductile failure; however, as the contents of recycled PVC increase, many residues are observed on the fracture surface. These residues are

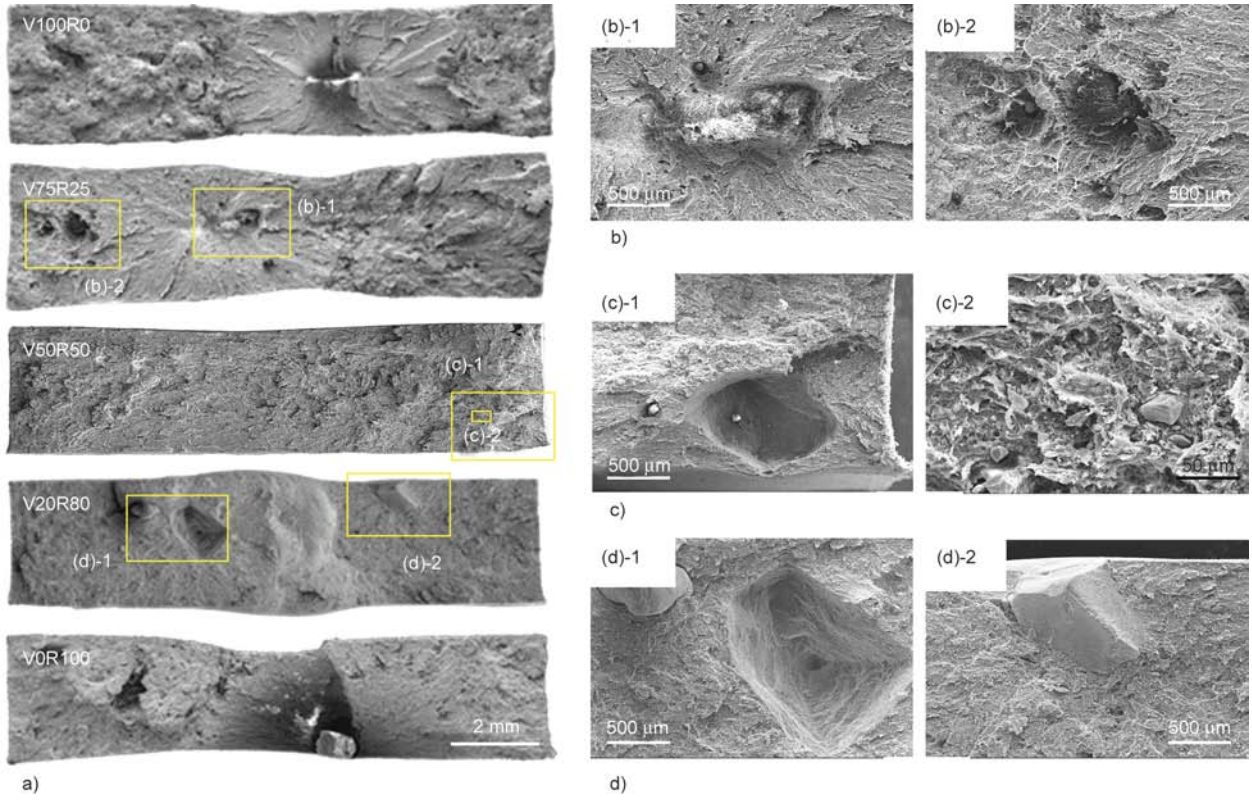


**Figure 5.** Fracture surface of samples under tensile loading condition; (a) whole surfaces of all samples, (b) V75R25, (c) V50R50, (d) V20R80

non-volatile, as analyzed by TGA, and they could be the source of the decreasing ductility of the blends with recycled PVC. Quasi-brittle behaviors observed from samples with 50% or more recycled PVC are mainly caused by local failures, i.e. multi-scale cracking, due to widely distributed residues as well as significant reduction of ductility of recycled PVC. The incompatibility of residues and inclusions with the matrix can be observed by the formation of craters on the fracture surface as shown in Figure 5. These craters could initiate local failures, and eventually affect the toughness of the blend. The elements of residues are characterized by energy-dispersive X-ray spectroscopy (EDS), and it is observed that all of residues contain $SiO_2$ and $CaCO_3$ as shown in Figure 6a. As shown in Figure 6b, the recycled PVC has a trace of $CaCO_3$ which is thermal stabilizer. However, virgin PVC does not show the trace of such thermal stabilizer as shown in Figure 6c. $SiO_2$ may not be expected from multiple extrusion processes, so it may enter the recycled PVC during handling them.

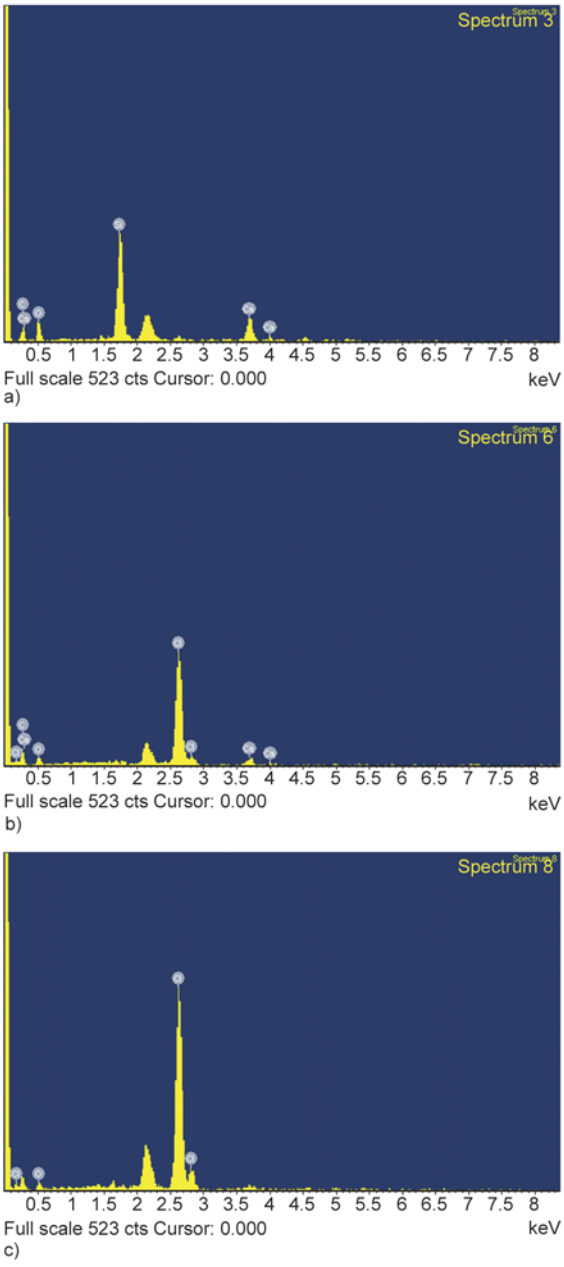


**Figure 6.** EDS spectrum of residue found from the fracture surface by comparing EDS spectra of V0R100 and V100R0 sample; (a) residue, (b) recycled PVC, (c) virgin PVC

### 3.3. Fatigue characteristics

Fatigue test results can be summarized using conventional *S–N* curves which can be expressed by a power law equation (Equation (1)):

$$S_{max} = S_f \cdot (N)^b \quad (1)$$

where $S_{max}$ is the maximum stress and $N$ is the number of cycles to failure. The fatigue fitting parameters in Equation (1) are the fatigue strength coefficient, $S_f$, and the fatigue strength exponent, $b$.

The fatigue test results for three samples, i.e. V100R0, V50R50, and V0R100, with actual test data are shown in Figure 7. Virgin PVC, V100R0, shows the best fatigue characteristics, while the worst fatigue characteristics are observed in the case of V50R50. Interestingly, the fatigue characteristics of V0R100 were recovered and were in between those of V100R0 and V50R50. It may also be related with complicated mechanisms such as the embrittlemet and inhomogeneity of recycled PVC, possible incompatibility of virgin and recycled PVC and so on.

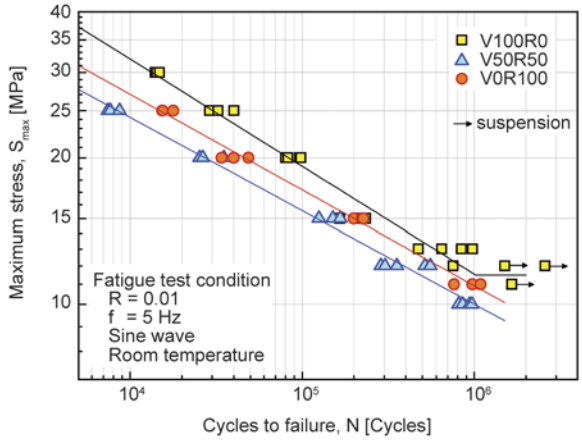


**Figure 7.** Fatigue tests results for selected samples (V100R0, V50R50 and V0R100) with actual test data

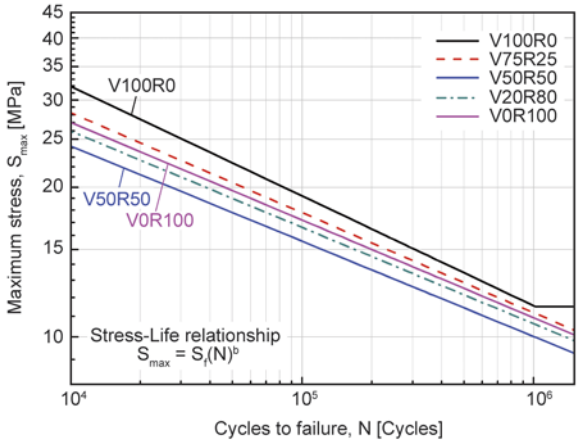


**Figure 8.** The schematics of *S–N* diagram for all samples are drawn, and measured fatigue fitting parameters are summarized in Table 4

Figure 8 shows the schematics of an *S–N* diagram for all test samples, and measured fatigue fitting parameters are summarized in Table 4. Both the fatigue strength coefficient and fatigue strength exponent decrease with up to 50% of recycled PVC content, and they increase when blending additional recycled PVC. The fatigue limit of V100R0 is measured as 11.5 MPa, but that of the blends is not easily defined due to the inhomogeneity of the blends, which causes possible long-life failures.

**Table 4.** Fatigue parameters of $S_{max}$–$N$ curves for various samples with different contents of recycled PVC (valid range: $1{\cdot}10^4 \le N \le 1{\cdot}10^6$, $S_f$: fatigue strength coefficient, $b$: fatigue strength exponent)

| Sample | V100R0 | V75R25 | V50R50 | V20R80 | V0R100 |
|---|---|---|---|---|---|
| $S_f$ | 244.56 | 180.70 | 141.96 | 154.79 | 165.47 |
| $b$ | –0.22096 | –0.20142 | –0.19194 | –0.19390 | –0.19672 |

The variation of the fatigue strength of blends as a function of the content of recycled PVC for three fatigue cycles to failure is shown in Figure 9a. In general, the fatigue strength decreases when adding recycled PVC up to 50%, but the fatigue strength increases again when adding additional recycled PVC. The maximum fatigue strength for all fatigue cycles to failure is observed for V100R0 and interestingly, the fatigue strength of V0R100 is better than some blend samples, e.g. V50R50 and V20R80. The variation of fatigue strength is significant at shorter fatigue cycles to failure, but it is less significant as the fatigue cycles to failure increase. However, unlike virgin PVC, blends with recycled PVC do not show a clear fatigue limit due to residues and inclusions; it can thus be expected that blends with recycled PVC may fail even at very-long fatigue cycles unless such residues and inclusions are well controlled. Similar fatigue characteristics can be observed in Figure 9b. Figure 9b shows a comparison of the fatigue cycles to failure for various stress levels ($S_{max}$ 12~25 MPa). It is observed that the fatigue lifetime to failure of V0R100 is about 49~74% of that of V100R0, and the fatigue lifetime to failure of V50R50 is only 28~47% of that of V100R0. Moreover, the initial drop of fatigue characteristics by adding recycled PVC is significant; it is thus observed that the fatigue lifetime to failure of V75R25 is already 61~84% of that of V100R0. Therefore, it can be thought that, even with a small amount of recycled PVC, the blend may affect the fatigue characteristics.

According to fatigue test results, it can be understood that several factors such as the incompatibil-

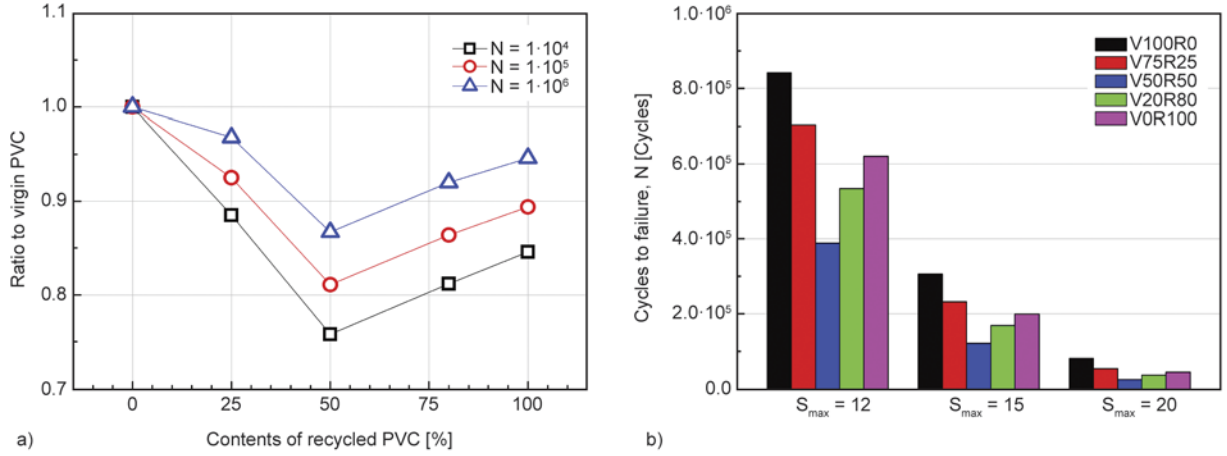


**Figure 9.** Variation of fatigue properties with different contents of recycled PVC; (a) fatigue strength at the each *N*, (b) *N* at the each fatigue strength

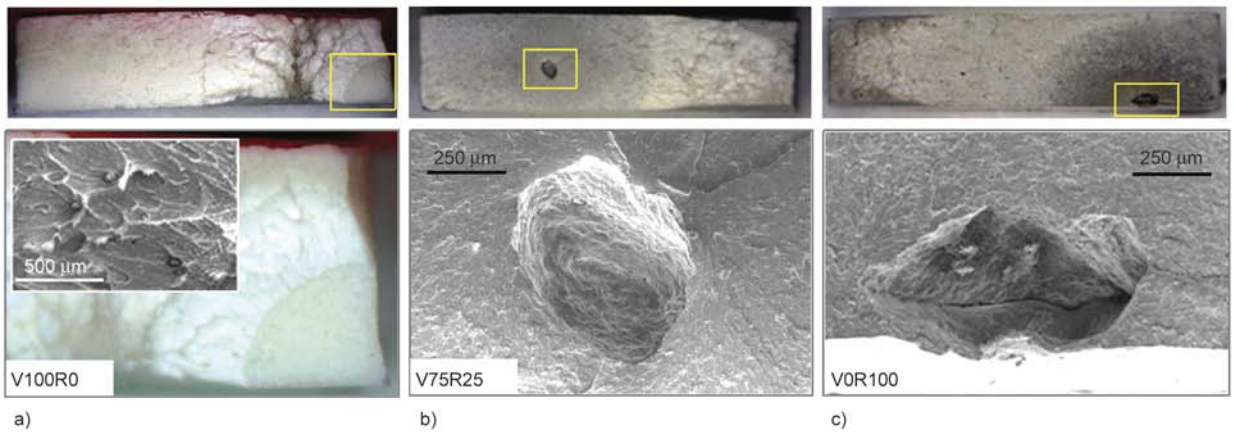


**Figure 10.** Optical and scanning electron microscopes of fatigue fractured surface; (a) V100R0, (b) V75R25, (c) V0R100

ity of virgin and recycled PVC, the formation of non-volatile residues, the stiffening effect of recycled PVC etc., together affect the fatigue characteristics. For example, V50R50 shows the worst fatigue characteristics among test samples due to the noticeable amount of residues with relatively low stiffening effect of recycled PVC. It is also interesting to note that the rank of the fatigue strength is similar to that of the tensile strength.

In Figure 10, the facture surfaces after fatigue tests are observed by optical and scanning electron microscopes. In the case of V100R0, for most specimens, a crack initiated from the edge of the specimen and grew into the specimen, which is a typical type of crack growth. Striations are not observed, but some traces of remnants of fibrillar deformation of the matrix material are observed. However, after the recycled PVC was added, macroscopic residues were observed at the crack initiation site (e.g. V75R25 and V0R100 shown in Figure 10). As the contents of recycled PVC increases, such macroscopic residues are more frequently observed. Approximately 60% of V75R25 and V50R50 specimens failed with such residues, and, in the cases of the V20R80 and V0R100 specimens, almost 90% of specimens failed with the residue. In addition, unlike V100R0, as the contents of recycled PVC increase, the fracture surface became brittle, so it is difficult to observe well-developed fibrillar deformation of the matrix material. Also, it is confirmed that all residues found at the fatigue crack initiation position have same elements discussed in Figure 6 by EDS analysis.

As described above, a blend of virgin PVC and recycled PVC may cause the loss of both static and long-term mechanical properties, although indication of chemical degradation is limited. Therefore, it should be noted that, considering the many factors, caution needs to be taken in the recycling of PVC , i.e. the incompatibility of virgin and recycled PVC, the formation of non-volatile residues, the stiffening effect of recycled PVC etc., especially for structural applications such as pipes.

## 4. Conclusions

In this study, the effect of using pre-consumer PVC scraps (which can be collected during pipe manufacturing process), as an alternative to post-consumer recycling, mixed with virgin pipe grade PVC on static and long-term mechanical properties is studied. Samples were prepared by blending virgin PVC with various contents of recycled PVC. The degradation characteristics were analyzed using various characterization tools. In addition, the fracture surfaces of test samples were carefully observed to understand the variation of fracture mechanisms of the samples.

No significant difference of molecular weight distribution was observed between the virgin PVC and recycled PVC. However, it is observed that the amount of non-volatile residues increases as the content of recycled PVC increases; also, the amount of residues of recycled PVC (10.76 wt%) is more than twice that of virgin PVC (4.97 wt%). Such a large amount of non-volatile residues in recycled PVC increases the inhomogeneity of the blend with recycled PVC. It is observed that, as the contents of recycled PVC increase, the amount of lead (Pb), which is the thermal stabilizer for recycling PVC, increases. In addition, the amount of ash and fillers such as $CaCO_3$ also increases by increasing the amount of recycled PVC. As the content of recycled PVC increases, the elastic modulus increases gradually, but the yield strength decreases up to 50% of the recy-

cled PVC and is recovered. The elongation to break and the impact strength rapidly decrease for 50% or more of recycled PVC; it can thus be observed that a high content of recycled PVC affects the toughness of the blend. The elements of residues observed from the fracture surface are characterized by energy-dispersive X-ray spectroscopy (EDS), and it is confirmed that all of residues contain $SiO_2$ and $CaCO_3$. The fatigue limit of V100R0 is measured as 11.5 MPa, but that of the blends is not easily defined experimentally. Unlike virgin PVC, the blends with recycled PVC do not show a clear fatigue limit due to the residues and inclusions; it can thus be expected that blends with recycled PVC may fail even at the very long fatigue cycles, unless such residues and inclusions are well controlled. The lowest fatigue strength is observed for the blend with 50% of recycled PVC. According to the fatigue test results, it can be understood that several factors such as the incompatibility of virgin and recycled PVC, the formation of non-volatile residues, the stiffening effect of recycled PVC etc., together affect the fatigue characteristics. In the case of V100R0, for most specimens a crack initiated from the edge of the specimen and grew into the specimen, which is a typical type of crack growth. However, once recycled PVC was added, macroscopic residues were observed at the crack initiation site, possibly causing the reduction of fatigue strength. In addition, unlike V100R0, it is observed that, as the contents of recycled PVC increase, the fracture surface becomes brittle; it is therefore difficult to observe any well-developed fibrillar deformation of the matrix material.

## References


[1] Attenberger P., Kufner T., Mieden O., Winter A.: Polyvinyl chloride (PVC). Kunststoffe International, **10**, 16–20 (2011).

[2] Kasper A. C., Bernaedes A. M., Veit H. M.: Characterization and recovery of polymers from mobile phone scrap. Waste Management and Research, **29**, 714–726 (2011).
DOI: 10.1177/0734242X10391528

[3] AWWA C900-07: Polyvinyl chloride (PVC) pressure pipe and fabricated fittings, 4 in. Through 12 in. (100 mm through 300 mm), for water transmission and distribution (2006).

[4] AWWA C905-10: Polyvinyl chloride (PVC) pressure pipe and fabricated fittings, 14 in. Through 48 in. (350 mm through 1,200 mm) (2009).

[5] Braun D.: Recycling of PVC. Progress in Polymer Science, **27**, 2171–2195 (2002).
DOI: 10.1016/S0079-6700(02)00036-9

[6] Sombatsompop N., Thongsang S.: Rheology, morphology, and mechanical and thermal properties of recycled PVC pipes. Journal of Applied Polymer Science, **82**, 2478–2486 (2001).
DOI: 10.1002/app.2098

[7] Ulutan S.: A recycling assessment of PVC bottles by means of heat impact evaluation on its reprocessing. Journal of Applied Polymer Science, **69**, 865–869 (1998).
DOI: 10.1002/(SICI)1097-4628(19980801)69:5<865::AID-APP4>3.0.CO;2-K

[8] Ma W., La Mantia F. P.: Processing and mechanical properties of recycled PVC and of homopolymer blends with virgin PVC. Journal of Applied Polymer Science, **59**, 759–767 (1996).
DOI: 10.1002/(SICI)1097-4628(19960131)59:5<759::AID-APP1>3.0.CO;2-V

[9] Arnold J. C., Maund B., Isaac D. H.: The mechanical properties of recycled PVC bottle compounds. Journal of Materials Processing Technology, **56**, 475–481 (1996).
DOI: 10.1016/0924-0136(95)01861-1

[10] Arnold J. C., Maund B.: The properties of recycled PVC bottle compounds. 1: Mechanical performance. Polymer Engineering and Science, **39**, 1234–1241 (1999).
DOI: 10.1002/pen.11510

[11] Garcia D., Balart R., Crespo E., Lopez J.: Mechanical properties of recycled PVC blends with styrenic polymer. Journal of Applied Polymer Science, **101**, 2464–2471 (2006).
DOI: 10.1002/app.23484

[12] Garcia D., Balart R., Sanchez L., López J.: Compatibility of recycled PVC/ABS blends. Effect of previous degradation. Polymer Engineering and Science, **47**, 789–796 (2007).
DOI: 10.1002/pen.20755

[13] Ajji A.: Morphology and mechanical properties of virgin and recycled polyethylene/polyvinyl chloride blends. Polymer Engineering and Science, **35**, 64–71 (1995).
DOI: 10.1002/pen.760350109

[14] Yoo Y., Kim S-S., Won J. C., Choi K-Y., Lee J. H.: Enhancement of the thermal stability, mechanical properties and morphologies of recycled PVC/clay nanocomposites. Polymer Bulletin, **52**, 373–380 (2004).
DOI: 10.1007/s00289-004-0296-7

[15] Yarahmadi N., Jakubowicz I., Gevert T.: Effects of repeated extrusion on the properties and durability of rigid PVC scrap. Polymer Degradation and Stability, **73**, 93–99 (2001).
DOI: 10.1016/S0141-3910(01)00073-8

[16] Nass L. I.: Encyclopedia of PVC, Vol. 3: Compounding processes, product design, and specifications. Mercel Dekker, New York (1992).

[17] Matuschek G., Milanov N., Kettrup A.: Thermoanalytical investigations for the recycling of PVC. Thermochimica Acta, **361**, 77–84 (2000).
DOI: 10.1016/S0040-6031(00)00549-9

[18] Anthony G. M.: Kinetic and chemical studies of polymer cross-linking using thermal gravimetry and hyphenated methods. Degradation of polyvinylchloride. Polymer Degradation and Stability, **64**, 353–357 (1999).
DOI: 10.1016/S0141-3910(98)00129-3

[19] McNeil I. C., Memetea L., Cole W. J.: A study of the products of PVC thermal degradation. Polymer Degradation and Stability, **49**, 181–191 (1995).
DOI: 10.1016/0141-3910(95)00064-S

[20] Benavides R., Castillo B. M., Castañeda A. O., López G. M., Arias G.: Different thermo-oxidative degradation routes in poly(vinyl chloride). Polymer Degradation and Stability, **73**, 417–423 (2001).
DOI: 10.1016/S0141-3910(01)00122-7

[21] La Mantia F. P.: Recycling of PVC and mixed plastic waste. ChemTec Publishing, Toronto (1996).

*eXPRESS Polymer Letters Vol.9, No.4 (2015) 372–383*
*Available online at www.expresspolymlett.com*
*DOI: 10.3144/expresspolymlett.2015.35*

# A new PDMS-b-PPO block copolymer membrane with novel *non-perforated* structure towards high flux for alcohol permselective pervaporation

*W. Liu*[1], *H. X. Guo*[2,3*], *S. L. Ji*[1,3], *H. J. Niu*[1], *J. R. Li*[1,3]

[1]College of Environmental and Energy Engineering, Beijing University of Technology, 100124 Beijing, PR China
[2]College of Materials Science and Engineering, Beijing University of Technology, 100124 Beijing, PR China
[3]Beijing Key Laboratory for Green Catalysis and Separation, 100124 Beijing, PR China

*Received 11 August 2014; accepted in revised form 24 October 2014*

**Abstract.** The effective permselective pervaporation of alcohol is one of key technology for bio-alcohol industrial production. In this work, a new polydimethylsiloxane-block-polyphenylene oxide (PDMS-b-PPO) copolymer was first synthesized by a bridge reagent technique. Based on the copolymer structure confirmation, the asymmetric PDMS-b-PPO membrane was subsequently prepared by phase-inversion method in order to improve the anti-swelling capacity of PDMS. SEM observation indicated that the morphology of as-prepared membrane exhibited a 'non-perforated' structure, resulting from the phase-inversion and micro-phase separation of the PDMS-b-PPO copolymer in the membrane forming process. Furthermore, the structure changes of the membranes with different ratio of PDMS to PPO were investigated. This non-perforated structure in the membrane favored to reduce the diffusion resistance, together with the affinity of PDMS segment to alcohol during pervaporation process. Thus, the prepared PDMS-b-PPO membrane showed dramatically increased flux, in pervaporation separation of alcohol/water mixture. The flux of the PDMS-b-PPO membrane (PDMS content of 42.4%) can reach 3816.8 g/(m$^2$·h), along with 8.53 of separation factor in pervaporation of 5 wt% alcohol/water mixture (60°C). This work may provide a new strategy to design and fabricate new copolymer membranes for improving alcohol permselective pervaporation.

***Keywords:*** *polymer membranes, alcohol permselective pervaporation, block copolymers, non-perforated structured membrane*

## 1. Introduction

Bio-alcohol has been promoted as a benign environmental source to solve energy problem worldwide [1–4]. The coupling of pervaporation (PV) and fermentation for bio-alcohol production has received increasing attention because the produced bio-alcohol can be timely in-situ recovered from fermentation using pervaporation technology [5, 6], so that the inhibition of fermentation from high alcohol concentration can be effectively reduced. Thus, the alcohol permselective pervaporation membrane with higher separation efficiency is one of the most important keys to accomplish the coupling of PV and fermentation.

Polydimethylsiloxane (PDMS) is one of the most representative membrane materials for pervaporation recovery of alcohols from their aqueous solutions, due to the advantages, such as high thermo-stability, hydrophobicity, low-surface tension, biocompatibility, and commercial availability. However, the wide utilization of PDMS is limited for its low glass transition temperature, difficult membrane-forming property, and poor cohesion, which lead to PDMS membrane cumbersome curing and lower anti-swelling

*Corresponding author, e-mail: hxguo@bjut.edu.cn

[7–13]. A few of modifications on PDMS have been made to improve these deficiencies, such as crosslinking, filling, graft, and block copolymerization [14–19], of which graft or block copolymerization offered an appealing route to generate new types of materials that combine the superior properties of multiple polymers. For example, Dong *et al*. [15] prepared poly(1-phenyl-1-propyne) (PPP)/PDMS graft copolymer membranes, in order to improve the anti-swelling capacity of PDMS. This PPP/PDMS membrane showed excellent permselectivity towards alcohol, acetone, dioxane, acetonitrile, and pyridine by pervaporation separation, due to that the rigid PPP chains of PPP/PDMS endowed the membrane a good anti-swelling capacity. Jiang *et al*. [20] has investigated a new kind of fluoridated siloxane-imide block copolymer (PSI) membrane for organic-pervaporation. This fluoridated imide blocks in the PSI improved the mechanical strength of the PDMS membranes without reducing its separation factors. Moreover, the similar modification of PDMS were carried out to synthesize polydimethylsiloxane-block-polymethylmethacrylate copolymer [21], polydimethylsiloxane-graft-polymethylmethacrylate copolymer [22], and polydimethylsiloxane/polystyrene interpenetrating polymer network [23]. All these works demonstrated that the poor properties of PDMS can be effectively improved by graft or block copolymerization with other relatively rigid polymers.

Polyphenylene oxide (PPO) is a thermoplastic polymer, which shows excellent chemical and thermal stability, and has been widely applied in pervaporation separation. For example, the asymmetric PPO membrane, prepared by Schauer *et al*. [24], has been applied in pervaporation separation of alcohol/water, which can permeate alcohol, preferentially. Herein, we regarded the rigid PPO polymer as a good candidate to combine with PDMS through graft or block copolymerization. Our previous work has fabricated a novel PDMS/bromide-substituted PPO (BPPO) membrane by *in situ* crosslinking method [25]. The results showed that existence of PPO really improved the anti-swelling capacity of PDMS, and the resultant PDMS/BPPO membrane exhibited a high selectivity towards butanol. However, the flux of such PDMS/BPPO membrane was not satisfactory due to its densely crosslinked structure. Therefore, to further improve flux of the membrane, this work synthesized a series of polydimethylsiloxane-block-polyphenylene oxide copolymers (PDMS-b-PPO) by reactive crosslinking method, using 2, 4-diisocyanatotoluene (TDI) as crosslinking reagent. Then, the asymmetric PDMS-b-PPO membranes were prepared by phase-inversion method. The morphologies and constituent of the membrane with tunable ratio of PDMS to PPO were investigated. The SEM results showed that the PDMS-b-PPO membrane presented a network porous structure both on the surfaces and in the cross-section, while the permeation and pervaporation tests showed that this porous membrane exhibited a '*non-perforated*' structure (porous but the pores were not truly through holes). This novel '*non-perforated*' structure led to a high flux in alcohol permselective pervaporation. This work may provide a new way to design and prepare asymmetric membrane with improved pervaporation performance, efficiently.

## 2. Experimentals

### 2.1. Materials

PDMS (KF-8008, average molecular weight of 11 400 g/mol, dual-terminated with aminopropyl group), was purchased from Japan's Shin-Etsu Chemical Industry Company. PPO (average molecular weight of 16 000 g/mol) was purchased from Hao Di Chemical Trading Company (Kun Shan, China). 2,4-diisocyanatotoluene (TDI), dibutyltin dilaurate (DBTDL), and chlorobenzene were supplied by Tianjin Fuchen Chemical Reagents Company (Tianjin, China). Analytically grade chlorobenzene, chloroform, methanol, alcohol, 2-propanol, and butanol were purchased from Beijing Chemical Company (Beijing, China).

### 2.2. Synthesis of polydimethylsiloxane-block-polyphenylene oxide copolymers (PDMS-b-PPO)

Calculated amount of PDMS, PPO and TDI were dissolved in chlorobenzene under stirring to obtain 10 wt% solutions, respectively. TDI solution was firstly transferred into a dried 500 mL flask. When the temperature of the flask was elevated at 80°C, the PPO solution was dropwise added into TDI solution under vigorous stirring and nitrogen atmosphere. Then, the PDMS solution together with 3 mL of DBTDL was added into the flask reactor. The temperature of the reaction system was elevated to 130°C and kept for 3 h. At last, the insoluble solids produced after cooled down to ambient temperature. The prod-

uct was filtrated and washed with methanol thoroughly, and the powder-like PDMS-b-PPO copolymers were collected and dried in a vacuum oven at 50°C for 48 h.

### 2.3. Preparation of PDMS-b-PPO membrane

The asymmetric PDMS-b-PPO membranes were prepared by phase inversion method. Typically, precalculated amount of PDMS-b-PPO and n-butyl alcohol was firstly dissolved in chloroform solvent to form a casting solution. The casting solution was spread on a level glass shutter by Gardner knife under ambient atmosphere. Then the glass shutter was immersed into a methanol coagulation bath. The as-obtained asymmetric PDMS-b-PPO membrane was peeled off and dried in a vacuum oven for 24 h.

### 2.4. Characterizations

The prepared PDMS-b-PPO copolymers were characterized by FTIR (Nicolet, 5DX instrument) and $^1$H-NMR analysis (Avance 400M, Bruker, Germany). The content of PDMS was calculated by the area ratio of the characteristic elements (mass fraction was equal to the product of the unit molecular weight and unit mole ratio. In this work, the area ratio is the unit mole ratio). The morphologies of membranes were characterized by SEM (Hitachi S-4300, Japan).

### 2.5. Pervaporation experiments

The pervaporation apparatus in this work is presented in Figure 1. The membrane was installed in a glass pervaporation cell with an operational area of 28 cm$^2$. The feed was circulated through the pervaporation cell by a peristaltic pump. The downstream pressure was kept at approximately 0.1 kPa by a vacuum pump. Permeate was collected through the condensation by liquid nitrogen. All the feeds are alcohol/water mixture with a ratio of 1:20 (5 wt % of the alcohol), and the operating temperature is 60°C. The feed and permeate compositions were analyzed by gas chromatography (GC7900, Tianmei Corporation, Shanghai, China), where the operating temperatures were 160°C in injector, 150°C in column and 160°C in detector. The separation factor was calculated from the quotient of the weight ratio of alcohol and water in the permeate, $Y_{alcohol}/Y_{water}$, and in the feed, $X_{alcohol}/X_{water}$ is given by Equation (1):

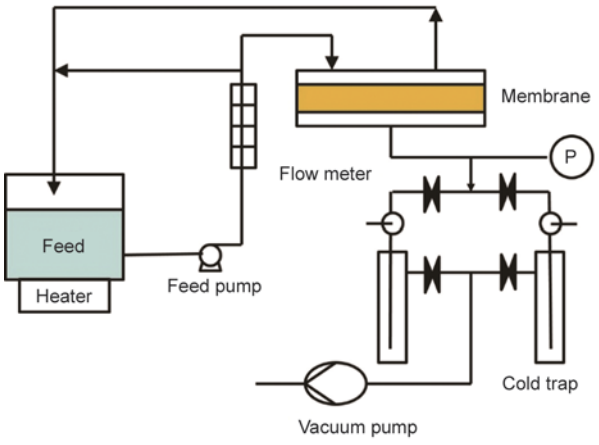


**Figure 1.** Scheme of experimental apparatus for pervaporation

$$\alpha = \frac{\frac{Y_{alcohol}}{Y_{water}}}{\frac{X_{alcohol}}{X_{water}}} \quad (1)$$

The flux ($J$) was calculated through weight of permeate ($W$) at unit time ($t$) and unit area ($A$) by Equation (2):

$$J = \frac{W}{t \cdot A} \ [g \cdot m^{-2} \cdot h^{-1}] \quad (2)$$

### 2.6. Permeation experiment

Permeation experiments were used to prove the '*non-perforated*' structure in the PDMS-b-PPO asymmetric membranes. The permeation test of PDMS-b-PPO membrane was conducted with an effective area of 26 cm$^2$. Deionized water and alcohol were used as the feeds. The experiments were carried out at a pressure of 0.6 MPa produced by a plunger pump. Permeations flux ($F$) were determined by measuring the volume of liquid collected over a measured time under steady-state conditions. $F$ was calculated as shown by Equation (3):

$$F = \frac{V}{t \cdot A} \ [mL \cdot m^{-2} \cdot h^{-1}] \quad (3)$$

where '$V$' is the permeate volume [mL], '$t$' stands for the time [hours], and '$A$' denote the effective membrane surface area [m$^2$].

## 3. Results and discussion

### 3.1. Synthesis and structures of PDMS-b-PPO copolymer

As illustrated in Figure 2, PDMS-b-PPO was synthesized by the reaction of the isocyano (–NCO) of TDI with aminopropyl (–$CH_2CH_2CH_2NH_2$) groups

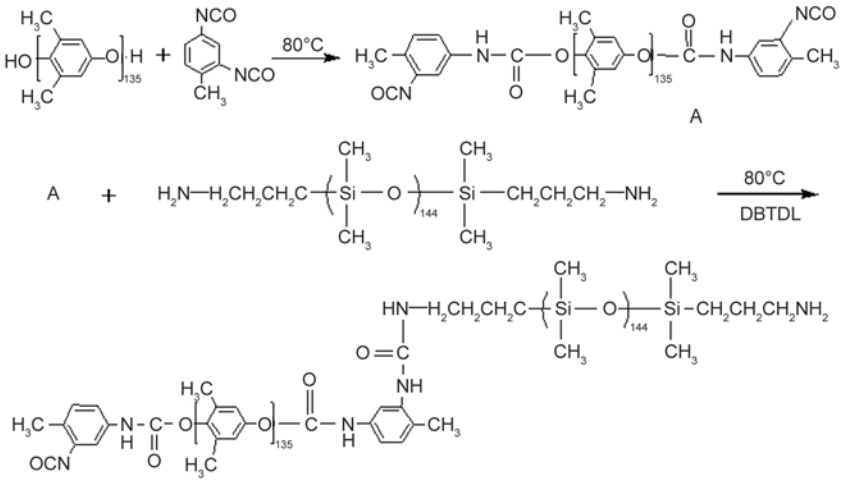


**Figure 2.** The reaction scheme of the formation of PDMS-b-PPO copolymer

of PDMS and hydroxyl (–OH) groups of PPO to form urethane and substituted urea group, respectively. The synthesis process was controlled by two stages. In the first stage, the reaction system was controlled at temperature of 80°C for one of isocyano (–NCO) of TDI to react with hydroxyl (–OH) group of PPO to form urethane, as well as in order to inhibit the self-polymerization of TDI. After the introduction of PDMS and dibutyltin dilaurate (DBTDL) solution, the other isocyano (–NCO) of TDI would be attacked by the aminopropyl group of PDMS in presence of dibutyltin dilaurate (DBTDL) other than –OH group of PPO because of the steric hindrance. Thus, the initial PDMS-b-PPO copolymer segments were formed. For the second stage, the temperature was further elevated and kept for 3 hrs. in order to complete the reaction.

To evidence of the formation of the PDMS-b-PPO copolymer, the FTIR spectra of PDMS, PPO, TDI, and PDMS-b-PPO were illustrated as in Figure 3. The PDMS spectrum in Figure 3 indicated typically the Si–O–Si stretching peak, $CH_3$ bending peak, $CH_3$ rocking peak, and C–H stretching peak appeared at 1100–1000, 1260, 797.35, and 2989 $cm^{-1}$, respectively. The spectra of PPO showed the benzene ring peak, C–O stretching peak, and $CH_3$ rocking peak appeared at 1468, 1306, and 857 $cm^{-1}$, respectively. And the peak at 2261 $cm^{-1}$ clearly indicated –N=C=O of TDI. In contrast, the characteristic peaks of PDMS and PPO are presented in the spectrum of PDMS-b-PPO copolymer. Meanwhile, the characteristic peak of TDI disappeared and a new peak appeared at 1711.9 $cm^{-1}$, which was ascribed to the produced urethane group. These results indicated that the PDMS-b-PPO was really formed.

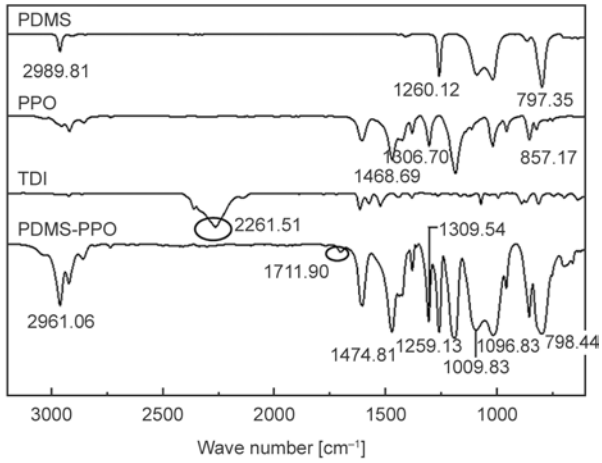


**Figure 3.** FTIR spectra of PDMS, PPO, TDI and PDMS-b-PPO copolymers

The typical $^1$H-NMR spectrum of the PDMS-b-PPO copolymers was shown in Figure 4. The peak at 7.256 ppm of Figure 4 was ascribed to the characteristic peak of deuterated chloroform solvent.

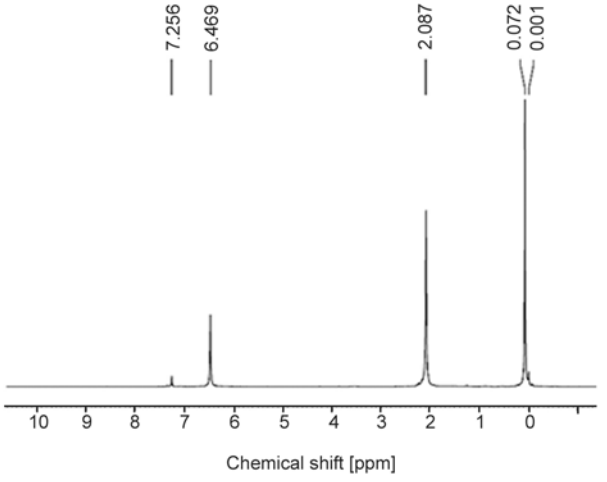


**Figure 4.** $^1$H-NMR spectra of PDMS-b-PPO copolymer

And the two peaks at 6.469 and 2.087 ppm were ascribed to the proton of aromatic and methyl group of PPO, respectively, and the peak at 0.072 ppm was attributed to the proton of siloxane. The area ratio of the three signals at 6.469, 2.087 and 0.072 ppm was used to calculate the PDMS content.

### 3.2. The morphologies of as-prepared PDMS-b-PPO membrane

Generally, PDMS cannot be directly formed into an asymmetric membrane by phase-inversion method because of its poor mechanical property. However, our PDMS-b-PPO copolymer can form a wholly continuous non-substrate membrane by phase-inversion method, due to existence of more rigid PPO segments. As shown in Figure 5, the surface and cross-section morphologies of the membranes indicated that the surface morphology of PPO asymmetric membrane (Figure 5a) was very dense and compact, and its cross-section (Figure 5b) exhibited a typical pear-shaped finger-like structure. In contrast, the surface of our PDMS-b-PPO membrane (prepared by the ratio of PDMS:PPO:TDI was 1.5:1:2) was porous-like (Figure 5c) with pore size of about 100 nm. But the enlarged image in the inset of Figure 5c indicated that the surface displayed much non-perforated pores. And the image of the cross-section (Figure 5d) showed a sponge-like network structure with pore size about 0.5–1.0 μm. The formed novel morphology of the PDMS-b-PPO membrane was mainly resulted from the specific hard and soft segments of the copolymers and the membrane-forming processes; that is, the microphase separation of the block copolymers and the phase-inversion process. As illustrated in Figure 6, when the casting solution consisting of PDMS-b-PPO dissolved in n-butyl alcohol and chloroform was spread onto a glass shutter and then immersed into methanol

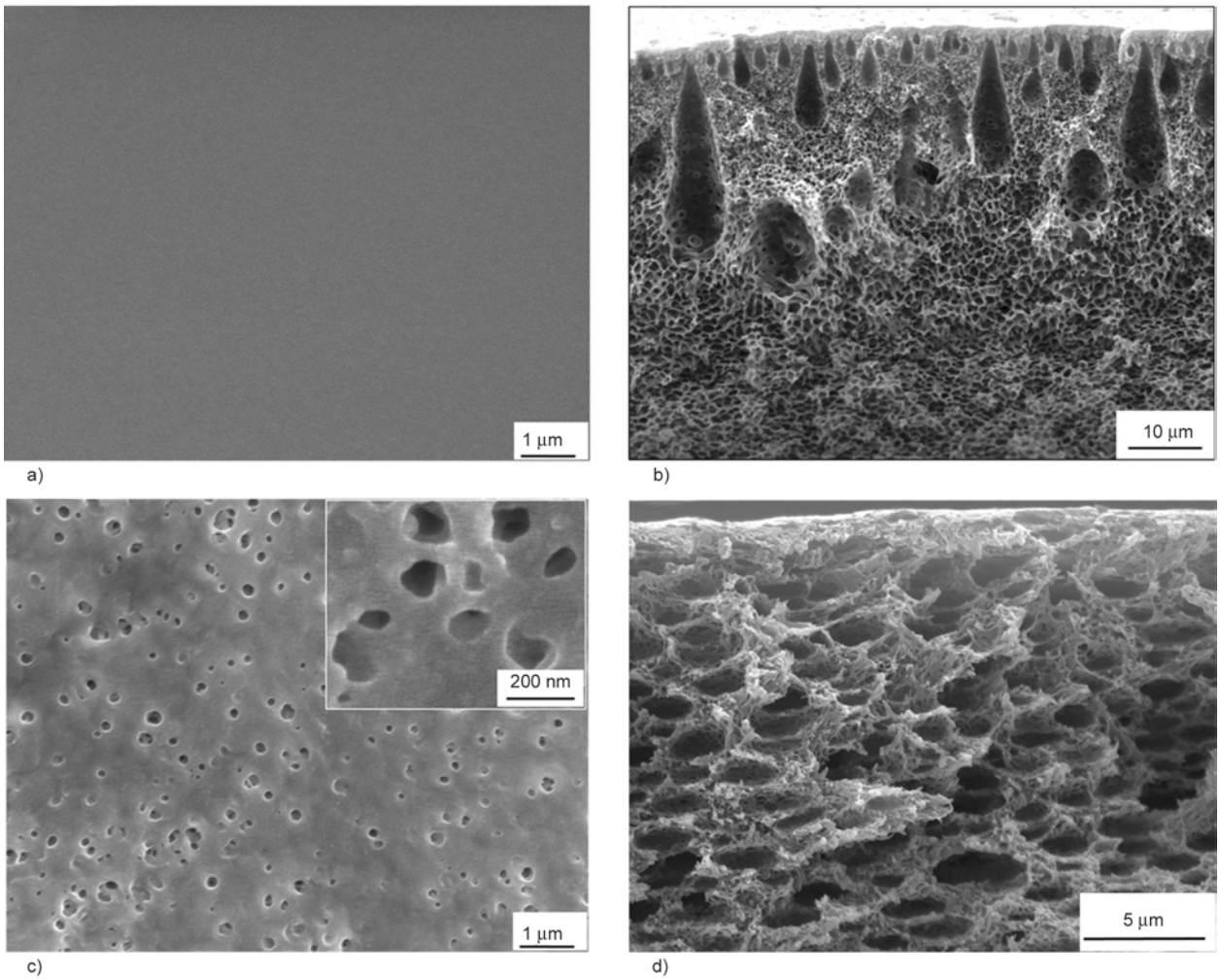


**Figure 5.** The SEM of the surface and the cross-section of PDMS-b-PPO membrane. a) surface of PPO asymmetric membrane; b) cross-section of PPO asymmetric membrane; c) surface of PDMS-b-PPO membrane; d) cross-section of PDMS-b-PPO membrane (PDMS:PPO:TDI =1.5:1:2).

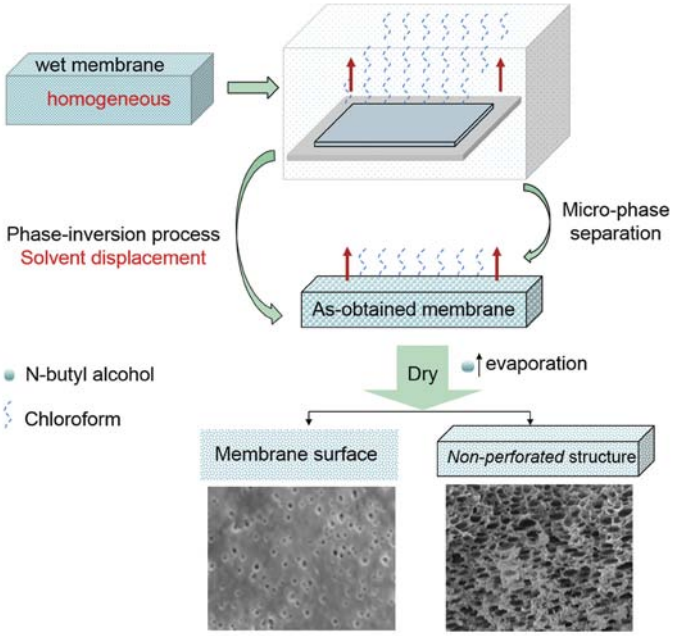


**Figure 6.** Phase-inversion process of PDMS-b-PPO membrane

coagulation bath, the phase inversion occurred. The solvent displacement between liquid component and gel proceed due to the existence of poor and rich phase region in the PDMS-b-PPO membrane, resulting in the porous structure. Furthermore, during membrane forming process, the solvent of n-butyl alcohol could be partially displaced by methanol when immersed into methanol coagulation bath, due to the compatibility between PDMS and n-butyl alcohol. Thus, the cross section of the PDMS-b-PPO membrane appeared as sponge-like other than finger-like structure. Moreover, when the phase inversion finished, the PDMS domains in outer skin layer of PDMS-b-PPO were swollen by methanol and n-butyl alcohol. And these wrapped solvents evaporated during drying, resulting in the shrinkage of PDMS segment and occurrence of subsidence areas, much similar to the porous-like but non-perforated structure. Simultaneously, the micro-phase separation of the as-prepared PDMS-b-PPO, resulting from the soft PDMS segment and the rigid PPO chain, caused that PDMS micro-region was uniformly dispersed in the PPO matrix to form such porous-like structure. The component of this micro-region can be further demonstrated by EDS shown in Figure 7. The blue points of Si element and the red points of C element in Figure 7 obviously indicated that the PDMS component in the blue Si domains was uniformly dispersed in the PPO matrix.

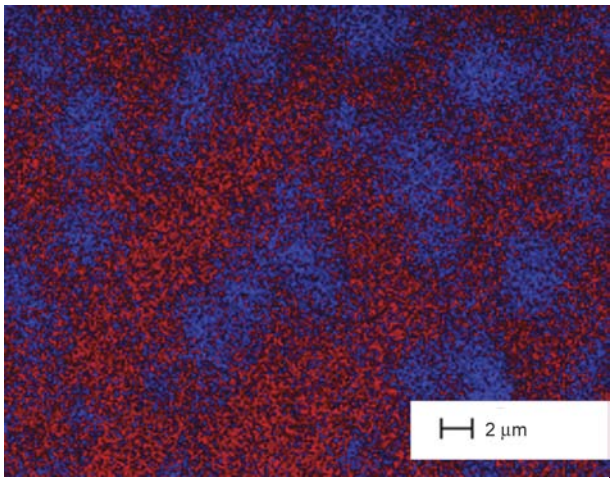


**Figure 7.** EDS scanning image of the PDMS-b-PPO membrane (blue points standardized Si element and the red points standardized C element)

To further demonstrate the porous-like but *non-perforated* structure of the surface and the cross-section of PDMS-b-PPO membrane, the permeation of aqueous solution was performed. Both of PPO and the PDMS-b-PPO asymmetric membrane were prepared by the phase-inversion method under the same conditions. The results in Figure 8 indicated that the pores in Figure 5b and 5d were not truly through holes, and really exhibited a non-perforated structure. When the feed liquid was water, the permeations of PPO and PDMS-b-PPO membrane were 3.0 and 15.0 mL/($m^2$·h) under 0.6 MPa, respectively.

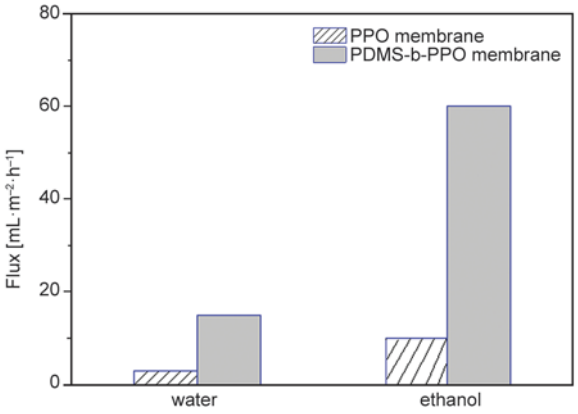


**Figure 8.** Permeation results of PPO membrane and PDMS-b-PPO membrane

The low permeation of pure water under relatively higher pressure demonstrated that the PPO membrane and PDMS-b-PPO membrane were dense and the water was difficult to permeate through. However, when the feed liquid was changed into alcohol, the permeation of the PPO membrane and PDMS-b-PPO membrane were increased to 10.0 and 60 mL/($m^2$·h) under the same pressure, respectively. This was due to the better affinity between PDMS and alcohol. And the PDMS-b-PPO membrane showed a relatively higher permeation for alcohol. Thus, we can deduce that the porous structure of the PDMS-b-PPO membrane in Figure 5 was really non-perforated.

### 3.3. The effect of raw material ratio on the structure of PDMS-b-PPO membranes

To investigate the effect of the soft and rigid segment in PDMS-b-PPO copolymers on the structure of the membrane, series of PDMS-b-PPO copolymers with different constituents were prepared by different ratio of PDMS to PPO. The PDMS content in the PDMS-b-PPO copolymer was measured using $^1$H-NMR area ratio as shown in Table 1. The results of Table 1 indicated that the PDMS content was some close to the theoretical ones. The relatively low PDMS contents in sample 3, 4, 5 of Table 1 may be probably due to that the excessive amount of TDI brought about the crosslinking structure, of which the long molecular chains increased the measurement error. Moreover, the content of PDMS in the copolymer increased with increasing the ratio of PDMS to PPO, indicating that the composition of soft PDMS segments and rigid PPO segments in PDMS-b-PPO copolymers could be effectively tuned by the ratio of PDMS to PPO.

**Table 1.** The variation of PDMS content in the copolymers with different ratio of PDMS to PPO

| Sample | PDMS:PPO:TDI (mole ratio) | PDMS [wt%] | |
|---|---|---|---|
| | | Theoretically added | Measured |
| 1 | 0.5:1:2 | 26.27 | 24.14 |
| 2 | 1:1:2 | 41.61 | 37.02 |
| 3 | 1.5:1:2 | 51.66 | 42.40 |
| 4 | 1:1:3 | 41.61 | 32.38 |
| 5 | 1:1:4 | 41.61 | 30.75 |

The morphologies of PDMS-b-PPO membrane with different ratio of PDMS to PPO on were investigated by SEM. As shown in Figure 9, all the PDMS-b-PPO membranes exhibited '*non-perforated*' porous-like structure. When the ratio of PDMS:PPO:TDI changed from 0.5:1:2 to 1.5:1:2, the PDMS content in PDMS-b-PPO increasing from 24.14 to 42.40 wt%, and the corresponding images shown in Figure 9A, 9B, and 9C, indicated that the irregular and small pores existed in the surface and cross-section of membrane with the ratio of PDMS:PPO:TDI as 0.5:1:2, due to the low amount of soft PDMS segment in the copolymer. When the soft PDMS segment of the copolymer chains increased, the pores in the surface and the cross-section of membrane became relatively lager (Figure 9B and Figure 9C), resulting from that the increased PDMS brought about higher degree of microphase separation. Moreover, when the ratio of PDMS:PPO:TDI changed from 1:1:2 to 1:1:4 as shown in Figure 9B, 9D, and 9E, the surface and cross-section of the PDMS-b-PPO membrane became denser and even compact (Figure 9D-s). This was attributed to that the excessive amount of TDI may produce some crosslinking structure in the membrane and resulted in the restricted micro-phase separation process during formation of membrane. Therefore, the results in Figure 9 indicated that the morphology of such '*non-perforated*' PDMS-b-PPO membrane can be tuned by changing the ratio of soft PDMS and rigid PPO.

### 3.4. Pervaporation separation of the alcohol/water binary mixtures

Figure 10 showed the effect of TDI amount on the pervaporation performances in the separation of alcohol/water, 2-propanol/water, and t-butanol/water mixtures. It can be noted that the separation factor and flux PDMS-b-PPO membrane decreasing with the increased of TDI amount. This was in accordance with the gradually denser and more compact

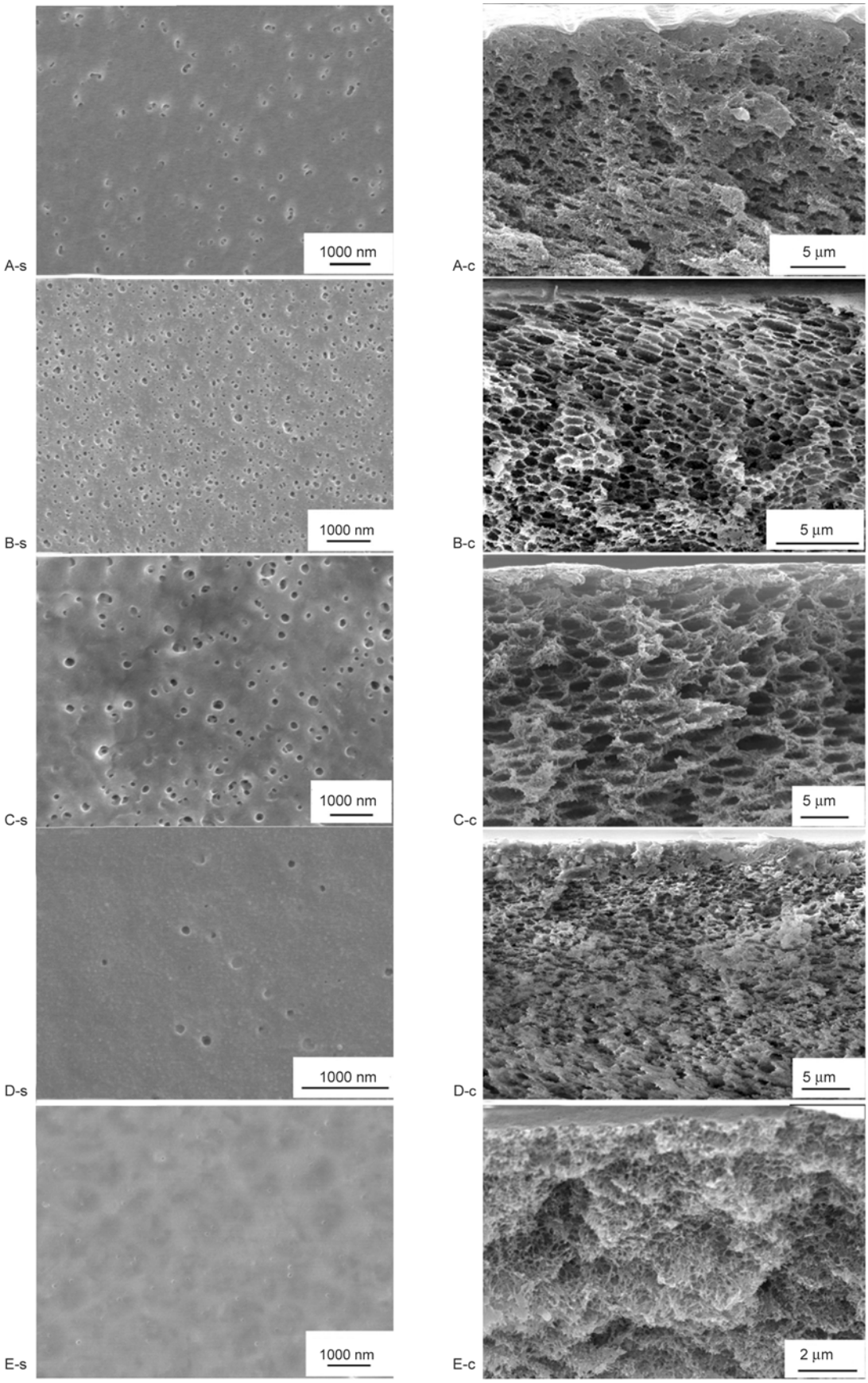


**Figure 9.** The SEM images of the membranes with different ratios of PDMS: PPO: TDI. '*s*' represent the surface and '*c*' represent cross-section. (A) PDMS:PPO:TDI=0.5:1:2 polymer membrane, (B) PDMS:PPO:TDI=1:1:2 polymer membrane, (C) PDMS:PPO:TDI = 1.5:1:2 polymer membrane, (D) PDMS:PPO:TDI=1:1:3 polymer membrane, (E) PDMS:PPO:TDI =1:1:4 polymer membrane.

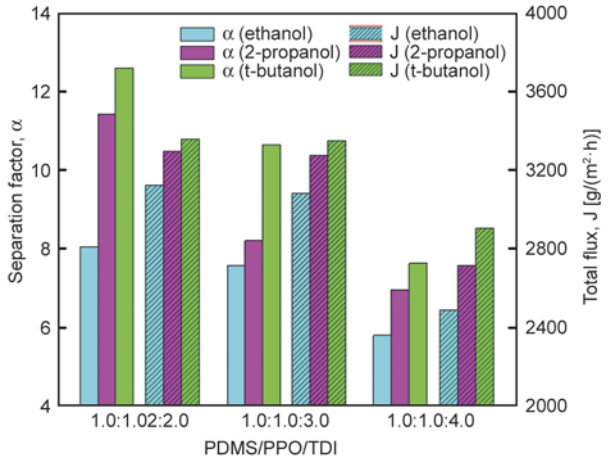


**Figure 10.** The effect of TDI amount on the pervaporation performances in the separation of alcohol/water, 2-propanol/water, and t-butanol/water mixtures

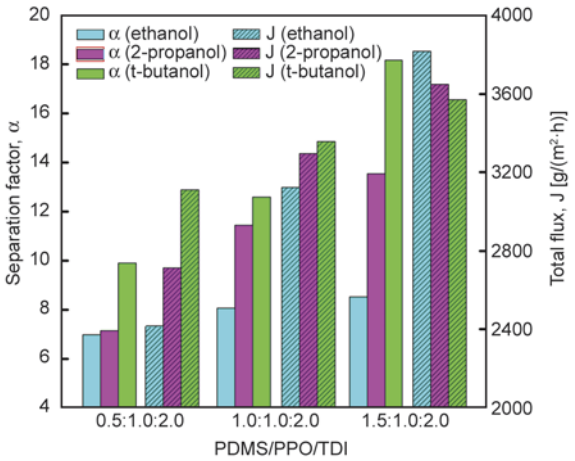


**Figure 11.** The effect of PDMS content in PDMS-b-PPO on pervaporation performances

structure of Figure 9B, 9D, and 9E. Moreover, based on the results of Table 1, more usage of TDI resulted in some crosslinked PDMS-b-PPO. The microphase separation process of PDMS-b-PPO was then restricted, and the shrinkage of PDMS segment caused the surface and the cross-section became less porous and relatively compact. Thus, the separation factor and flux of PDMS-b-PPO membrane decreased. When the ratio of PDMS: PPO: TDI was 1:1:2 (PDMS content is 37.02%), the prepared membrane exhibited an optimum pervaporation performance. The separation factor ($\alpha$) and flux ($J$) were 8.06 and 3150.7 g/(m$^2$·h) for alcohol/water mixture, 11.35 and 3390.8 g/(m$^2$·h) for 2-propanol/water and 12.7 and 33456.1 g/(m$^2$·h) for t-butanol/water mixture, respectively, with 5 wt% of the feed concentration and at 60°C of operation temperature. Figure 11 showed the effect of PDMS content in PDMS-b-PPO on pervaporation performances in the separation of alcohol/water, 2-propanol/water and t-butanol/water mixtures. It was noted that the separation factor and flux PDMS-b-PPO membrane increased with increasing of PDMS content, which was also in accordance with the variation of morphologies of Figure 9A to 9C. This was probably due to that the more amount of PDMS led to a relatively larger PDMS domains on the surface and a looser and porous cross-section in the membrane (Figure 9C), which resulted in increased efficient contact areas and reduced mass transfer resistance of the membrane. Therefore, the flux of PDMS-b-PPO membrane was enhanced. This optimum pervaporation performance can be further illustrated from the porous '*non-perforated*' structure of the membrane shown in Figure 9C. When the ratio of PDMS:PPO: TDI was 1.5:1:2 (PDMS content is 42.4%), the feed concentration was 5 wt%, and the operation temperature was 60°C, the optimum pervaporation separation behavior was achieved. The separation factor

**Table 2.** The pervaporation performance of membranes in reference (In the system of ethanol/water)

| Membrane | Ethanol concentration [wt%] | Temperature [°C] | Flux [kg/(m$^2$·h)] | Separation factor | Reference |
|---|---|---|---|---|---|
| Crosslinked PDMS containing vinyl groups | 16.5 | 40 | 0.085 | 8 | [26] |
| Crosslinked PDMS containing acetoxysilyl groups | 8 | 30 | 0.0251 | 10.8 | [11] |
| PDMS-PS IPN supported on PESF | 10 | 60 | 0.16 | 5.5 | [27] |
| PDMS film treated with octadecyldiethoxymethylsilane | 4.0 | 25 | 0.016 | 16.3 | [28] |
| PDMS supported on PTFE | 1.5 | 60 | 1.53 | 14 | [29] |
| PDMS supported on CA | 5 | 40 | 1.3 | 8.5 | [12] |
| PTMSP | 6 | 30 | 0.44 | 15.1 | [30] |
| PTMSP modified with PFA-g-PDMS | 10 | 25 | 0.6 | 20 | [31] |
| Plasma modified with octadecyldiethoxymethylsilane | 4 | 25 | 0.015 | 18 | [28] |
| PDMS-PI copolymer | 10 | 60 | 0.56 | 10.6 | [32] |
| PEO-CS blend polymer | 8 | 20 | 0.9 | 4.4 | [33] |
| Silicalite filled PDMS | 5.5 | 22.5 | 0.05 | 16.5 | [34] |
| PDMS-b-PPO asymmetric membrane | 5 | 60 | 3.816 | 8.53 | This work |

and flux reached 8.53 and 3816.8 g/($m^2$·h) for alcohol/water mixture, 13.54 and 3650.0 g/($m^2$·h) for 2-propanol /water and 18.18 and 3571.0 g/($m^2$·h) for t-butanol/water mixture, respectively.

Table 2 shows the pervaporation performance of other polymeric membranes. As can be shown, our PDMS-b-PPO asymmetric membrane exhibit better flux than that of the reported polymeric membranes while the separation factors maintained on a relatively high level [26–34].

## 4. Conclusions

PDMS-b-PPO membranes were successfully prepared for pervaporation separation of alcohol/water mixtures. The membranes showed a '*non-perforated*' structure and high flux in alcohol permselective pervaporation. With the increasing of PDMS content and the decreasing of TDI amounts, the sponge-like structure of PDMS-b-PPO membranes became looser and the PDMS shrinkage domains on surface increased, resulting in the improved separation performance. When the ratio of PDMS: PPO:TDI was 1.5:1:2, the separation factor and flux reached 8.53 and 3816.8 g/($m^2$·h) for alcohol/water mixture, 13.54 and 3650.0 g/($m^2$·h) for 2-propanol/water and 18.18 and 3571.0 g/($m^2$·h) for t-butanol/water mixture, respectively. This higher flux for alcohol was attributed to the specific '*non-perforated*' structure, which enhanced efficient contact areas and reduced the mass transfer resistance of the membrane. This work provides a new way to design and develop the novel alcohol permselective pervaporation membranes.

## Acknowledgements

This work was financially supported by the National High Technology Research and Development Program of China (NO. 2012AA03A607) and the National Natural Science Foundation of China (NO. 20876003, 21176007 and 21322601).

## References

[1] Kheshgi H. S., Prince R. C., Marland G.: The potential of biomass fuels in the context of global climate change: Focus on transportation fuels. Annual Review of Energy and the Environment, **25**, 199–244 (2000). DOI: 10.1146/annurev.energy.25.1.199

[2] Roca C., Olsson L.: Increasing ethanol productivity during xylose fermentation by cell recycling of recombinant *Saccharomyces cerevisiae*. Applied Microbiology and Biotechnology, **60**, 560–563 (2003). DOI: 10.1007/s00253-002-1147-9

[3] Chum H. L., Overend R. P.: Biomass and renewable fuels. Fuel Processing Technology, **71**, 187–195 (2001). DOI: 10.1016/S0378-3820(01)00146-1

[4] Çakır T., Arga K. Y., Altıntaş M. M., Ülgen K. O.: Flux analysis of recombinant *Saccharomyces cerevisiae* YPB-G utilizing starch for optimal ethanol production. Process Biochemistry, **39**, 2097–2108 (2004). DOI: 10.1016/j.procbio.2003.10.010

[5] Shao P., Huang R. Y. M.: Polymeric membrane pervaporation. Journal of Membrane Science, **287**, 162–179 (2007). DOI: 10.1016/j.memsci.2006.10.043

[6] Sae-Khow O., Mitra S.: Pervaporation in chemical analysis. Journal of Chromatography A, **1217**, 2736–2746 (2010). DOI: 10.1016/j.chroma.2009.12.043

[7] Xiangli F. J., Wei W. Chen Y. W., Jin W. Q., Xu N. P.: Optimization of preparation conditions for polydimethylsiloxane (PDMS)/ceramic composite pervaporation membranes using response surface methodology. Journal of Membrane Science, **311**, 23–33 (2008). DOI: 10.1016/j.memsci.2007.11.054

[8] Sun H., Lu L., Chen X., Jiang Z.: Pervaporation dehydration of aqueous ethanol solution using H-ZSM-5 filled chitosan membranes. Separation and Purification Technology, **58**, 429–436 (2008). DOI: 10.1016/j.seppur.2007.09.012

[9] Lai J. Y., Li S-H., Lee K-R.: Permselectivities of polysiloxaneimide membrane for aqueous ethanol mixture in pervaporation. Journal of Membrane Science, **93**, 273–282 (1994). DOI: 10.1016/0376-7388(94)00097-2

[10] Li L., Xiao Z., Tan S., Liang P., Zhang Z. B.: Composite PDMS membrane with high flux for the separation of organics from water by pervaporation. Journal of Membrane Science, **243**, 177–187 (2004). DOI: 10.1016/j.memsci.2004.06.015

[11] Ishihara K., Matsui K.: Pervaporation of ethanol-water mixture through composite membranes composed of styrene-fluoroalkyl acrylate graft copolymers and cross-linked polydimethylsiloxane membrane. Journal of Applied Polymer Science, **34**, 437–440 (1987). DOI: 10.1002/app.1987.070340135

[12] Ahmed I., Pa N. F. C., Nawawi M. G. M., Rahman W. A. W. A.: Modified polydimethylsiloxane/polystyrene blended IPN pervaporation membrane for ethanol/water separation. Journal of Applied Polymer Science, **122**, 2666–2679 (2011). DOI: 10.1002/app.34319

[13] Nagase Y., Mori S., Matsui K.: Chemical modification of poly(substituted-acetylene). IV. Pervaporation of organic liquid/water mixture through poly(1-phenyl-1-propyne)/polydimethylsiloxane graft copolymer membrane. Journal of Applied Polymer Science, **37**, 1259–1267 (1989).
DOI: 10.1002/app.1989.070370510

[14] Lunn D. J., Boott C. E., Bass K. E., Shuttleworth T. A., McCreanor N. G., Papadouli S., Manners I.: Controlled thiol-ene functionalization of polyferrocenylsilane-block-polyvinylsiloxane copolymers. Macromolecular Chemistry and Physics, **214**, 2813–2820 (2013).
DOI: 10.1002/macp.201300520

[15] Dong J., Liu Z., Han N., Wang Q., Xia Y.: Preparation, morphology, and mechanical properties of elastomers based on α,ω-dihydroxy-polydimethylsiloxane/polystyrene blends. Journal of Applied Polymer Science, **92**, 3542–3548 (2004).
DOI: 10.1002/app.20394

[16] Kitagawa M., Takegami S., Tokiwa Y.: Free-radical polymerization of a reducing vinyl sugar ester in dimethylformamide and water. Macromolecular Rapid Communications, **19**, 155–158 (1998).
DOI: 10.1002/(SICI)1521-3927(19980301)19:3<155::AID-MARC155>3.0.CO;2-W

[17] Miyata T., Obata S., Uragami T.: Annealing effect of microphase-separated membranes containing poly (dimethylsiloxane) on their permselectivity for aqueous ethanol solutions. Macromolecules, **32**, 8465–8475 (1999).
DOI: 10.1021/ma9909612

[18] Zhao Q., Qian J. W., An Q. F., Zhu Z. H., Zhang P., Bai Y. X.: Studies on pervaporation characteristics of polyacrylonitrile–*b*-poly(ethylene glycol)–*b*-polyacrylonitrile block copolymer membrane for dehydration of aqueous acetone solutions. Journal of Membrane Science, **311**, 284–293 (2008).
DOI: 10.1016/j.memsci.2007.12.023

[19] Jha A. K., Chen L., Offeman R. D., Balsara N. P.: Effect of nanoscale morphology on selective ethanol transport through block copolymer membranes. Journal of Membrane Science, **373**, 112–120 (2011).
DOI: 10.1016/j.memsci.2011.02.043

[20] Jiang Y., Shi H., Cai M., Liang Y., Li B., Zhang H., Song R.: Synthesis and characterization of PS-*b*-PDMS-*b*-PS triblock copolymer. Journal of Applied Polymer Science, **129**, 247–252 (2013).
DOI: 10.1002/app.38726

[21] Miyata T., Obata S., Uragami T.: Morphological effects of microphase separation on the permselectivity for aqueous ethanol solutions of block and graft copolymer membranes containing poly(dimethylsiloxane). Macromolecules, **32**, 3712–3720 (1999).
DOI: 10.1021/ma981949x

[22] Miyata T., Takagi T., Uragami T.: Microphase separation in graft copolymer membranes with pendant oligodimethylsiloxanes and their permselectivity for aqueous ethanol solutions. Macromolecules, **29**, 7787–7794 (1996).
DOI: 10.1021/ma960663u

[23] Miyata T., Higuchi J-I., Okuno H., Uragami T.: Preparation of polydimethylsiloxane/polystyrene interpenetrating polymer network membranes and permeation of aqueous ethanol solutions through the membranes by pervaporation. Journal of Applied Polymer Science, **61**, 1315–1324 (1996).
DOI: 10.1002/(SICI)1097-4628(19960822)61:8<1315::AID-APP11>3.0.CO;2-Y

[24] Schauer J., Sysel P., Marousek V., Pientka Z., Pokorný J., Bleha M.: Pervaporation and gas separation membranes made from polyimide/polydimethylsiloxane block copolymer. Journal of Applied Polymer Science, **61**, 1333–1337 (1996).
DOI: 10.1002/(SICI)1097-4628(19960822)61:8<1333::AID-APP13>3.0.CO;2-#

[25] Liu W., Ji S-L., Guo H-X., Gao J., Qin Z-P.: *In situ* cross-linked-PDMS/BPPO membrane for the recovery of butanol by pervaporation. Journal of Applied Polymer Science, **131**, 4004/1–4004/9 (2014).
DOI: 10.1002/app.40004

[26] Takegami S., Yamada H., Tsujii S.: Pervaporation of ethanol/water mixtures using novel hydrophobic membranes containing polydimethylsiloxane. Journal of Membrane Science, **75**, 93–105 (1992).
DOI: 10.1016/0376-7388(92)80009-9

[27] Liang L., Ruckenstein E.: Pervaporation of ethanol-water mixtures through polydimethylsiloxane-polystyrene interpenetrating polymer network supported membranes. Journal of Membrane Science, **114**, 227–234 (1996).
DOI: 10.1016/0376-7388(95)00319-3

[28] Kashiwagi T., Okabe K., Okita K.: Separation of ethanol from ethanol/water mixtures by plasma-polymerized membranes from silicone compounds. Journal of Membrane Science, **36**, 353–362 (1988).
DOI: 10.1016/0376-7388(88)80028-0

[29] Mori Y., Inaba T.: Ethanol production from starch in a pervaporation membrane bioreactor using *Clostridium thermohydrosulfuricum*. Biotechnology and Bioengineering, **36**, 849–853 (1990).
DOI: 10.1002/bit.260360815

[30] Volkov V. V., Fadeev A. G., Khotimsky V. S., Litvinova E. G., Selinskaya Y. A., McMillan J. D., Kelley S. S.: Effects of synthesis conditions on the pervaporation properties of poly[1-(trimethylsilyl)-1-propyne] useful for membrane bioreactors. Journal of Applied Polymer Science, **91**, 2271–2277 (2004).
DOI: 10.1002/app.13358

[31] Uragami T., Doi T., Miyata T.: Control of permselectivity with surface modifications of poly[1-(trimethylsilyl)-1-propyne] membranes. International Journal of Adhesion and Adhesives, **19**, 405–409 (1999).
DOI: 10.1016/S0143-7496(98)00064-5

[32] Krea M., Roizard D., Moulai-Mostefa N., Sacco D.: New copolyimide membranes with high siloxane content designed to remove polar organics from water by pervaporation. Journal of Membrane Science, **241**, 55–64 (2004).
DOI: 10.1016/j.memsci.2004.03.040

[33] Wang X-P., Shen Z-Q., Zhang F-Y., Zhang Y-F.: Preferential separation of ethanol from aqueous solution through hydrophilic polymer membranes. Journal of Applied Polymer Science, **73**, 1145–1151 (1999).
DOI: 10.1002/(SICI)1097-4628(19990815)73:7<1145::AID-APP6>3.0.CO;2-B

[34] te Hennepe H. J. C., Bargeman D., Mulder M. H. V., Smolders C. A.: Zeolite-filled silicone rubber membranes: Part 1. Membrane preparation and pervaporation results. Journal of Membrane Science, **35**, 39–55 (1987).
DOI: 10.1016/S0376-7388(00)80921-7

*eXPRESS Polymer Letters Vol.9, No.4 (2015) 384–393*
*Available online at www.expresspolymlett.com*
*DOI: 10.3144/expresspolymlett.2015.36*

# Inverse effect in simultaneous thermal and radiation aging of EVA insulation

*G. Przybytniak[1*], J. Boguski[1], V. Placek[2], L. Verardi[3], D. Fabiani[3], E. Linde[4], U. W. Gedde[4]*

[1]Institute of Nuclear Chemistry and Technology, Dorodna 16, 03-195 Warsaw, Poland
[2]Ustav Jaderneho Vyzkumu A.S., Husinec – Řež, Hlavní 130, 250 68, Czech Republic
[3]Laboratory of Innovation Technologies (DEI-LIT), University of Bologna, Viale Risorgimento 2, 40136 Bologna, Italy
[4]KTH Royal Institute of Technology, School of Chemical Science and Engineering, Fiber and Polymer Technology, SE-100 44 Stockholm, Sweden

*Received 11 August 2014; accepted in revised form 29 October 2014*

**Abstract.** Poly(ethylene-*co*-vinyl acetate) (EVA) insulation of the cable applied in nuclear power plants was accelerated aged by gamma-rays at two various temperatures, namely 55 and 85°C. Radiation degradation in the dose range of 0–1500 kGy was monitored using a Differential Scanning Calorimetry method by measuring oxidative induction temperature (OITp), gel fraction, mechanical and electrical tests. It was confirmed that a dose rate effect in the range of 420–1500 Gy/h was negligible whereas progress of degradation with increasing dose was strongly temperature dependent. For the insulation accelerated aged at 85°C the OITp and permittivity measurements confirmed lower degradation than for the specimens radiation treated at 55°C at the same dose rates. It was postulated that an inverse thermal effect resulted from radiation induced cross-linking facilitated by melting of EVA crystallites at 85°C.

***Keywords:*** *material testing, radiation degradation, thermal degradation, inverse thermal effect, poly(ethylene-co-vinyl acetate)*

## 1. Introduction

Reliability of the cables operating in Nuclear Power Plant (NPP) is usually estimated by the condition monitoring tests followed by accelerated aging. This approach is necessary as with increasing service time polymers, the crucial components of insulations and jackets, degrade gradually predominantly due to exposure to two adverse stressors associated with gamma radiation and elevated temperatures. In the past, various procedures were implemented for conducting the initial and on-going qualifications of the NPP cables [1].

During accelerated aging performed in the first stage of the procedure, intensities of both degrading factors (i.e. radiation and heating) vary significantly, depending on the possibilities of testing laboratories. In spite of the recommendations presented in IAEA reports that the acceleration factor for absorbed dose should not exceed 250 [2], the value in many conducted experiments is often higher and depends on the access to the particular type of gamma chambers equipped with an installation for thermal heating. Additionally, many tests are performed applying periodically heating and exposure to ionizing radiation, in spite of the fact that under real conditions in NPPs both stressors operate simultaneously and that the final effect of degradation varies depending on the applied procedure. Therefore, in our studies the second modus operandi, better suited to the NPP realities, was applied.

It is generally accepted that thermal condition monitoring techniques are convenient for the analysis of

*Corresponding author, e-mail: g.przybytniak@ichtj.waw.pl

polymer degradation as they are sensitive, accessible, relatively simple and require a small sample weight [3–5]. Additionally, they might be applied for a variety of plastics for which accelerated aging induces changes in the thermal features. In this group of materials is poly(ethylene-*co*-vinyl acetate) (EVA) being the object of the reported studies. The polymer characterizes high electrical resistivity, low processing temperature and water wettability.

DSC thermograms of EVA reveal two or more peaks corresponding to the ethylene domains of the copolymer. As a semicrystalline material, it shows a very broad melting transition because of wide dispersion of the crystallite sizes and the variety of imperfections in the ordered phase [6, 7]. The DSC method is also used in isothermal mode for measuring oxidative induction time (OIT) related to the copolymer stability [8–10].

The goal of our work was to monitor the influence of dose rate and total dose absorbed at two various temperatures on some parameters characterizing the extent of degradation. In the previous studies we investigated isothermal decay of aged EVA copolymer in aerobic and anaerobic environment. The results strongly suggested that in both cases the effect is determined by dose absorbed and presence of oxygen during measurement [7]. Now we report further studies on the macroscopic effects of oxidative degradation monitored by several selected methods.

The oxidative induction time (OIT) measurements were unsuccessful as the thermograms did not reveal any distinct thermal transitions related to oxidation. Thus, oxidative induction temperatures (OITp) and pre-oxidation phase transitions were investigated in order to demonstrate the capability of the thermal analysis to monitor the actual status of the cable. The data obtained were compared with the results of mechanical and electrical tests as well as gel fraction values.

## 2. Experimental

### 2.1. Materials and aging procedure

The selected insulation was a component of the low voltage measurement cable. The following main constituents of the insulation composite were confirmed: 42% cross-linked poly(ethylene-*co*-vinyl acetate) (EVA), flame retardant and inorganic filler, $Al(OH)_3$ and $CaCO_3$ respectively. Initial thermal characteristic of the pristine insulation revealed that the degree of crystallinity of EVA was 9.5%. The value was calculated basing on the DSC measurements using the total enthalpy method, as shown by Equation (1):

$$DC = \frac{\Delta H_{\mathrm{m}}}{\Delta H_{100\%}} \tag{1}$$

where $DC$ is the degree of crystallinity, $\Delta H_{\mathrm{m}}$ is the enthalpy of melting of the sample (27.3 J/g) and $\Delta H_{100\%}$ is the enthalpy of melting for 100% crystalline polyethylene (288 J/g [6]). Additionally, on the basis of TGA measurements it was found that the VA content in the EVA copolymer was about 14% [11]

The material of the symbol I0 was exposed to accelerated aging in a gamma chamber equipped with a heating installation in the form of thermobox (ROZA facility in Ustav Jaderneho Vyzkumu A.S., Rez, Czech Republik). Thermal and radiation aging was carried out simultaneously.

The dose rate depended on the distance from the centrally located $^{60}Co$ source. Dosimetry of the particular positions in the chamber was based on the alanine signal detected by EPR spectroscopy [12]. Actual temperature of the cables during irradiation was controlled.

Every 200 h the samples introduced into the chamber were taken out and investigated by thermal, mechanical and electrical methods.

Accelerated aging processes were performed under the conditions specified in Table 1.

**Table 1.** Accelerated aging conditions of insulation marked by a symbol I0

| Code | Accelerated ageing procedure | | | |
|---|---|---|---|---|
| | Temperature [°C] | Radiation dose [Gy/h] | Time [h] | Cumulative dose [kGy] |
| I85-A | 85 | 420 | 200; 400; 600; 800; 1000 | 84; 168; 252; 336; 420 |
| I85-B | 85 | 940 | 200; 400; 600; 800; 1000 | 188; 376; 565; 752; 940 |
| I85-C | 85 | 1500 | 200; 400; 600; 800; 1000 | 300; 600; 900; 1200; 1500 |
| I55-B | 55 | 940 | 200; 400; 600; 800; 1000 | 188; 376; 565; 752; 940 |
| I55-C | 55 | 1500 | 200; 400; 600; 800; 1000 | 300; 600; 900; 1200; 1500 |

### 2.2. Thermal measurements

The thermo-oxidative stability testing was performed using a Differential Scanning Calorimetry apparatus (MDSC 2920 CE TA Instruments). Because the OIT tests failed, the OITp measurements were applied for determining the progress of insulation degradation [7, 13]. Both techniques, among others, monitor the amount of antioxidant remaining in the sample upon aging [14]. Small samples of the insulation (below 10 mg) placed in an open aluminium pan were inserted into the apparatus oven. The programmable temperature increase was 10°C/min starting from the ambient conditions. The measurements were conducted at an oxygen flow of 50 mL/min. Analysis of the results was conducted using TA Instruments software – Universal Analysis 2000. Each measurement was repeated at least 3 times.

### 2.3. Mechanical tests

The tensile properties were measured using a load frame testing machine Instron 5565 with extension rate of 50 mm/min and initial gauge length of 40 mm [15]. Samples were conditioned at 25°C and 50% relative humidity for 24 hours prior to testing. For each sample five specimens were tested.

### 2.4. Gel fraction

The gel content was determined for the cross-section segments of insulation. Extraction with xylene in a Soxhlet apparatus was performed according to the standard [16]. Percentage of the insoluble part of the sample containing fillers and 42% EVA was normalized to the polymer content only. Each measurement was repeated three times.

### 2.5. Microstructure characterization

Microstructure of the starting and accelerated aged samples was examined by Zeiss Ultra-High-Resolution Imaging SEM based on Zeiss' GEMINI field emission SEM column. The microscope had two electron detectors and an energy selective back scattering detector.

### 2.6. Electrical tests

Electrical properties of the aged cable were investigated through dielectric spectroscopy, using a Novocontrol Impedance Analyzer. Frequency ranged between $10^{-2}$–$10^{6}$ Hz with an input voltage of 3 $V_{rms}$. Test temperature was kept at 50°C.

## 3. Results and discussion

The first OITp measurement was performed for non-aged insulation I0. The recorded thermogram revealed two broad endothermic peaks attributed to two types of crystallites of various size and lattice defects, Figure 1. Shi *et al*. [17] reported that for EVA the peaks were located in two ranges – lower transition temperature was situated at 40–60°C and higher transition temperature in the range of 80–90°C. Generally, it is assumed that the larger crystals of better-defined structure show higher melting temperatures which in the case of studied EVA insulation corresponds to the transition showing maximal temperature ($T_m$) at about 89°C. The low temperature transition is situated at around 75°C what indicates that there are not small crystallites having melting points below 60°C.

For the insulation accelerated aged with dose rates of 940 or 1500 Gy/h at 55°C enthalpy of fusion determined for the transitions extended from 55 to 100°C increases from 22.3 to about 28.2 J/g for the most severely damaged samples. The representative example of the thermogram (I55-C; 1200 kGy) is shown in Figure 1. For aging performed at 55°C the variations in the maxima of phase transition temperature ($T_m$) are situated in the narrow range of 89.5–91.3°C. Intensity of the peak increases, contrary to the low-temperature thermal effect which almost disappears. It seems that the crystallites change structure and their population grows as might be concluded from almost 30% increase in the enthalpy of fusion. The last effect might be attributed to the radiation induced scission of tie macromolecules resulting in a growth of crystalline

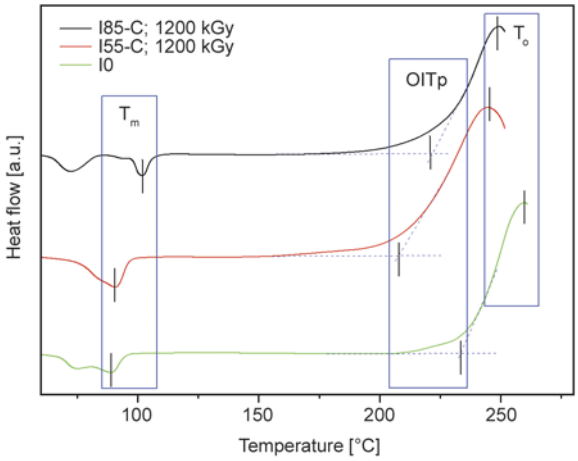


**Figure 1.** Examples of thermograms measured under oxygen flow for EVA insulation before and after accelerated aging

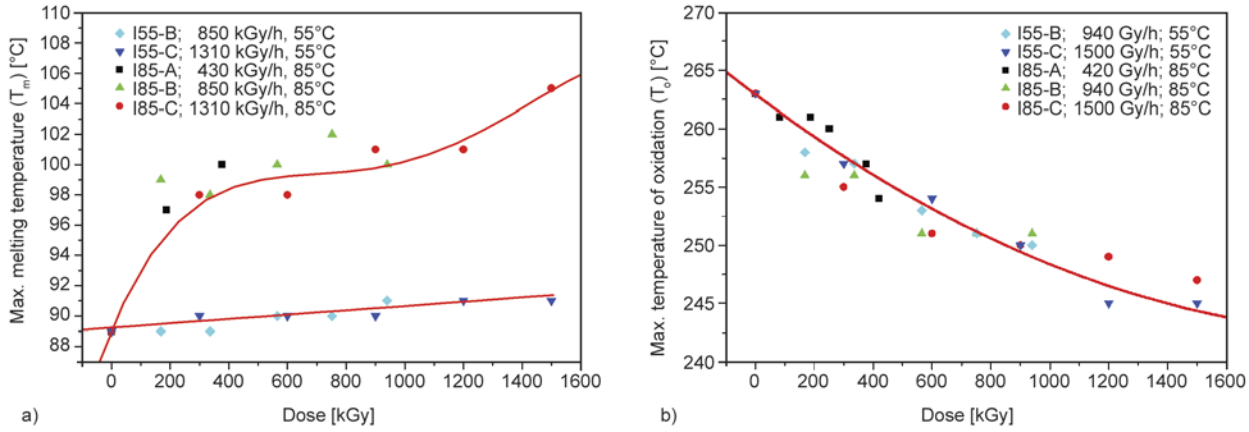


**Figure 2.** (a) Maximum melting temperatures ($T_m$) as a function of dose for EVA insulation aged under various conditions. (b) Maximum oxidation temperatures ($T_o$) as a function of dose for EVA insulation aged under various conditions. Average temperatures were determined on the basis of 3 independent measurements. The margin of error is ±1,5°C.

size and eventually in the increase of the content of ordered phase [18].

The thermograms are changing substantially when aging is performed at 85°C, i.e. at temperature corresponding to the melting state of a significant part of crystalline phase. The endothermic high-temperature transitions are shifted towards higher temperatures and Tm increases of at least 8 deg in comparison with Tm found for the initial sample, Figure 2a. Observed upon aging shift towards higher temperatures is usually attributed to the growth of structural regularity and to the enhanced crystal thickness. Due to continuous heat supply at 85°C melting is not only a surface process and the interior of the crystals is also involved in the structural changes. Reaching thermal equilibrium, all crystallites showing melting points smaller than the annealing temperature are melted. During cooling they form new crystallites of melting points higher or lower than the annealing temperature [11]. Additionally, under such conditions the original crystals having melting temperature higher than 85°C continuously improve their structure in the reorganization process [19]. These phenomena correspond to the temperature dependent isothermal recrystallization. In such circumstances, enthalpy of fusion should increase due to favorable conditions for the formation of well defined, larger crystals. Nevertheless, simultaneously gamma-radiation induces defects of the polymer macromolecules and for this reason the resultant degree of crystallinity does not increase in this case. We suggest that crystallites melted at 85°C, when exposed to ionizing radiation, are more susceptible to cross-linking due to intense conformational movements. The effect was confirmed earlier for some other polymers, e.g. polytetrafuoroethylene [20].

Contrary to above findings, the maximum oxidation temperature $T_o$ (see Figure 1) decreases almost monotonically with dose, and both dose rates and temperatures of accelerated aging do not influence significantly the parameter, Figure 2b.

Changes in OITp determined for the accelerated aged insulation are presented in Figure 3a and 3b. The significant reduction of the values with increasing dose was confirmed for aging conducted both at 55 and at 85°C; the OITp decrease even up to about 30 and 20°C was found, respectively. On the other hand, the influence of applied dose rates at lower temperature was negligible and at higher one barely noticeable. The results suggest that the nature of the processes for dose rates situated in the range of 420–1500 Gy/h is generally the same.

Thermal oxidative degradation of EVA measured by OITp involves at the first stage deacetylation followed by concurrent oxidation [21]. The elimination of acetic acid is possible via catalytic or non-catalytic reaction [22]. Hydroperoxides are important products of degradation that are converted into ketone groups in autooxidation process. When the EVA copolymer was oven aged at 180°C [23] other oxygen containing groups like hydroxyl, lactones, anhydride were confirmed by FTIR spectroscopy. It was also found that degradation leading to the creation of hydroperoxides prompts the formation of polyconjugated carbonyl groups resulting in color change [24]. All these processes and their contribu-

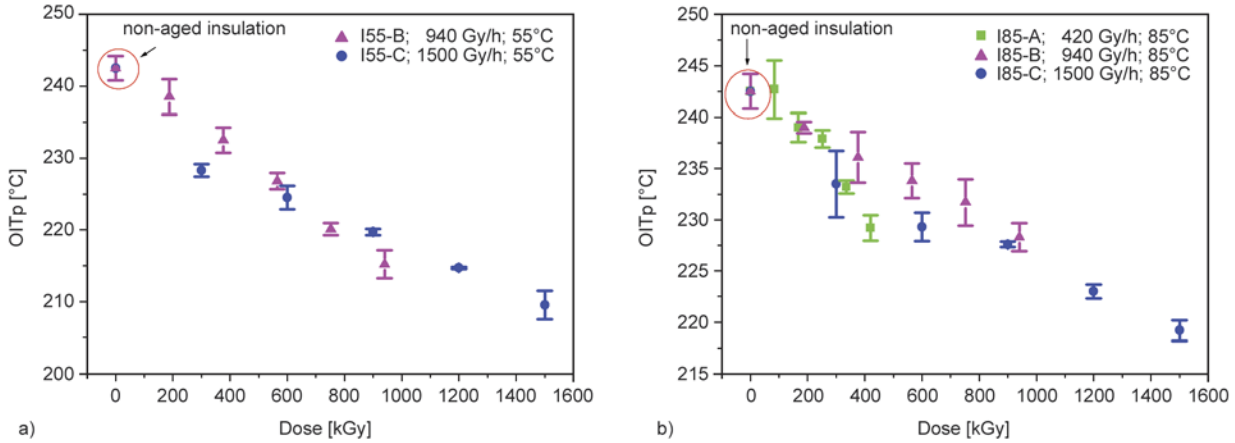


**Figure 3.** Relationship between dose absorbed by insulation and OITp values for various dose rates. (a) aging carried out at 55°C, (b) aging carried out at 85°C

tion in the exothermic oxidation observed above 200°C by OITp depend on the extent of degradation occurring during aging.

Interestingly, as shown in Figure 4, the gradual reduction of OITp is strongly temperature dependent. For both compared dose rates, 940 and 1500 Gy/h, the observed consequences of aging monitored by OITp are much severe for 55 than for 85°C. Based on these relationships we suggest that in the studied system the inverse thermal effect is observed and that thermal aging and radiation aging cause neither additive nor synergetic effects. Similar changes were observed in the past by Celina *et al*. [25] for semi-crystalline polyolefin.

At higher temperature (85°C) degradation measured by OITp is smaller than at lower one (55°C) what confirms our earlier assumption that radiation effects in the molten state are fundamentally different than in crystallites and that this dissimilarity results in abnormal behavior of the accelerated aged insulation. Postulated cross-linking not only increases thermooxidative stability but also hinders the diffusion of oxygen necessary for oxidative degradation. The inverse effect seems to be deeper for the lower dose rate, i.e. for 940 Gy/h, than for 1500 Gy/h, as in the first case the charts illustrating dependence OITp vs. dose diverge from each other to a greater extent.

For the samples exposed to accelerated aging the beginning of oxidation determined on the basis of OITp requires higher temperatures at the same absorbed dose than for the insulation radiation treated at 55°C what has to be the consequence of some structural obstacles. Thus, intermolecular bonds radiation generated in the molten crystals result in hindering exothermic oxidative processes identified above 200°C, as is apparent from Figures 1 and 4.

Radiation degradation of EVA copolymer refers primarily to the acetate regions. Murat Şen and Mehmet Copuroğlu concluded on the basis of FTIR analysis

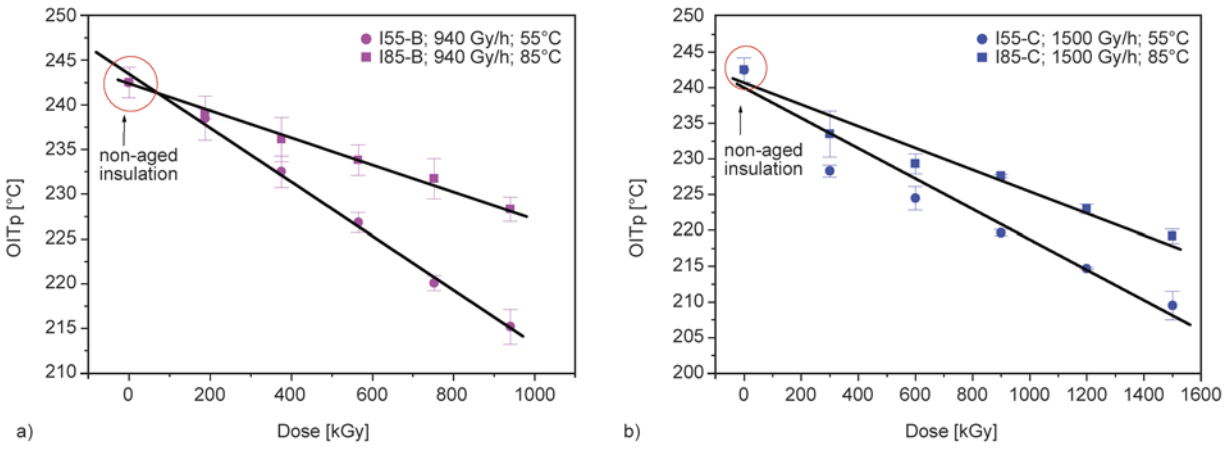


**Figure 4.** OITp as a function of dose absorbed for irradiations performed at 55 and 85°C with a dose rate of 940 Gy/h (a) and 1500 Gy/h (b)

that main products of gamma degradation were conjugate dienes and ketones [26]. Subsequently, according to Norrish I and Norrish II reactions the second species might in the multistage processes form carboxylic acid, lacton, ester or vinyl groups [27]. The total effect of oxidative degradation depends on the access to oxygen that is controlled, among others, by aging temperature. Generally for gases, solubility decreases with an increase in temperature, whereas diffusion changes in opposite direction [28]. Usually the second effect in semi-crystalline polymers is studied in terms of a spatial distribution of the impermeable crystalline phase and the permeable amorphous phase, which are cross-linked by tie chains or by intermolecular bonds. However, in our studies the melting of EVA crystals at 85°C partly removes this limitation. Due to topological differences of EVA at various temperatures and eventually not the same oxidation conditions, our assumption that it increasing contribution of cross-linking induces 'inverse effect' requires further evidences.

Mechanical properties also exhibit an interesting relationship with aging. In particular, Figure 5 shows elongation at break (EaB) vs. dose for the samples irradiated at 55°C (Figure 5a) and at 85°C (Figure 5b), with dose rates of 420, 940 or 1500 Gy/h. As can be seen, the influence of dose rate on the EaB decrease with dose absorbed is negligible in the range of doses herein investigated, confirming the OITp results presented in Figure 3. The effect of temperature is shown in Figure 6, which presents plots the EaB values as a function of dose absorbed for the samples irradiated at 55 and 85°C, with fixed dose rates of 940 Gy/h (Figure 6a) and 1500 Gy/h (Figure 6b). The slope of EaB decrease with dose is higher for insulation aged at 85 than at 55°C. It should be noted that the steep decrease of EaB, particularly at 85°C can be associated both with cross-

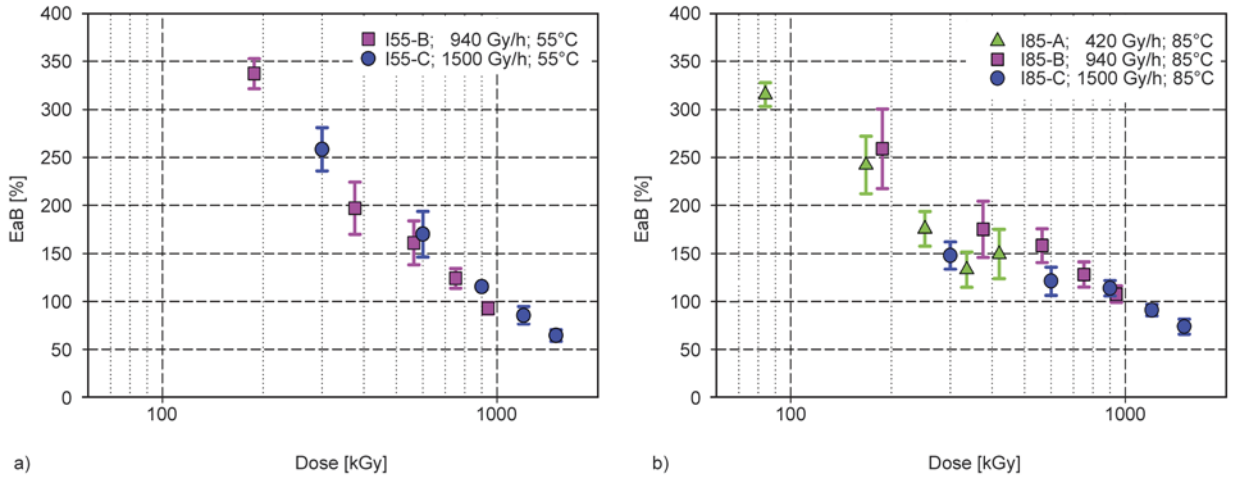


**Figure 5.** Elongation at break vs. dose for samples irradiated at 55°C (a) and 85°C (b), with dose rates of 420 Gy/h, 940 Gy/h and 1500 Gy/h

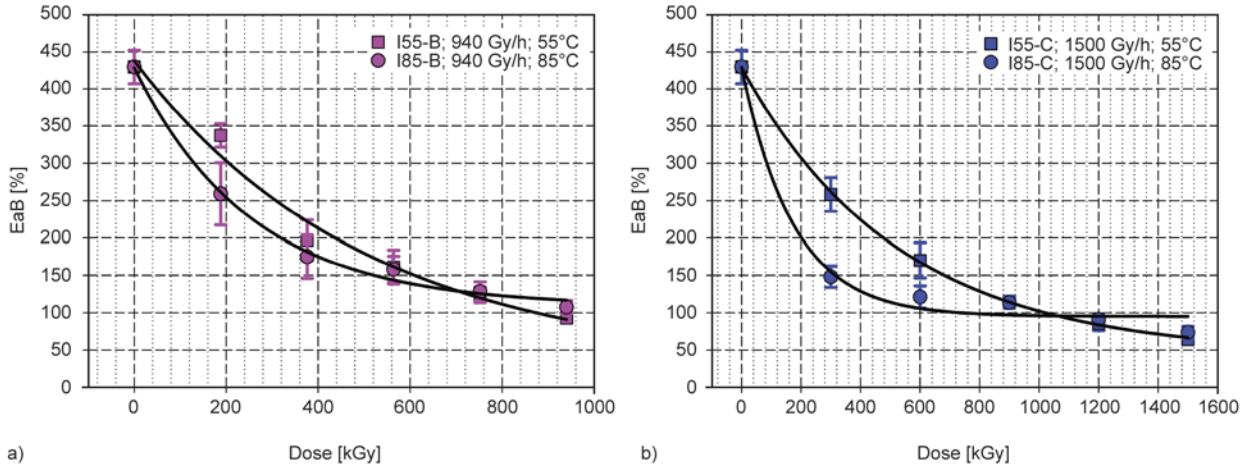


**Figure 6.** Elongation at break vs. dose for samples irradiated at 55 and 85°C, with dose rates of 940 Gy/h (a) and 1500 Gy/h (b)

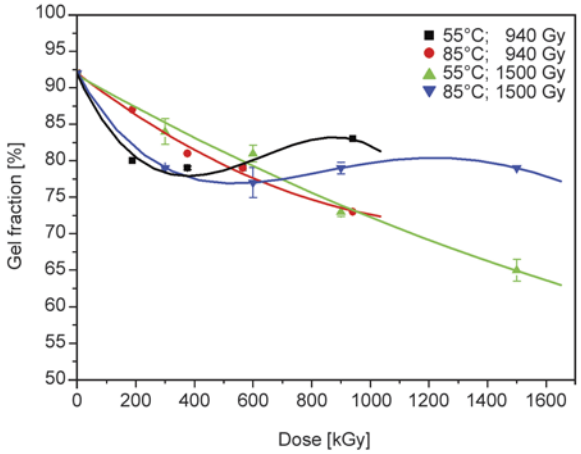


**Figure 7.** Gel fraction versus doses absorbed for polymeric matrix of insulation accelerated aged under various conditions

linking and with chain scission occurring during aging, thus the results are not conclusive with respect to the search for inverse effect evidences.

Gel fraction determined for the initially cross-linked polymeric matrix decreases almost proportionally to the growth of doses for both dose rates if aging temperature is fixed at 55°C, Figure 7. The relationship changes when irradiation is performed at 85°C. An initial decline of gel fraction of almost 15% is followed by the clear increase for the doses above 400 kGy and then the insoluble part of EVA remains higher than for specimens aged at 55°C. The tendency is unambiguous and corresponds to the correlations found for OITp vs. dose absorbed. Irradiation at both studied temperatures obviously induces degradation of the polymeric matrix and this effect prevails over cross-linking. However, the yield of the second process is higher at 85 than at 55°C what diversifies macroscopic properties of the aged insulation. The conclusion on enhanced cross-linking at elevated temperature additionally supports a decrease in the degree of crystallinity determined on the basis of melting transitions recorded during the first and second DSC cycle, e.g. for the sample I85°C irradiated with a dose of 1200 kGy crystallinity diminishes from 7.5 to 5.0%, respectively.

SEM studies were carried out for fractures of the non-aged insulation I0 and for the sample radiation aged at 85°C to a dose of 1200 kG at a dose rate of 1500 Gy/h, Figure 8. The images reveal inhomogeneous structure of the composites constructed from continuous polymeric matrix doped with inorganic particles of various sizes. It seems that for aged insulation the copolymer tightly adheres to the fillers and that the phase separation in this case is reduced in comparison with the starting sample. It could be a result of the reorganisation of the polymer during thermal and radiation aging, including cross-linking.

The measurement of electrical quantities, like e.g. imaginary permittivity, provides further confirmation of the results obtained from measuring OITp and gel fraction. Indeed, negligible variation of imaginary permittivity with the dose rate can be observe at fixed temperature (Figure 9) while at fixed dose rate (Figure 10) the imaginary permittivity increases more steeply at 55 than at 85°C, showing again the inverse temperature effect.

## 4. Conclusions

1. OITp measurements are convenient condition monitoring method for studding cable degrada-

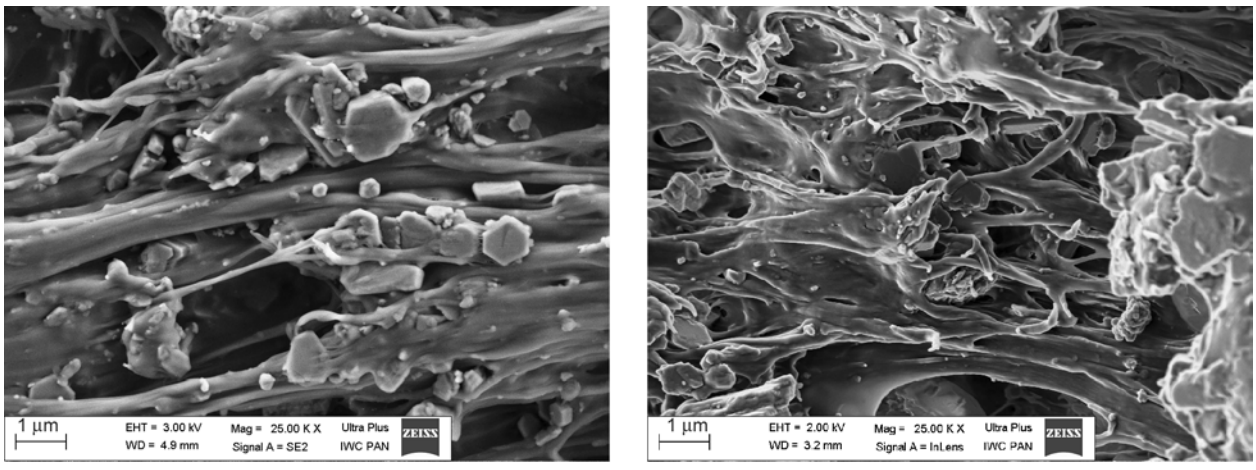


a) b)

**Figure 8.** The examples of SEM images recorded for the fractures of pristine sample I0 (a) and sample aged at 85°C with a dose of 1200 kGy at 1500 Gy/h (b)

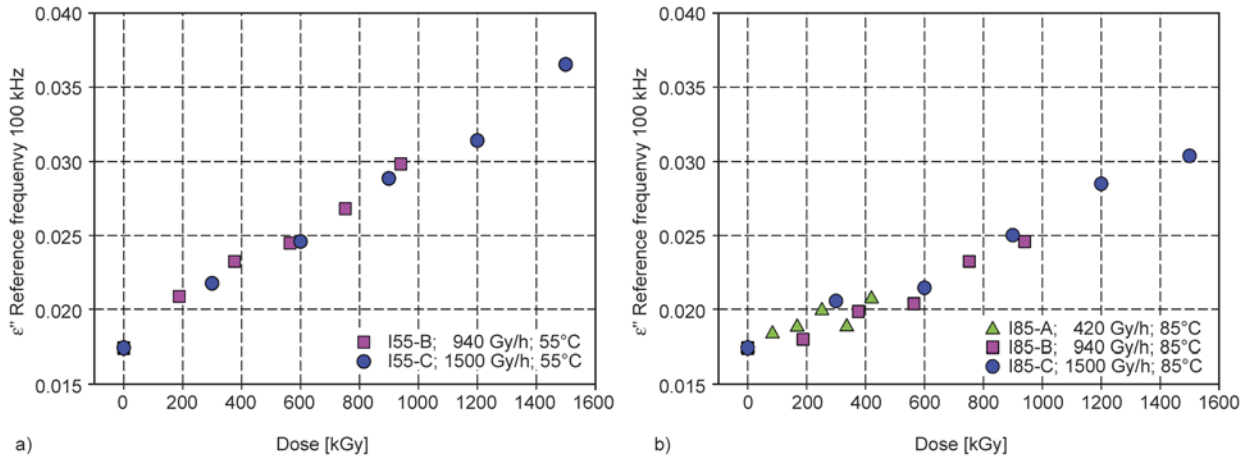


**Figure 9.** Imaginary part of permittivity (105 Hz) vs. dose for samples irradiated at 55°C (a) and 85°C (b), with dose rates of 420, 940 and 1500 Gy/h

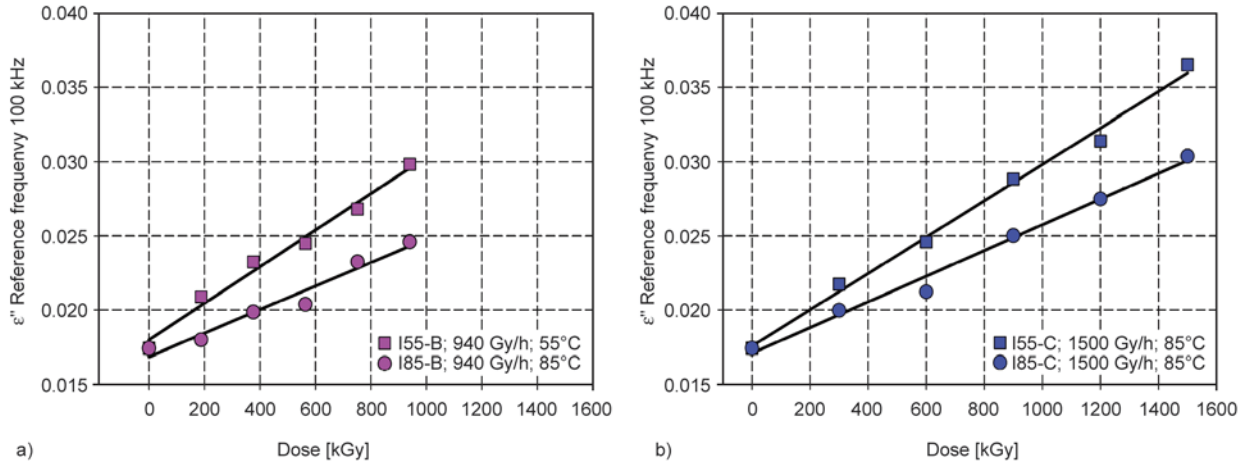


**Figure 10.** Imaginary part of permittivity (105 Hz) vs. dose for samples irradiated at 55 and 85°C, with dose rates of 940 Gy/h (a) and 1500 Gy/h (b)

tion, especially when OIT tests do not provide reliable results.

2. For EVA insulation the extent of thermal and radiation induced aging performed simultaneously is a function of temperature and dose, whereas the effect of applied dose rates is insignificant (420–1500 Gy/h).
3. Accelerated radiation aging conducted at the temperatures corresponding to melting points of the polymer crystallites (or higher) leads to the inconsistent conclusions which cannot be applied for the simulation of anticipated aging of the cables installed in NPPs and for the prediction of their lifetime. In this instance, the extrapolation of OITp values underestimates destruction effects expected at lower temperatures encountered in hot spots of reactors surrounding.
4. Electrical measurements, contrary to mechanical tests, provide results consistent with thermal analysis and gel fraction results confirming that the accelerated degradation of cable insulation strongly depends on the accelerated aging procedure applied to the specimens.
5. For the thermally and radiation aged EVA insulation an inverse thermal effect was confirmed by OITp, dielectric permittivity and gel fraction measurements. The phenomenon is associated with heating of the semicrystalline polymer in the range of melting endotherm during radiation treatment. It seems that such an aging procedure promotes radiation induced cross-linking limiting polymer degradation and hindering oxidation determined by the oxidative induction temperature measurements.
6. The temperature depended changes of EVA morphology influence mechanisms of radiation induced processes and eventually affect macro-

scopic features determined by some thermal, mechanical and electrical techniques.

## Acknowledgements

The work has been performed in the frame of 7th FP project: 'Aging Diagnostics and Prognostics of low-voltage I&C cables', grant agreement No 269893. Polish participation was co-financed by the Polish Ministry of Science and Higher Education, Grant Agreement No 2055. Matthias Meyer, Nexans is thanked for providing the cable used in this study.

## References

[1] Assessing and managing cable aging in nuclear power plants. IAEA, Nuclear Energy Series, No. NP-T-3.6, Wien (2012).

[2] Assessment and management of aging of major nuclear power plant components important to safety: In-containment instrumentation and control cables. Volume I. IAEA-TECDOC-1188, Wien (2000).

[3] Bartoníček B., Hnát V., Plaček V.: Life-assessment technique for nuclear power plant cables. Radiation Physics and Chemistry, **52**, 639–642 (1998). DOI: 10.1016/S0969-806x(98)00172-8

[4] Calmet J. F., Carlin F., Nguyen T. M., Bousquet S., Quinot P.: Irradiation ageing of CSPE/EPR control command electric cables. Correlation between mechanical properties and oxidation. Radiation Physics and Chemistry, **63**, 235–239 (2002). DOI: 10.1016/S0969-806x(01)00585-0

[5] Rosa D. S., Sarti J., Mei L. H. I., Filho M. M., Silveir S.: A study of parameters interfering in oxidative induction time (OIT) results obtained by differential scanning calorimetry in polyolefin. Polymer Testing, **19**, 523–531 (2000). DOI: 10.1016/S0142-9418(99)00022-7

[6] Agroui K., Collins G.: Determination of thermal properties of crosslinked EVA encapsulant material in outdoor exposure by TSC and DSC methods. Renewable Energy, **63**, 741–746 (2014). DOI: 10.1016/j.renene.2013.10.013

[7] Boguski J., Przybytniak G., Łyczko K.: New monitoring by thermogravimetry for radiation degradation of EVA. Radiation Physics and Chemistry, **100**, 49–53 (2014). DOI: 10.1016/j.radphyschem.2014.03.028

[8] Riga A., Collins R., Mlachak G.: Oxidative behavior of polymers by thermogravimetric analysis, differential thermal analysis and pressure differential scanning calorimetry. Thermochimica Acta, **324**, 135–149 (1998). DOI: 10.1016/S0040-6031(98)00530-9

[9] Woo L., Ling M. T. K., Ding S. Y., Westphal S. P.: Effect of ionizing radiation on the thermal oxidative stability of medical polymers. Thermochimica Acta, **324**, 179–185 (1998). DOI: 10.1016/S0040-6031(98)00534-6

[10] Woo L., Sandford C. L.: Comparison of electron beam irradiation with gamma processing for medical packaging materials. Radiation Physics and Chemistry, **63**, 845–850 (2002). DOI: 10.1016/S0969-806x(01)00664-8

[11] Menczel J. D., Prime R. B.: Thermal analysis of polymers. Fundaments and Applications. Wiley, Hoboken (2009).

[12] ISO/ASTM 51607-04: Standard practice for use of the alanine-epr dosimetry system (2012).

[13] ASTM D3895: Standard test method for oxidative-induction time of polyolefins by differential scanning calorimetry (2004).

[14] Plaček V., Bartoníček B.: The dose rate effect and the homogeneity of radio-oxidation of plastics. Nuclear Instruments and Methods in Physics Research Section B: Beam Interactions with Materials and Atoms, **185**, 355–359 (2001). DOI: 10.1016/S0168-583X(01)00943-0

[15] IEC/IEEE 62582-3: Nuclear power plants – Instrumentation and control important to safety – Electrical equipment condition monitoring methods – Part 3: Elongation at break (2012).

[16] ASTM D2765 Determination of gel content and swell ratio of crosslinked ethylene plastics (2006).

[17] Shi X-M., Zhang J., Li D-R., Chen S-J.: Effect of damp-heat aging on the structures and properties of ethylene-vinyl acetate copolymers with different vinyl acetate contents. Journal of Applied Polymer Science, **12**, 2358–2365 (2009). DOI: 10.1002/App.29659

[18] Kostoski D., Stojanović Z.: Radiation-induced crystallinity changes and melting behavior of drawn isotactic polypropylene. Polymer Degradation and Stability, **47**, 353–356 (1995). DOI: 10.1016/0141-3910(94)00126-X

[19] Stark W., Jaunich M.: Investigation of ethylene/vinyl acetate copolymer (EVA) by thermal analysis DSC and DMA. Polymer Testing, **30**, 236–242 (2011). DOI: 10.1016/j.polymertesting.2010.12.003

[20] Seguchi T.: New trend of radiation application to polymer modification – Irradiation in oxygen free atmosphere and at elevated temperature. Radiation Physics and Chemistry, **57**, 367–371 (2000). DOI: 10.1016/S0969-806x(99)00406-5

[21] Patel M., Pitts S., Beavis P., Robinson M., Morrell P., Khan N., Khan I., Pockett N., Letant S., von White II G., Labouriau A.: Thermal stability of poly(ethylene-*co*-vinyl acetate) based materials. Polymer Testing, **32**, 785–793 (2013). DOI: 10.1016/j.polymertesting.2013.03.014

[22] Rimez B., Rahier H., Van Assche G., Artoos T., Biesemans M., Van Mele B.: The thermal degradation of poly(vinyl acetate) and poly(ethylene-*co*-vinyl acetate), Part I: Experimental study of the degradation mechanism. Polymer Degradation and Stability, **93**, 800–810 (2008). DOI: 10.1016/j.polymdegradstab.2008.01.010

[23] Allen N. S., Edge M., Rodriguez M., Liauw C. M., Fontan R.: Aspects of the thermal oxidation of ethylene vinyl acetate copolymer. Polymer Degradation and Stability, **68**, 363–371 (2000).
DOI: 10.1016/S0141-3910(00)00020-3

[24] Allen N. S., Edge M., Rodriguez M., Liauw C. M., Fontan R.: Aspects of the thermal oxidation, yellowing and stabilisation of ethylene vinyl acetate copolymer. Polymer Degradation and Stability, **71**, 1–14 (2001).
DOI: 10.1016/S0141-3910(00)00111-7

[25] Celina M., Gillen K. T., Wise J., Clough R. L.: Anomalous aging phenomena in a crosslinked polyolefin cable insulation. Radiation Physics and Chemistry, **48**, 613–626 (1996).
DOI: 10.1016/0969-806x(96)00083-7

[26] Şen M., Copuroğlu M.: A comparative study of gamma irradiation of poly(ethylene-*co*-vinyl acetate) and poly (ethylene-*co*-vinyl acetate)/carbon black mixture. Materials Chemistry and Physics, **93**, 154–158 (2005).
DOI: 10.1016/j.matchemphys.2005.03.005

[27] Scaffaro R., Botta L., Gallo G.: Photo-oxidative degradation of poly(ethylene-*co*-vinyl acetate)/nisin antimicrobial films. Polymer Degradation and Stability, **97**, 653–660 (2012).
DOI: 10.1016/j.polymdegradstab.2012.01.003

[28] Rogers C. E.: Permeation of gases and vapours in polymers. in 'Polymer permeability' (Ed.: Comyn J.) Chapman and Hall, London, 11–73 (1985).
DOI: 10.1007/978-94-009-4858-7_2

*eXPRESS Polymer Letters Vol.9, No.4 (2015) 394–400*
*Available online at www.expresspolymlett.com*
*DOI: 10.3144/expresspolymlett.2015.37*

# The analysis of injection molding defects caused by gate vestiges

*T. Tábi*[1,2], *A. Suplicz*[1], *F. Szabó*[1], *N. K. Kovács*[1], *B. Zink*[1], *H. Hargitai*[3], *J. G. Kovács*[1*]

[1]Department of Polymer Engineering, Faculty of Mechanical Engineering, Budapest University of Technology and Economics, Műegyetem rkp. 3., H-1111 Budapest, Hungary
[2]MTA–BME Research Group for Composite Science and Technology, Műegyetem rkp. 3., H-1111 Budapest, Hungary
[3]Department of Materials Science and Technology, Széchenyi István University, Egyetem tér 1., H-9026 Győr,Hungary

*Received 26 August 2014; accepted in revised form 2 November 2014*

**Abstract.** Issues of product safety are the most serious problems of an injection molded product due to their risk to human health. Such a safety problem can be the needle-shaped vestige at the gate zone of injection molded products, called a gate vestige. Only observations of the formation of gate vestiges can be found in the literature, but the processing parameters influencing their dimensions, especially their height have not been studied yet. Our goal was to study the effect of various injection molding processing parameters and gate constructions on gate vestige formation.

***Keywords:*** *processing technologies, injection molding defect, damage mechanism, gate vestiges, 3-plate mold*

## 1. Introduction

In the 21st century modern plastics have more and more roles and are so widespread that they are a part of our everyday lives. Their consumption has become a benchmark of how developed a country is. In the injection molding cycle defects can occur, such as burn marks [1], delamination [2], flash [3], jetting [4], sink marks [5], weld lines [6] or warpage [7] and these can cause injection molded parts to be rejected.

Typically, the most serious are problems that could damage the mold and/or affect product safety. Such a product safety problem can be a so-called gate vestige, which is a remnant of the gate, thus a separation phenomenon between the runner and the product. The size and shape of the vestige depend mostly on the shape of the gate (mold design) and the processing parameters.

The elimination or moderation of gate vestiges by using various valve gates in the case of a hot runner system are widely investigated [8]. Valve gates like reciprocating pinpoint gates have a mechanically activated pin that shuts off the gate as the pin moves forward, which provides mechanical sealing and a relatively clean vestige [9, 10]. These valve gates provide the most control over gate vestiges but they significantly increase the complexity of the mold and introduce wear problems. Vestiges can also be controlled by using a standard fixed hot tip torpedo in hot runner systems. Gate vestiges and freezing are controlled by the temperature and the location of the tip in the gate area [10].

Xie *et al*. [11] investigated the effect of gates on the cavity filling pattern and residual stress of the injection molded part. They concluded that if a larger gate is used, the cavity will be filled faster and the residual stress of the part will be smaller. They concluded that melt temperature and injection rate can significantly affect the above two aspects, which might have an effect on gate vestiges as well. Shen *et al*.

*Corresponding author, e-mail: kovacs@pt.bme.hu

[12] showed simulation methods for gate location analysis, in which they calculated the ideal location and size of gates. Zhai *et al*. [13] performed gate location optimization for injection molding. They concluded that if injection pressure at the end of fill is minimized, gate location can be optimized. In spite of the best location, possible injection molding defects were not mentioned by the authors.

Sánchez and Lladó [14, 15] investigated direct gates, which are similar to pinpoint gates but significantly larger, thus the conclusions cannot be used for those because of the significantly different shear effects. For cold runner systems like three-plate molds, gate vestige and other injection molding defects can be avoided or minimized if a suitable gate or nozzle design is used. The tapered region should be as short as possible to achieve lower pressure for filling and reduce the height of the vestige. Generally, its length ranges from 0.13 to 0.25 mm. A tapered region and sharp corners at the entry into the cavity are important to ensure that the plastic will break between the gate and the product but as near the product as possible, leaving no or only a little vestige. It is important to optimize gate size as it has a major influence on gate vestige, shear induced heat, holding time and other important parameters. The gates of a three-plate mold are inherently self-degating, since the gate breaks off as the product is ejected from the cavity [9].

Although the problem of gate vestiges seems to be solved in expensive and complicated hot runner molds, in three-plate molds gate vestiges can still occur. The height of gate vestiges is determined not only by the mechanical strength of the solidified thermoplastic, but as gate vestiges are formed as a result of a complex process, injection molding parameters probably also have a significant effect on it. No information was found in the literature on the effect of injection molding parameters on the formation of gate vestiges.

In this paper our goal was to investigate the effect of various injection molding processing parameters and examine various gate constructions influencing the formation of gate vestiges. A quick measuring method was also developed to determine the dimensions of gate vestiges without any need for time-consuming optical and/or scanning electron microscope measurements.

## 2. Materials and equipments

BASF Terluran GP35 injection molding grade ABS terpolymer was chosen for the tests. This grade of ABS has a specific gravity of 1.04 g/cm$^3$, a melt volume rate of 34 cm$^3$/10 min (at 220°C and 10 kg of load) and a recommended melt and mold temperature of 220–270°C and 40–60°C respectively. The material was dried at 85°C for 4 hours prior to injection molding.

A three-plate mold with 16 cavities was chosen for the examinations. In the mold there were big differences between gate dimensions, therefore 15 cavities were blocked and the mold was used as a single-cavity mold. The effect of nozzle (gate) geometry on gate vestiges was also measured. Some geometrical parameters such as the diameter of the outlet, the nozzle end height and the internal angle near the outlet were varied in our experiments (Figure 1).

The other main geometrical parameters including the 2 mm inner diameter, the 15.6 mm length of the nozzle and the interior draft angle of 2° were the same. The varied geometrical parameters of the various nozzles can be seen in Table 1.

An Engel Victory 330/60 injection molding machine with a clamping force of 600 kN was used for producing parts for the investigation. The injection molding machine had a 35 mm diameter screw capable of a maximum injection rate of 151 cm$^3$/s and a maximum injection pressure of 1595 bars. The specimens were injection molded with the following parameters using pressure controlled filling (Table 2).

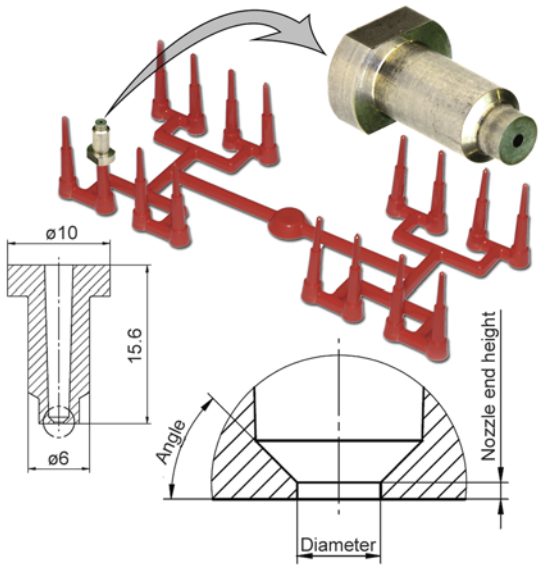


**Figure 1.** The varied geometrical parameters of the nozzles

**Table 1.** Geometrical parameters of various nozzle geometries

| Nr. | Diameter [mm] | Nozzle end height [mm] | Angle [°] |
|---|---|---|---|
| 1 | 0.8 | 0.08 | 45 |
| 2 | 0.8 | 0.2 | 45 |
| 3 | 0.8 | 0.8 | 45 |
| 4 | 1.0 | 0.08 | 45 |
| 5 | 1.0 | 0.2 | 45 |
| 6 | 1.0 | 0.8 | 45 |
| 7 | 1.2 | 0.08 | 45 |
| 8 | 1.2 | 0.2 | 45 |
| 9 | 1.2 | 0.8 | 45 |
| 10 | 1.0 | 0.2 | 30 |
| 11 | 1.0 | 0.2 | 60 |

**Table 2.** Injection molding set-up parameters

| Injection molding parameter | Value |
|---|---|
| Total injection time (the sum of the filling and holding time) [s] | 2.5 |
| Pressure [bar] | 600 |
| Injection rate limit [$cm^3/s$] | 110 |
| Residual cooling time [s] | 5 |
| Screw rotational speed [m/min] | 17.1 |
| Back pressure [bar] | 100 |
| Temperature of the zones [°C] | 238–200 |
| Temperature of the stationary/movable mold half [°C] | 35/16 |
| Cycle time [s] | 11.2 |

Injection molded specimens produced in the first 50 cycles were automatically rejected. Then, when steady-state production conditions were reached, injection molding was continued and every tenth specimen (cycle) was selected for measurement. A total number of twelve specimens were selected from continuous production to determine the average and the standard deviation of the measured values.

Mold temperature was set up based on preliminary studies and the inlet temperatures were chosen to maintain a uniform mold surface temperature. Some injection molding parameters (cooling time, mold opening speed, injection rate and total injection time) were varied to better understand gate vestige formation and to map their effect on the dimensions of the gate vestiges.

Microscopic measurements were performed to observe gate vestiges by using an Olympus BX 51M type optical microscope and a Jeol JSM 6380LA type electron microscope. The optical microscope was used only to determine the geometry of the gate vestiges, while the scanning electron microscope (SEM) was used for deeper analysis to determine the causes of gate vestige formation. To speed up the measurement of dimensions and at the same time keep the accuracy of the optical microscope, a Universal Serial Bus (USB) microscope type Celestron Handheld Digital Microscope was used in a combination with and self-developed software to automatically identify gate vestige dimensions. The new system was previously tested and validated by the conventional optical microscopic measurements.

## 3. Measurement method

As the first step, the optical microscope was used to determine the dimensions of gate vestiges, namely their height, bottom (base) diameter, and top diameter. By using 50× magnification, the gate sections of the specimens were easily observable and the dimensions of the gate vestiges were measured (Figure 2). The standard deviation of measurement was found to be low when the same 12 specimens were measured by various operators (human factor) and also the repeatability of the measurements was found to be excellent. The maximum differences between the values measured by the three measuring persons were 48, 31 and 17 μm, (height, bottom and top diameter). The USB microscope was also tested; photos were taken, loaded into graphics software and the dimensions of the gate vestiges were determined by converting the dimensions in pixels into μm using the resolution of the image. There is no significant difference between the measured values obtained from the optical and the USB microscope. It can be stated that the USB microscope not only allows faster evaluation but is also at least as accurate as the optical microscope, which makes the USB microscope suitable for the measurements.

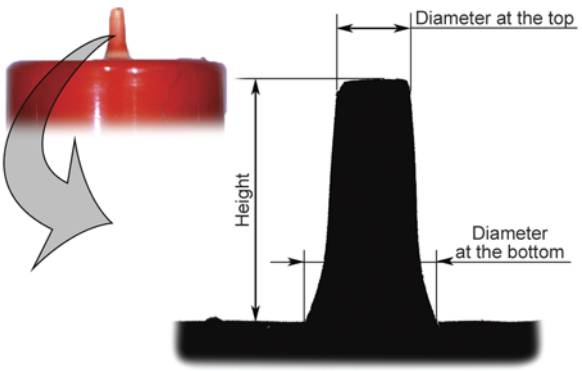


**Figure 2.** Analyzing the dimensions of gate vestige

## 4. Results and discussion

### 4.1. The effect of nozzle geometry on gate vestiges

Before analyzing the effect of various nozzle geometries, the reproducibility of the dimensions of gate vestiges was checked. Reproducibility was found to be very good. Injection molding was performed using different geometry nozzles. Figure 3 shows the most important dimension, the height of the gate vestiges according to the various nozzle geometries.

It can be seen that the height of gate vestiges can be significantly decreased by modifying the geometry of the nozzle. According to the height of the gate vestige, various types can be observed, such as low (nozzles number 1 and 2), medium (nozzles number 3, 6 and 7) and high (nozzles number 4, 5, 8, 10 and 11) and even no gate vestige in the case of nozzle number 9. Nozzles number 9, 1, 3, and 5 were chosen to represent no (zero), low, medium and high gate vestiges, respectively, for SEM observation and the images of the gate vestiges were also inserted into the drawings of the nozzles for visualization (Figure 4).

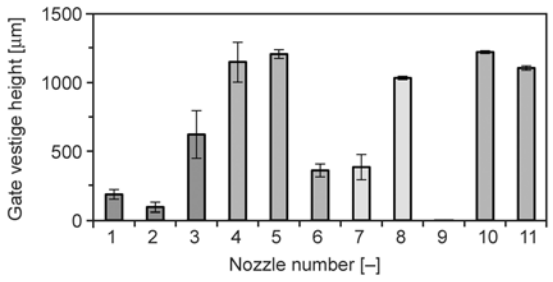


**Figure 3.** The height of the gate vestiges according to the various nozzles

It is obvious that nozzle number 9 was preferred as no gate vestige was produced and surprisingly, the highest gate vestige was not created with the nozzle with the largest nozzle end height dimension. It can also be seen that the diameter of the vestige is not equal to the diameter of the nozzle, thus the vestige does not form by the material simply detaching from the inner wall of the nozzle, but it is torn from its own material. This explains why a highly sheared region of material was found on the surface of the vestiges, which probably formed during degating due to the friction within the material or due to the high shear during the filling phase (Figure 5). This would mean that gate vestige takes place only as delamination at the interface of highly oriented layers. These

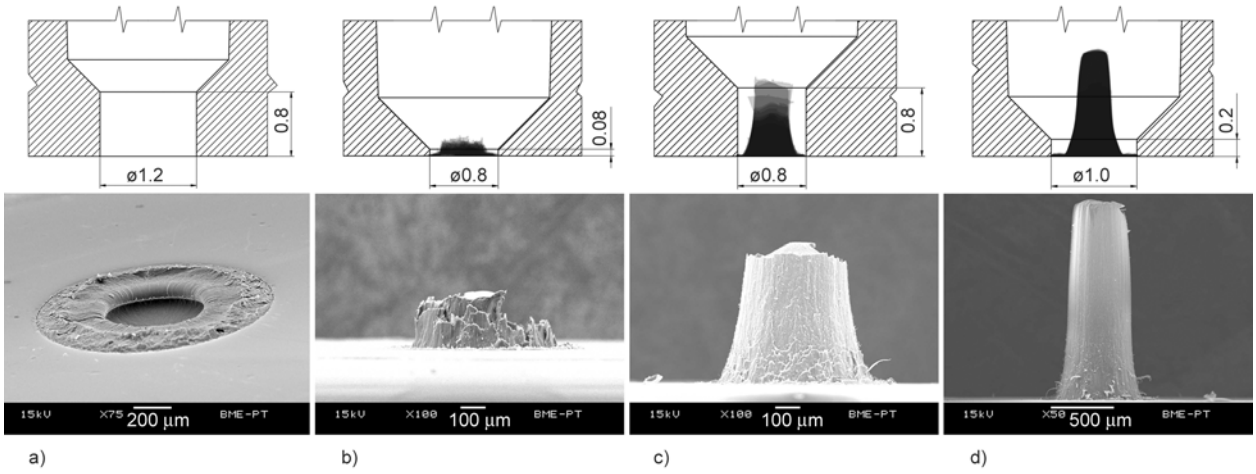


**Figure 4.** SEM micrographs and 10 superimposed microscopic pictures of the gate vestiges and the nozzle geometries for no (zero) gate vestige/nozzle number 9. (a), low (broken) gate vestige/nozzle number 1. (b), medium (broken) gate vestige/nozzle number 3. (c) and high (theoretically 'good') gate vestige/nozzle number 5. (d)

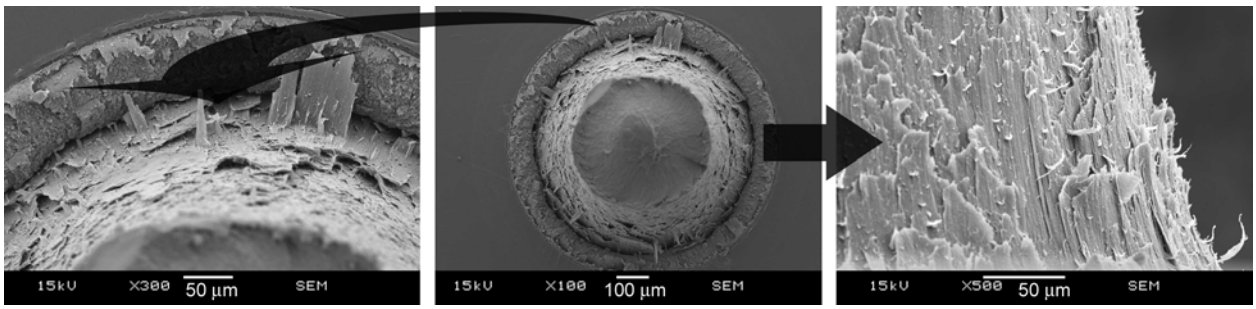


**Figure 5.** The highly sheared region of the gate vestige

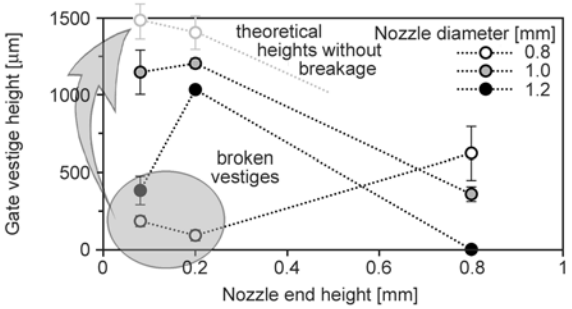


**Figure 6.** Gate vestige height produced with various nozzles as a function of nozzle end height

kind of delamination was observable on all gate vestige surfaces.

It is assumed that the height of gate vestiges is limited because if the gate vestige forming during filling the cavity was too high, it would break during degating due to the long grip length and this would result in a shorter and broken gate vestige. The height of the gate vestige can be seen as a function of nozzle end height and nozzle diameter in Figure 6.

The results seem to be stochastic at first sight, but if it is taken into account that some of them are broken, and some of them are undamaged, just pulled out from the inner core, a clearer tendency can be observed. No significant difference was found in the bottom diameter of gate vestiges as nozzle end height was increased, but there is a positive correlation between gate vestige bottom diameter and nozzle outlet diameter. As expected, when the outlet diameter of the nozzle was increased, the bottom diameter of gate vestiges increased (Figure 7). In the case of nozzle number 9 (1.2 mm nozzle diameter and 0.8 mm nozzle end height) no gate vestige exists thus only the outer diameter of the remaining 'ring' (Figure 4a) could be measured by SEM. Changing the internal angle near the outlet of the nozzles did not have a significant effect on the dimensions of gate vestiges.

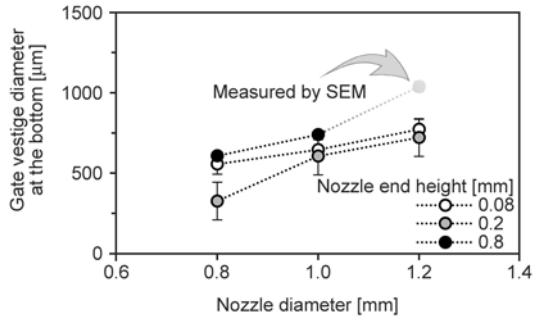


**Figure 7.** Gate vestige diameter at the bottom as a function of nozzle diameter, produced with various nozzles

## 4.2. The effect of injection molding parameters

In this chapter the effect of injection molding parameters, such as cooling time, mold opening speed, injection rate and total injection time on the dimension of gate vestiges were investigated. For further experiments, nozzle number 9 was used.

### 4.2.1. Analysis of cooling time

Gate vestiges may be caused by the breaking of the still hot and thus rubber-like runner system. In order to analyze this possibility, specimens were injection molded with an extremely long cooling time of 10 minutes. It was found that the height of the gate vestige did not change significantly; only a negligible decrease was found. It means that gate vestiges do not form because of the breaking of a still warm runner system, but form previously in the filling and holding phases.

### 4.2.2. Analysis of mold opening speed

Since the mechanical properties of polymers depend on the rate of deformation, the effect of mold opening speed was investigated to find whether it is possible to tear the specimens from the runner system leaving no gate vestige by using extremely high or low mold opening speeds. The original value of mold opening speed of 150 mm/s was used as a reference, while 10 and 450 mm/s of mold opening speeds were investigated as the smallest and highest possible speeds. The results showed that mold opening speed has only a minor effect on the height of gate vestiges. A possible explanation of the results is that it was not possible to vary deformation rate by mold opening speed at the desired level, where it could have had a significant effect on the gate vestige; only the top of the vestige was broken.

### 4.2.3. Analysis of injection rate

The effect of injection rate, or screw (ram) speed on gate vestiges was also analyzed. For this test 15, 20, 30, 40 and 50 $cm^3/s$ were set for injection rates. It was found that by decreasing the injection rate, the height of the gate vestige also decreased (Figure 8).

By increasing the injection rate, the bottom diameter of gate vestiges remains constant, while their height increases and their top diameter decreases, which means that they get more and more tapered. A possible explanation of the decreasing height of

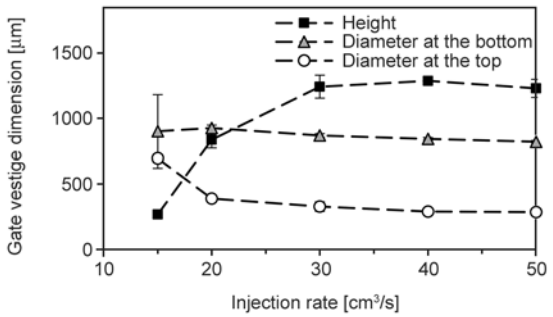


**Figure 8.** Dimensions of the gate vestige as a function of injection rate

gate vestiges is the lower melt rate during the filling of the cavity, which results in less shearing.

#### 4.2.4. Analysis of total injection time (filling + holding)

The effect of total injection time on the formation of gate vestiges was also investigated. The original value of total injection time (2.5 s) was varied between 2 and 5 s, while cooling time was also changed to keep the same cycle time. Since total injection time can be divided into filling time and holding time, if total injection time is changed, the parameter that is actually changed is holding time. As total injection time was increased, the height of the gate vestige gradually decreased (Figure 9).

There is a noticeable tendency that if the total injection time is increased, the height of the gate vestige decreases. However, a special phenomenon can also be observed: when the total injection time is around 2.5 s, no gate vestige, while at a total injection time of 2 or 3 s, a gate vestige with a certain height appeared. This most preferred 'no gate vestige' interval was only stable when total injection time was between 2.3 and 2.8 s. This special phenomenon is to be further investigated so that this kind of gate vestige can be reproduced on other products. The fact that the size of gate vestiges decreased as the total injection time was increased can be explained by the longer holding phase within the total injection time.

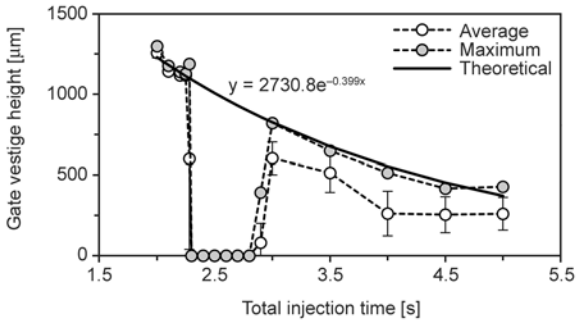


**Figure 9.** The height of gate vestiges as a function of total injection time. (For every single point 10 measurements were made where 'Maximum' is the highest measured value and 'Average' is the average of the ten samples.)

## 5. Conclusions

In our work, the product safety problem of injection molded parts called gate vestige was investigated with a three-plate multi-cavity mold. Since the unbalanced runner system strongly influences the results, 15 cavities were blocked. As the first step, we developed a quick measuring method suitable for accurately determining the dimensions of gate vestiges with the help of a USB microscope. 11 different nozzles were produced to examine the effect of nozzle geometry. The reproducibility of the technology with the single-cavity mold was checked and found to be excellent. It was demonstrated that by increasing nozzle end height and/or the outlet diameter of the nozzle, the height of the gate vestige could be decreased.

The effect of some of the process parameters like total injection time, cooling time, injection rate and mold opening speed were also tested. It was proved that by increasing total injection time or decreasing the injection rate, it is possible to decrease the height of gate vestiges, while cooling time and mold opening speed had only a minor effect on their height.

The main causes of gate vestiges were found to be shear and orientation conditions during molding. It is assumed that the formation of the gate vestige structure itself is already completed during filling and can be found within the nozzle in the solidified polymer, however, degating can still modify this structure by breaking it at a certain cross-section.

Finally, the low standard deviation of the height of gate vestiges proved that the whole process of gate vestige formation is not stochastic or random. This proves that if all the parameters and conditions of the injection molding process are known, the height of gate vestiges can be calculated, although probably in a very complex way.

## Acknowledgements

This paper was supported by the János Bolyai Research Scholarship of the Hungarian Academy of Sciences. This work was supported by the Hungarian Scientific Research Fund (OTKA K105257 and OTKA PD 105995).

This work is connected to the scientific program of the 'Development of quality oriented and harmonized R+D+I strategy and functional model at BME' project. This project is supported by the New Széchenyi Plan (Project ID: TÁMOP-4.2.1/B-09/1/KMR-2010-0002).

The work reported in this paper has been developed in the framework of the project 'Talent care and cultivation in the scientific workshops of BME' project. This project is supported by the grant TÁMOP - 4.2.2.B-10/1-2010-0009.

The research work presented in this paper was carried out as part of the TÁMOP-4.2.2.A-11/1/KONV-2012-0029 project in the framework of the New Széchenyi Plan. The realization of this project is supported by the European Union, and co-financed by the European Social Fund.

## References

[1] Garcia J. L., Koelling K. W., Xu G., Summers J. W.: PVC degradation during injection molding: Experimental evaluation. Journal of Vinyl and Additive Technology, **10**, 17–40 (2004).
DOI: 10.1002/vnl.20004

[2] Karger-Kocsis J., Csikai I.: Skin-core morphology and failure of injection-molded specimens of impact-modified polypropylene blends. Polymer Engineering and Science, **27**, 241–253 (1987).
DOI: 10.1002/pen.760270403

[3] Zhu J., Chen J. C.: Fuzzy neural network-based in-process mixed material-caused flash prediction (FNN-IPMFP) in injection molding operations. The International Journal of Advanced Manufacturing Technology, **29**, 308–316 (2006).
DOI: 10.1007/s00170-005-2528-x

[4] Oda K., White J. L., Clark E. S.: Jetting phenomena in injection mold filling. Polymer Engineering and Science, **16**, 585–592 (1976).
DOI: 10.1002/pen.760160811

[5] Mathivanan D., Parthasarathy N. S.: Prediction of sink depths using nonlinear modeling of injection molding variables. The International Journal of Advanced Manufacturing Technology, **43**, 654–663 (2009).
DOI: 10.1007/s00170-008-1749-1

[6] Kovács J. G., Sikló B.: Experimental validation of simulated weld line formation in injection moulded parts. Polymer Testing, **29**, 910–914 (2010).
DOI: 10.1016/j.polymertesting.2010.06.003

[7] Kovács J. G., Sikló B.: Investigation of cooling effect at corners in injection molding. International Communications in Heat and Mass Transfer, **38**, 1330–1334 (2011).
DOI: 10.1016/j.icheatmasstransfer.2011.08.007

[8] Beaumont J. P.: Runner and gating design handbook. Hanser, Munich (2004).

[9] Rees H.: Mold engineering. Hanser, Munich (2002).

[10] Campo E. A.: The complete part design handbook. Hanser, Munich (2006).

[11] Xie P., Guo F., Jiao Z., Ding Y., Yang W.: Effect of gate size on the melt filling behavior and residual stress of injection molded parts. Materials and Design, **53**, 366–372 (2014).
DOI: 10.1016/j.matdes.2013.06.071

[12] Shen Y-K., Wu C-W., Yu Y-F., Chung H-W.: Analysis for optimal gate design of thin-walled injection molding. International Communications in Heat and Mass Transfer, **35**, 728–734 (2008).
DOI: 10.1016/j.icheatmasstransfer.2008.01.014

[13] Zhai M., Lam Y. C., Au C. K., Liu D. S.: Automated selection of gate location for plastic injection molding processing. Polymer-Plastics Technology and Engineering, **44**, 229–242 (2005).
DOI: 10.1081/PTE-200048523

[14] Sánchez B., Lladó J.: Surface quality of PVC fittings based on the design of the sprue. Journal of Materials Processing Technology, **207**, 13–20 (2008).
DOI: 10.1016/j.jmatprotec.2008.04.041

[15] Lladó J., Sánchez B.: Influence of injection parameters on the formation of blush in injection moulding of PVC. Journal of Materials Processing Technology, **204**, 1–7 (2008).
DOI: 10.1016/j.jmatprotec.2007.12.063